Study of Compression Modes in 56 Ni using an Active Target

Bagchi Soumya

Study of Compression Modes in ^{56}Ni using an Active Target

To my parents and family
&
especially my mother

COVER: Giant's Causeway on the northern coast of Northern Ireland.
COVER DESIGNED BY: Dipayan Paul & Soumya Bagchi

university of groningen

kvi - center for advanced radiation technology

This work is supported by University of Groningen (RUG) and the Helmholtzzentrum für Schwerionenforschung GmbH (GSI), Darmstadt, Germany.

ISBN: 978-90-367-7709-4 (printed version)
ISBN: 978-90-367-7708-7 (digital version)

PRINTED BY: Grafimedia, Groningen, March 2015

university of groningen

Study of Compression Modes in ^{56}Ni using an Active Target

PhD thesis

to obtain the degree of PhD at the
University of Groningen
on the authority of the
Rector Magnificus Prof. E. Sterken
and in accordance with
the decision by the College of Deans.

This thesis will be defended in public on

Friday 1 May 2015 at 14:30 hours

by

Soumya Bagchi

born on 4 February, 1987
in Siliguri, India

Supervisors
Prof. N. Kalantar-Nayestanaki
Prof. M.N. Harakeh

Co-supervisor
Dr. J. Gibelin

Assessment committee
Prof. T. Aumann
Prof. A. Bracco
Prof. O. Scholten

Contents

Chapter 1

Introduction

In 2015, the nuclear-physics community will celebrate the 30^{th} anniversary of the first genuine work on radioactive ion beams [1] used to study the properties of atomic nuclei. However, until the 50's, the nuclear-physics experiments were constrained to the stable nuclei or the long-lived unstable nuclei (black boxes in Fig. 1.1). With the advent of new types of powerful accelerators, it is possible nowadays to access nuclei with exotic neutron-proton ratios. Furthermore, it is predicted that there are more than 3000 nuclei that could exist in bound states but have not been experimentally observed yet. How the structure and properties of a nucleus change with exotic ratios is still one of the fundamental questions in nuclear physics.

The study of the collective modes in nuclei, the so-called giant resonances, has been one of the important research topics in the field of nuclear physics for several decades. Giant resonances in nuclei, especially for exotic nuclei, are important in understanding some astrophysical phenomena, such as, supernovae explosions, formation of neutron stars etc. . Giant resonances are well established for stable nuclei, however, they show different behaviors while approaching nuclei with exotic N/Z ratios. In neutron-rich nuclei, the collectivity of extra neutrons relative to protons can cause soft multipole excitations or pygmy resonances [3, 49]. Therefore, it is necessary to extend our knowledge of giant resonances towards exotic nuclei.

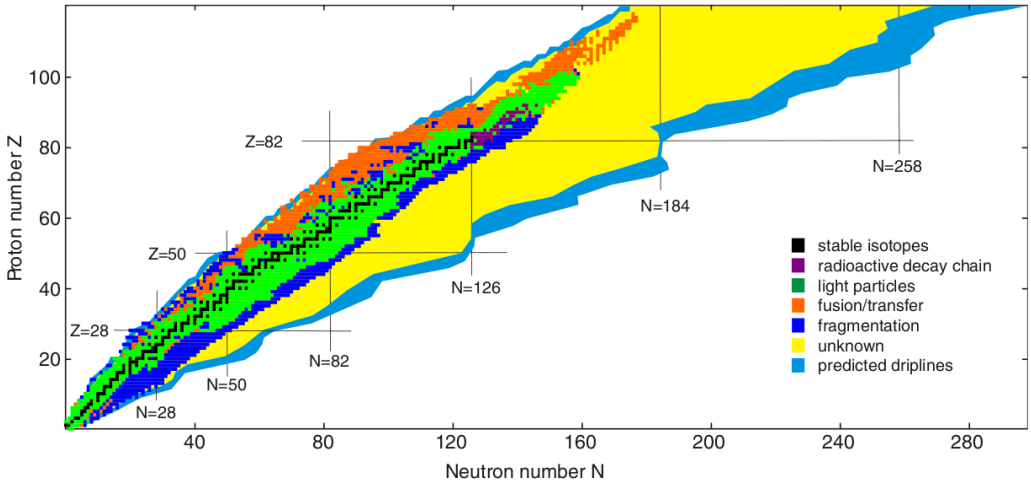

Figure 1.1: Chart of atomic nuclei. The nuclei are classified according to their number of neutrons (abscissa) and number of protons (ordinate). The valley of stability is shown in black boxes. Other unstable nuclei are shown in different colors depending on their production mechanisms: light-ion induced reactions (green), fragmentation processes (dark blue), fusion or transfer reactions (orange) and radioactive decay chains (magenta). The nuclei in the yellow region are predicted but not yet observed. The limits of the existence of nuclei is shown by the light-blue area (the so-called proton-drip line and neutron-drip line) [2].

1.1 Historical overview of giant resonances

The atomic nucleus is a many-body quantum system. In such systems, occurrence of collective oscillations is a natural phenomenon. Giant resonances, which is the subject of this thesis, are prime examples of collective oscillations of nucleons in a nucleus. Giant resonances are characterized by excitation energies higher than the particle-emission threshold and broad widths greater than 2 MeV.

Giant resonances can easily be described by the macroscopic models based on semi-classical concepts. Within the liquid-drop model, giant resonances can be understood as small-amplitude collective oscillations of a nucleus around its equilibrium shape and density. But unlike the only one type of fluid in the liquid-drop model, the nuclear fluid consists of four different types of fluids; protons and neutrons with spin-up and spin-down.

Giant resonances can be categorized depending on three quantum numbers characterizing the transition between the initial and the final state:

- Multipolarity: ΔL

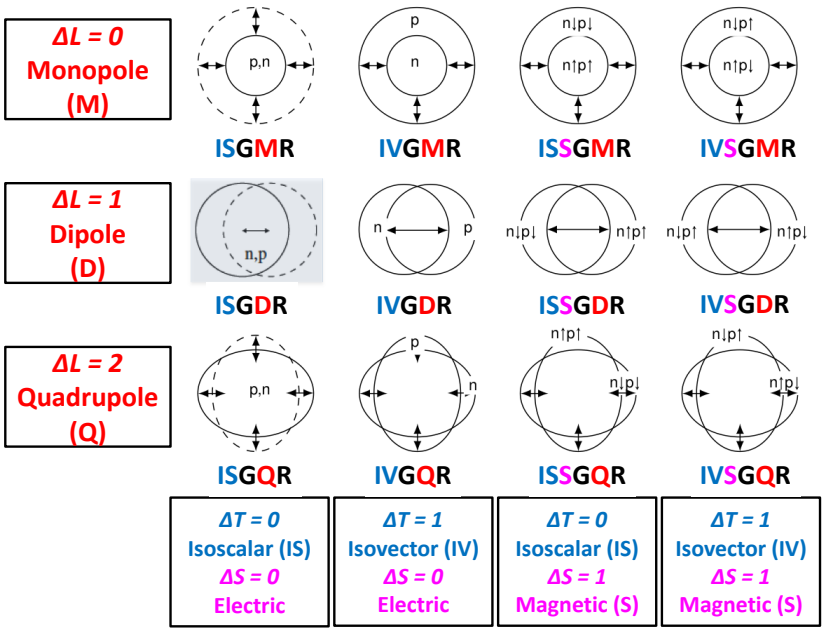

Figure 1.2: Schematic representation of giant resonances for the monopole, dipole and quadrupole modes. Isoscalar and isovector modes correspond to neutrons and protons moving in phase and out of phase, respectively. Similarly, electric (scalar) and magnetic (vector) modes correspond to nucleons with spin-up and spin-down moving in phase and out of phase, respectively. The notations used are self-explanatory [4]. The ISGDR depicted in this figure is a spurious center-of-mass motion. For details, see Chapter 2.

- Spin: ΔS
- Isopin: ΔT

An *isoscalar* mode corresponds to protons and neutrons oscillating in phase ($\Delta T = 0$) whereas an *isovector* mode corresponds to protons and neutrons oscillating out of phase ($\Delta T = 1$). Similarly, an *electric* mode corresponds to nucleons with spin-up and spin-down oscillating in phase ($\Delta S = 0$) and a *magnetic* mode corresponds to nucleons with spin-up and spin-down oscillating out of phase ($\Delta S = 1$). In Fig. 1.2, a schematic diagram of different giant resonance modes is shown for the lowest three multipolarities: $\Delta L = 0$ (*monopole*), $\Delta L = 1$ (*dipole*) and $\Delta L = 2$ (*quadrupole*) where ΔL represents the change in the orbital angular momentum. For each multipolarity, *isoscalar-electric* ($\Delta T = 0$, $\Delta S = 0$), *isovector-electric* ($\Delta T = 1$, $\Delta S = 0$), *isoscalar-magnetic* ($\Delta T = 0$, $\Delta S = 1$) and *isovector-magnetic* ($\Delta T = 1$, $\Delta S = 1$) modes are shown.

The first evidence for a giant resonance was found in 1937 by Bothe and Genter by means

of photo-absorption by ^{63}Cu nucleus [5]. This type of giant resonance, obtained by photo-absorption, is called Isovector Giant Dipole Resonance (IVGDR). In 1944, the first theoretical description of dipole oscillation of the nucleus was given by Migdal [6]. A systematic study of the properties of giant resonances began in 1947 [7, 8] when the first betatron came into operation.

In 1971, another type of giant resonance was observed by Pitthan and Walcher [9] which was thought to be a collective E2 excitation. It is the Isoscalar Giant Quadrupole Resonance (ISGQR), the energy of which is below the excitation energy of IVGDR.

The first evidence for the existence of Isoscalar Giant Monopole Resonance (ISGMR) was found by Harakeh et al. in 1977 [10,11] by means of inelastic α-particle scattering at 120 MeV on ^{206,208}Pb, ^{197}Au and ^{209}Bi. From its discovery in 1977 up till now, ISGMR has been extensively studied both for stable and unstable nuclei not only by inelastic α-particle scattering but also by deuteron scattering [53].

First attempts of identifying Isoscalar Giant Dipole Resonance (ISGDR) were made in the early 80's. Indications of this resonance were reported in inelastic scattering measurements with protons and α-particles [12–16]. Although several similar measurements claimed the non-existence of this resonance [17], the first 0° measurements for the study of ISGDR were reported by Davis et al. [18, 19] in 1997.

Establishing the occurrence of isovector giant resonances other than IVGDR turned out to be quite difficult as both Isovector Giant Quadrupole Resonance (IVGQR) and Isovector Giant Monopole Resonance (IVGMR) are located in the high excitation energy regions implying broad and overlapping distributions. However, the first evidence for IVGQR was found by Pitthan [20] and Torizuka et al. [21] via electron-scattering experiments. The study of IVGQR strength distribution using the (γ, n) reaction was demonstrated by Sims et al. [22].

The first definitive evidence for IVGMR was reported by Bowman et al. [23] in 1983, where the resonance was studied by the charge-exchange reactions ($\pi^{\pm}$, π^0) at a bombarding energy of 165 MeV.

The best probe to study the isoscalar giant resonances is α-particle scattering because of two-fold advantages. Since the α-particle has zero spin and isospin, the electric isoscalar resonances are predominantly excited. Moreover, since inelastic α-particle scattering is a surface reaction, the angular distributions are characteristic of the transferred angular momentum ΔL.

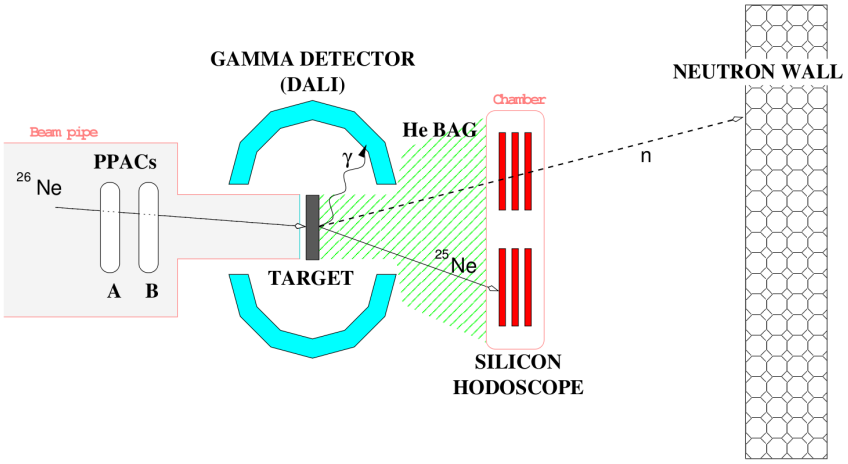

Figure 1.3: The schematic view of the experimental setup used at RIKEN to study the low-lying dipole strength in the neutron-rich ^{26}Ne. Picture is taken from Ref. [25].

1.2 Experimental setups for the study of giant resonances

The experimental setups for studying giant resonances vary depending on the nature of the nucleus of interest.

- In case of a stable nucleus, the nucleus is used as a target and the probes (p, d or α-particle...) are used as projectiles. We call this direct or normal kinematics.
- In case of unstable nuclei, their short half lives forbid these nuclei to be used as targets. Hence, the nucleus becomes the projectile and the probe the target, implying inverse kinematics.

Extensive studies for giant resonances in stable nuclei have been made. Performing experiments with unstable nuclei is a challenge. One of the main challenges is the low production intensity. Therefore, several experimental techniques must be adapted to study the properties of unstable nuclei.

Coulomb excitation

The isovector dipole strength of a nucleus can be studied by Coulomb excitation. For this purpose, the beam of interest impinges on a high-Z target (usually Pb). The fragments

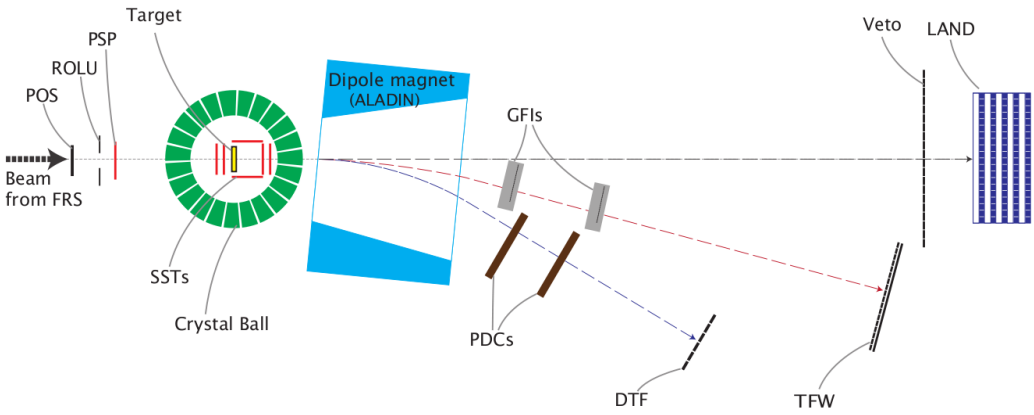

Figure 1.4: The schematic view of the experimental setup used at GSI to measure dipole response for neutron-rich Oxygen isotopes [26]. Picture is taken from Ref. [27].

are detected in the particle detectors. The emitted neutrons from the excited projectile or the excited projectile-like fragments are kinematically focused in the forward direction and are detected in neutron detectors [24, 25]. For emitted γ-rays detection, the γ-ray detectors (e.g. NaI detectors) surround the target. In Figs. 1.3 and 1.4, schematic diagrams of such experimental setups are shown.

Storage ring

Giant resonances in exotic nuclei can also be studied with the help of storage rings. Since the production rates of the exotic beams are low, a gain in the yield can be obtained by the gain in luminosity of the beam which is achieved through the accumulation and recirculation of the beam in the ring [28]. In Fig. 1.5, the schematic diagram of such a storage ring is shown. For inverse kinematics, the probe or the light particle can be put in the target position as shown in the figure. Usually, a hydrogen or helium gas-jet target is used in this case to study the giant resonances via (p, p') or (α, α') types of reactions. Typical luminosity that can be achieved with the storage ring is of the order of 10^{26}–10^{27} cm^{-2} s^{-1} for some radioactive isotopes.

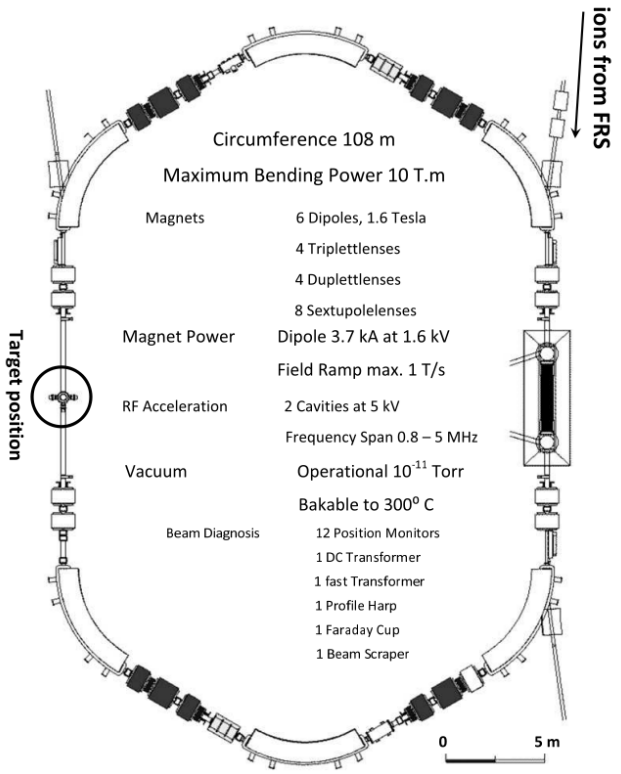

Figure 1.5: Schematic view of the experimental storage ring (ESR) facility at GSI. Picture is taken from Ref. [29].

Active target

An alternative to the above-mentioned experimental setups, which is useful to study giant resonances in unstable nuclei is to use an active-target detector. The active-target technique can be used efficiently for inverse-kinematics reactions. As mentioned above, the production rates of the exotic beams are low, requiring a thick target to get a reasonable yield. But usage of a thick target degrades the energy resolution and also the very low-energy recoil particles may stop inside the target. In the active-target technique, the thickness of the target can be increased without loss of energy resolution. Furthermore, very low-energy (sub MeV) recoil particles can be detected with this type of detector. Such a kind of detector is the MAYA detector. The aim of this work is to study the isoscalar giant resonances in neutron-deficient ^{56}Ni via ^{56}Ni$(\alpha,\alpha')^{56}$Ni* reaction using the active-target detector MAYA.

The details of the experimental setup, analysis procedures and results, are presented in this thesis. Relevant information can also be found from Ref. [30] which was dedicated to study ISGMR and ISGQR in ^{56}Ni with deuteron scattering and from Ref. [69] which was dedicated to study soft-monopole resonance, ISGQR and ISGMR in ^{68}Ni via deuteron and α-particle scattering. In both cases, the experiments were performed using the active-target detector MAYA.

1.3 Outline

In this thesis, we will focus on the isoscalar giant resonances in the neutron-deficient doubly-magic nucleus ^{56}Ni. The dedicated experiment of inelastic α-scattering on ^{56}Ni was performed at GANIL in May 2011. The outline of this thesis is as follows:

In **Chapter 2** the theoretical tools that are commonly used to describe the giant resonance states are described. Some theoretical predictions and experimental evidences of giant resonances in Ni isotopes are also given. Finally, the theoretical predictions for the angular distributions for ISGMR, ISGDR and ISGQR in ^{56}Ni relevant to this thesis are presented.

Chapter 3 is dedicated to the details of the MAYA active-target detector and the corresponding electronics.

Chapter 4 describes the tools and methods that were used for the analysis of the data presented in this thesis. It includes the methods for track and scattering-angle reconstruction, beam purification and filters that were applied to avoid spurious events.

Chapter 5 reports on the details of the simulations performed. It contains the method developed to generate events, determination of experimental resolutions and discussion about efficiency corrections.

Chapter 6 is devoted to the results obtained from the data analysis. The procedure of getting the angular distributions for different multipolarities of excited giant resonances will be detailed.

Chapter 7 contains the overall summary of the whole thesis and it gives an outlook for future experiments.

Finally, the summary in Dutch is given in **Chapter 8**.

Chapter 2

Giant resonances and nuclear incompressibility

Giant resonances (GR) can be understood via macroscopic models but for detailed understanding, microscopic calculations have to be performed. This chapter begins with the macroscopic and microscopic descriptions of GRs. The relationship between GRs and nuclear incompressibility will be detailed. Theoretical predictions and experimental evidences of GRs in Ni isotopes closer to the subject of this manuscript will be discussed. This chapter ends with the theoretical predictions for the angular distributions of the GRs for the ^{56}Ni$(\alpha,\alpha')^{56}$Ni* reaction.

2.1 Macroscopic model

The simplest way of depicting giant resonances is through the macroscopic model where the nucleus is assumed to be a liquid drop which vibrates in different modes around its equilibrium shape. For a schematic representation of different modes of giant resonances, see Fig. 1.2. Among these giant resonances modes, Isoscalar Giant Monopole Resonance (ISGMR) is called the "*breathing mode*" as it shows a volume oscillation around the equilibrium volume, i.e., the nucleus is either compressed or expanded with all the nuclear fluids (proton and neutron fluids) oscillating in phase. Experiments with the stable nuclei with mass number $A \geqslant 90$ show that the strength distribution for ISGMR can be described with a Gaussian. The centroid of the Gaussian (E_{ISGMR}) for nuclei with $A \geqslant 90$ can be approximated as [4]:

$$E_{ISGMR} = 80A^{-1/3}\ \text{MeV} \tag{2.1}$$

The isoscalar dipole oscillation depicted in Fig.1.2 corresponds to a spurious CM motion. The real Isoscalar Giant Dipole Resonance (ISGDR) is a higher-order oscillation, called the "*squeezing mode*". It displays oscillations wherein the density increases on one side of the nucleus and decreases on the other side with a slight change in shape keeping the center-of-mass fixed. The centroid energy of ISGDR (E_{ISGDR}) can be approximated as [4]:

$$E_{ISGDR} = 100 - 120A^{-1/3}\ \text{MeV} \tag{2.2}$$

The strength distribution in case of ISGDR is extended over 10 MeV [4].

In both cases of ISGMR and ISGDR, there is a change of density of the nuclear matter. Therefore, these two modes are referred to as *compression modes* and are depicted in Fig. 2.1.

For comparison, Isoscalar Giant Quadrupole Resonance (ISGQR) is also depicted in Fig. 2.1. ISGQR corresponds to an axial deformation of nuclear fluid with no change in density. In lighter nuclei, the strength distribution for ISGQR is fragmented whereas for A larger than $\sim$64, the centroid energy of ISGQR (E_{ISGQR}) can be approximated as [4]:

$$E_{ISGQR} = 64.7A^{-1/3}\ \text{MeV} \tag{2.3}$$

2.2 Microscopic model

Microscopic models have been developed to understand the nuclear structure and in particular GRs. These microscopic models are usually based on a *mean-field* concept where the nucleons are considered to move independently in a mean field generated by the two-body interaction between all nucleons in addition to a small residual interaction. Although in principle, one can calculate the effective interaction from the bare nucleon-nucleon force, but for the sake of simplicity, the effective interaction is written in terms of phenomenological forces (e.g. Skyrme or Gogny type of interaction).

One such microscopic calculation is based on the Hartree-Fock (HF) method. In this method, one assumes that the ground state of the nucleus is approximated by a single Slater determinant of single-particle orbitals where all the states below the Fermi surface are completely

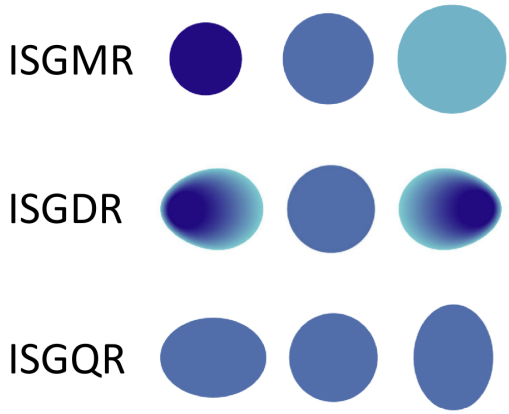

Figure 2.1: Oscillation of the nucleus about an equilibrium shape shown for ISGMR (top), ISGDR (middle) and ISGQR (bottom). The ISGMR (breathing mode) and the ISGDR (squeezing mode) display density variations and, are therefore, denoted as the compression modes. The ISGQR displays no density variations; only change in shape occurs.

filled and above the Fermi surface are completely empty. In the HF method, a *np-nh* state can be created by promoting n particles to states above the Fermi level from the states below the Fermi level. For constructing GR excitations, one has to take into account the coherent superposition of *1p-1h* transitions [4].

Nowadays, the commonly used microscopic calculation is based on Random-Phase Approximation (RPA) in which a correlated ground state of the nucleus is considered, including admixtures of *0p-0h*, *2p-2h* and higher-order configurations. Pairing correlations for open-shell nuclei can also be taken into account in the RPA formalism. In RPA, the excited state of a system can be represented by a creation operator $\hat{\Gamma}^{\dagger}_{\nu}$ acting on the correlated ground state [4]:

$$|\nu\rangle = \hat{\Gamma}^{\dagger}_{\nu}|0\rangle \tag{2.4}$$

and the ground state of the system is defined as [4]:

$$\hat{\Gamma}_{\nu}|0\rangle = 0 \tag{2.5}$$

In the lowest-order RPA, only *1p-1h* excitations are considered and the boson creation operator $\hat{\Gamma}^{\dagger}_{\nu}$ can be defined as [4]:

$$\hat{\Gamma}^{\dagger}_{\nu} = \sum_{p,h} (X^{\nu *}_{ph}\, a^{\dagger}_{p}\, a_{h} - Y^{\nu *}_{ph}\, a^{\dagger}_{h}\, a_{p}) \tag{2.6}$$

where $a^{\dagger}_{p(h)}$ is the creation operator for the particle (hole) state and $a_{p(h)}$ is the annihilation operator for the particle (hole) state. The amplitudes $X^{\nu *}_{ph}$ and $Y^{\nu *}_{ph}$ can be obtained from the particle-hole excitations under consideration.

In RPA, the transition matrix elements for an operator $\hat{O}$ ($\hat{O} = \sum_{kl} O_{kl}\, a^{\dagger}_{k}\, a_{l}$) between the ground state $|0\rangle$ and the excited state $|\nu\rangle$ is given by [4]:

$$\langle \nu | \hat{O} | 0 \rangle = \sum_{p,h} \{ X^{\nu *}_{ph}\, O^{*}_{ph} + Y^{\nu *}_{ph}\, O_{hp} \} \tag{2.7}$$

The moment of an electric multipole transition can be expressed in terms of spherical Bessel function. Depending on the multipolarities of the isoscalar giant resonances, either the first-order term or the second-order term of the expansion of the Bessel function should be considered. In case of ISGMR ($L = 0$), the first-order term is a constant. In case of ISGDR ($L = 1$), the first-order term corresponds to a translational motion of the whole nucleus and it is not an intrinsic nuclear excitation. Therefore, the transition operators for the isoscalar electric giant resonances can be written as:

$$\begin{aligned} \hat{O}_{L} &= \sum_{i=1}^{A} r_{i}^{L}\, Y_{LM}(\Omega_{i}), \qquad L \geqslant 2 \\ \hat{O}_{L} &= \frac{1}{2} \sum_{i=1}^{A} r_{i}^{L+2}\, Y_{LM}(\Omega_{i}), \qquad L < 2 \end{aligned} \tag{2.8}$$

with $Y_{LM}(\Omega_{i})$ being the spherical harmonics. The qualitative features of giant resonances can be understood from a schematic shell-model picture as shown in Fig. 2.2. The parity of the single-particle wave functions in the subsequent shells N, $N+1$, $N+2$, ... are alternating. Due to parity conservation, odd multipolarity transitions require ΔN = 1, 3, ... and even multipolarity transitions require ΔN = 0, 2, ... However, $0\hbar\omega$ transition is not possible for ISGMR because of angular-momentum conservation. In this model, the energy difference between two major shells is [4]:

$$\Delta E = \Delta N \times 1\hbar\omega = \Delta N \times 41 A^{-\frac{1}{3}}\ \text{MeV} \tag{2.9}$$

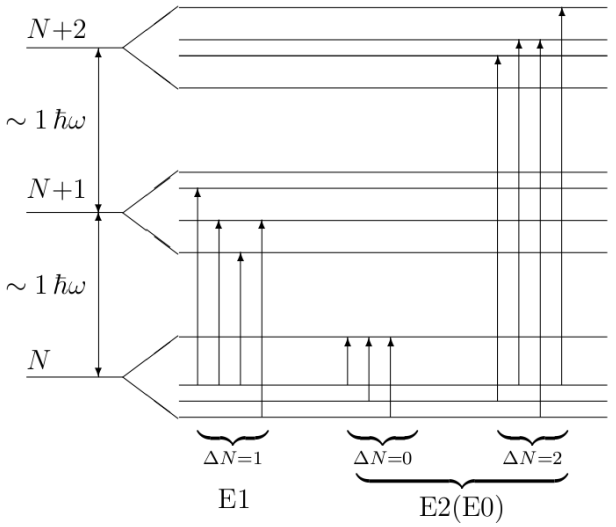

Figure 2.2: Schematic picture of E1 and E2 (E0) single-particle transitions between shell-model states [4].

Since the residual particle-hole interaction is attractive for isoscalar excitations and repulsive for isovector excitations, the isoscalar resonances will be located below and the isovector resonances will be located above the corresponding unperturbed energies $\Delta N \times 41 A^{-\frac{1}{3}}$ MeV. In fact, it has been found experimentally that ISGQR and IVGDR are located nearly at same excitation energy. Therefore, it is necessary to use specific probes to disentangle the overlapping resonances.

2.3 Sum rules

The strength function of a transition can be obtained from the transition matrix elements from Eqn. 2.7:

$$S_F(E) = \sum_{\nu} |\left\langle \nu|\hat{O}|0\right\rangle|^2 \, \delta(E - E_\nu) \tag{2.10}$$

where $\hat{O}$ is the transition operator between the ground state $|0\rangle$ and the excited state $|\nu\rangle$ at energy E_ν. One can define the n^{th} moment of the strength distribution by [31]:

$$m_n = \sum_\nu (E_\nu - E_0)^n \mid \langle \nu | \hat{O} | 0 \rangle \mid^2 \tag{2.11}$$

The sum turns into an integral for continuum states. By taking appropriate ratios of these moments, one can obtain various estimations for the energy of the monopole vibration. The first-order moment m_1 can be written as [32]:

$$m_1 = \sum_\nu (E_\nu - E_0) \mid \langle \nu | \hat{O} | 0 \rangle \mid^2 \tag{2.12}$$

This first-order moment is used to characterize the giant resonances and is defined as the Energy-Weighted Sum Rule (EWSR). It can be evaluated independently of the models and for isoscalar resonances depends only on the ground-state properties of the nucleus. A giant resonance state exhausts almost all of the transition strength. Usually for heavier nuclei with $A \geq 90$, the giant resonance state exhausts about 100% of the EWSR whereas for lighter nuclei it exhausts 50-100% of the EWSR.

2.4 Damping of giant resonances

2.4.1 Width of the resonances

The GRs are characterized by their broad widths. The total width of the giant resonance can be defined as [4]:

$$\Gamma_{total} = \Gamma_{inh} + \Gamma^{\downarrow} + \Gamma^{\uparrow} \tag{2.13}$$

where Γ_{inh} is the *inherent* width, $\Gamma^{\downarrow}$ is the *spreading* width and $\Gamma^{\uparrow}$ is the *escape* width. Among these, the *spreading* width gives the largest contribution to the total width.

The *inherent* width (commonly called Landau damping) is due to the spreading in excitation energy of the initial collective *1p-1h* transitions. Such a spreading can be caused by many non-collective *1p-1h* transitions whose energies are close to the energy of the collective state.

The *spreading* width arises from the coupling of the *1p-1h* configurations with the *2p-2h*, *3p-3h* and higher-order configurations. For the theoretical understanding of the *spreading* width, RPA calculations are required where the admixtures of *2p-2h* and higher-order configurations are considered.

The *escape* width can be understood from the decay of the giant-resonant state. In general,

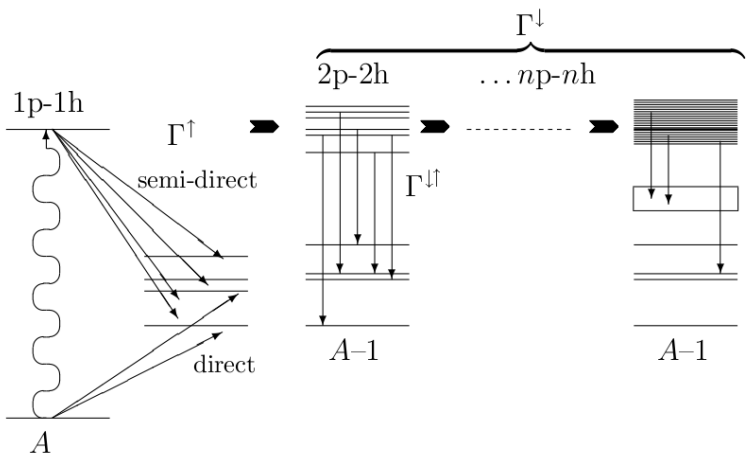

Figure 2.3: Schematic picture of the width of the collective (*1p-1h*) state into a direct component $\Gamma^{\uparrow}$ and a spreading component $\Gamma^{\downarrow}$ [4].

the collective *1p-1h* state is well above the particle-emission threshold. Therefore, the state acquire a width through particle emission. In principle, the *2p-2h*, ... states can also decay by particle emission which is denoted as $\Gamma^{\downarrow\uparrow}$. In Fig. 2.3, the processes which lead to the GR state acquiring a width are illustrated schematically.

2.4.2 Decay of giant resonances

Since the GR states are well above the particle emission threshold, their properties can be determined by studying their particle decay. The spin and parity of the GR state can also be determined by looking into the angular correlations between the ejectile and the decay particle [33, 34]. Furthermore, since GRs are sitting on top of a continuum, the background can be eliminated by performing coincidence measurements between the ejectile from the GR excitation process and the decay particles (neutron, proton, α, γ) [35, 36].

2.5 Nuclear incompressibility

The incompressibility of nuclear matter (K_∞) is a basic quantity like saturation density (ρ_0) or Fermi momentum (k_F). It can be defined as the curvature of the binding energy per

particle at the saturation density (ρ_0) and can be written as [37]:

$$K_\infty = 9\rho_0^2 \frac{d^2(E/A)}{d\rho^2}\bigg|_{\rho_0} \tag{2.14}$$

Nuclear incompressibility is an important ingredient in the equation of state of nuclear matter. Its value enters into the analysis of astrophysical phenomena such as masses of neutron stars and explosion of supernovae. However, unlike the equilibrium density, the value of nuclear incompressibility cannot be measured directly. It turns out that the best way to determine K_∞ is from the strength distributions of the ISGMR and the ISGDR which can be experimentally accessed. The centroid energies of the ISGMR and ISGDR, the so-called compression modes, are given in the constrained and scaling models as [38]:

$$E_{ISGMR} = \hbar\sqrt{\frac{K_A}{m < r^2 >}} \tag{2.15}$$

$$E_{ISGDR} = \hbar\sqrt{\frac{7}{3}\frac{K_A + \frac{27}{25}\epsilon_F}{m < r^2 >}} \tag{2.16}$$

where E_{ISGMR} and E_{ISGDR} are the centroid energies of ISGMR and ISGDR, respectively, m is the nucleon-mass, $\langle r^2 \rangle$ is the mean-square nuclear radius and ϵ_F is the Fermi energy. One can see that if the excitation energies of the compression modes increase the nucleus becomes harder. In the above equations, K_A is the nuclear incompressibility for a finite nucleus. Following the liquid-drop model concepts, K_A can be expanded as follows [39]:

$$K_A = K_\infty + K_{surf}A^{-1/3} + K_\tau\left(\frac{N-Z}{A}\right)^2 + K_{coul}Z^2A^{-4/3} \tag{2.17}$$

where K_∞ is the volume term and is the nuclear incompressibility for infinite nuclear matter. K_{surf}, K_τ and K_{coul} are surface, neutron-proton asymmetry and Coulomb terms, respectively. However, in this model, the values of K_∞ from the fit of the data using Eqn. 2.17 do not converge to a unique solution but a good fit can be obtained giving values of K_∞ ranging from 100 MeV to 400 MeV [32, 40].

The microscopic calculations of nuclear incompressibility depend on the possibility of constructing sets of effective interactions, e.g., Skyrme or Gogny interactions. These effective interactions can reproduce well the nuclear properties such as binding energy, Fermi mo-

mentum and charge radius. By calculating the energy of the breathing mode with such effective interactions, one can correlate the value of K_A for a nucleus with the corresponding value of K_∞ in nuclear matter.

The value of K_∞ obtained from the ISGMR & ISGDR data is 240$\pm$10 MeV [41–44]. The effective interactions mentioned above can reproduce well the centroid energies of the ISGMR for ^{90}Zr, ^{144}Sm and ^{208}Pb [45]. However, the same effective interactions overestimate the centroid energies for ISGMR strength distributions for Sn [46, 47] and Cd [48] isotopes, although they can reproduce well the ground-state properties for Sn and Cd isotopes. In spite of significant theoretical efforts to reproduce simultaneously the ISGMR centroid energies in ^{90}Zr, ^{208}Pb and in Sn/Cd isotopes, no single approach has emerged. Therefore, in order to help solving the mystery *why Sn or Cd isotopes are fluffy* [46–48], it is necessary to study compression modes for another series of isotopes. Since Ni isotopes have astrophysical implications, efforts have been put to study in details the compression modes for several stable and unstable isotopes of Ni from the proton-rich to neutron-rich regions of the nuclear chart.

2.6 Giant resonances in Ni isotopes

2.6.1 Theoretical predictions

Giant resonances have been extensively studied for stable isotopes. But for exotic nuclei there is little information available. To understand different terms in Eqn. 2.17 and especially the term K_τ, the asymmetry term, one has to study the giant resonances over an isotopic chain of an element. In Figs. 2.4, 2.5 and 2.6, the theoretical predictions for GMR, GDR and GQR for both isoscalar and isovector modes for even-A Ni isotopes from the proton-drip line to the neutron-drip line are given. The calculations were done using quasi-particle RPA (QRPA) with a three types of Skyrme interactions (SkM*, Skp and Sly4). The results for different Skyrme interactions are essentially very similar [49].

In Fig. 2.4, the 0^+ strength functions for isoscalar and isovector modes are given for Skyrme interaction of type SkM*. The IS giant resonance peaks at $\sim$20 MeV and gradually moves to $\sim$15 MeV as N, the number of neutrons, increases. The isovector giant resonance is broad in the light isotopes and develops a low-energy component as N gets larger.

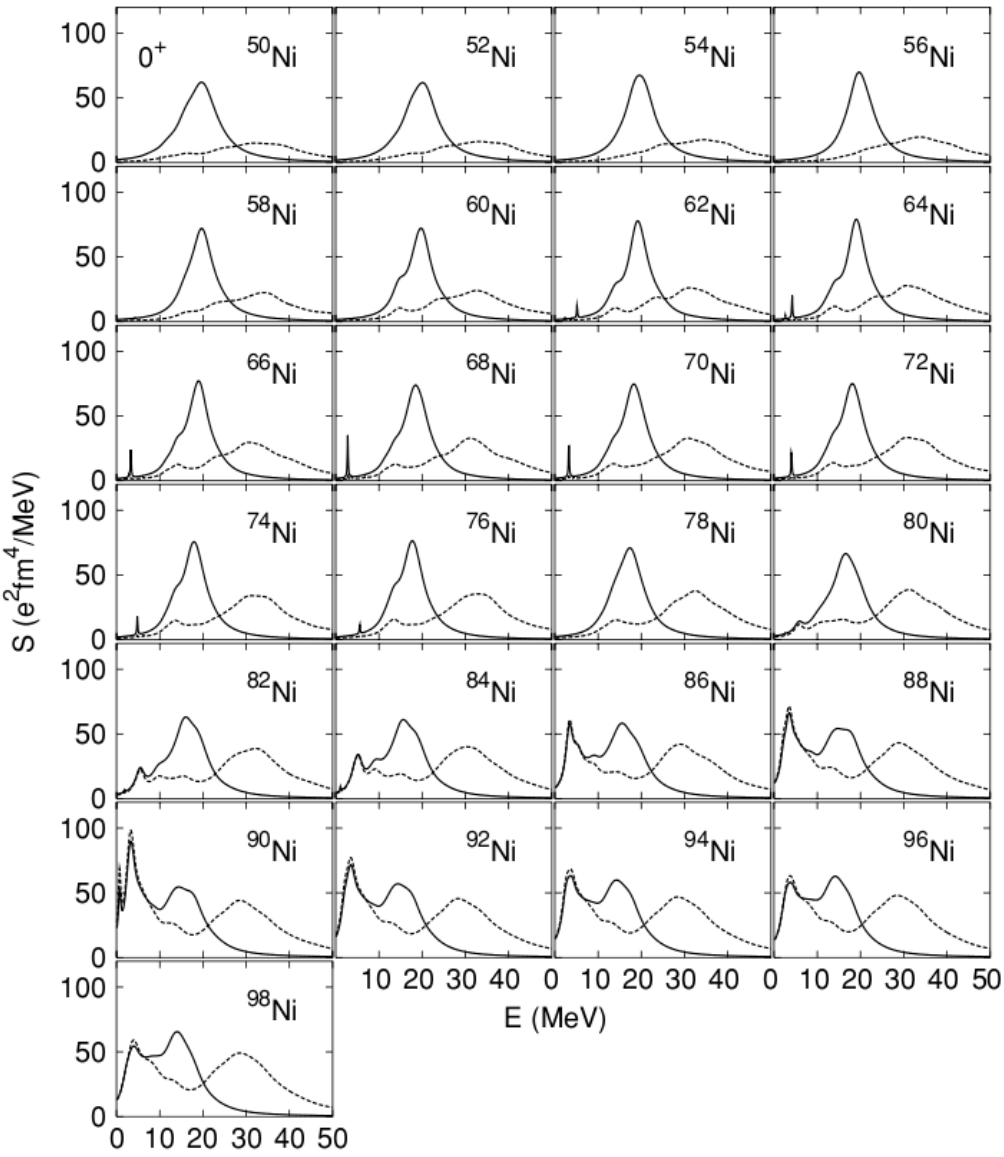

Figure 2.4: E0 strength functions for even-A Ni isotopes. The solid line refers to isoscalar modes and the dashed line refers to isovector modes [49].

In Fig. 2.5, the 1^- strength functions for isoscalar and isovector modes are given for Skyrme interaction of type SkM*. The IS giant resonance peak appears around $\sim$30 MeV and devel-

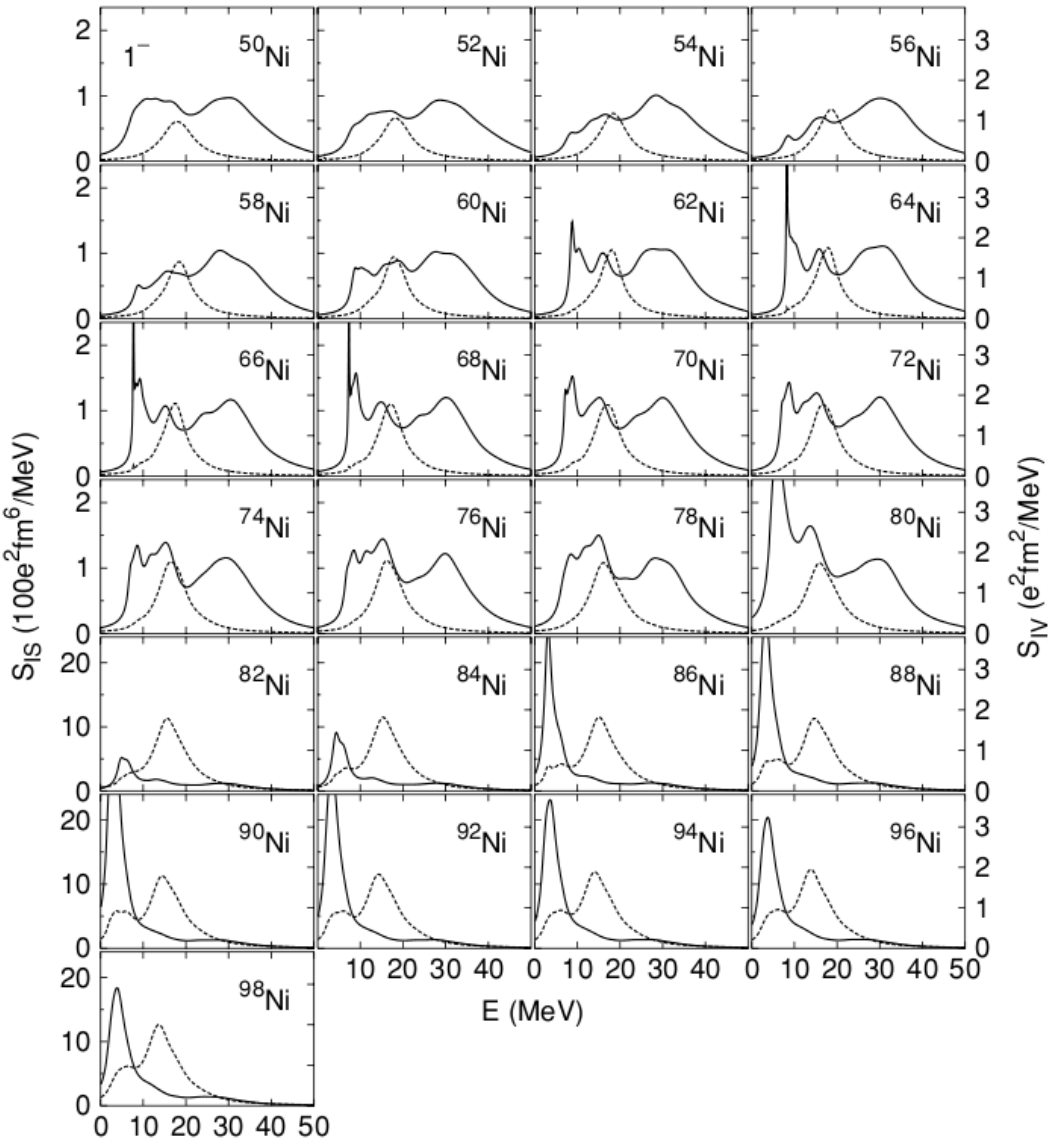

Figure 2.5: Same as Fig. 2.4 but for E1 [49].

ops a low-energy component as N increases. The IV giant resonance peak appears around $\sim$16 MeV.

In Fig. 2.6, the 2^+ strength functions for isoscalar and isovector modes are given for Skyrme

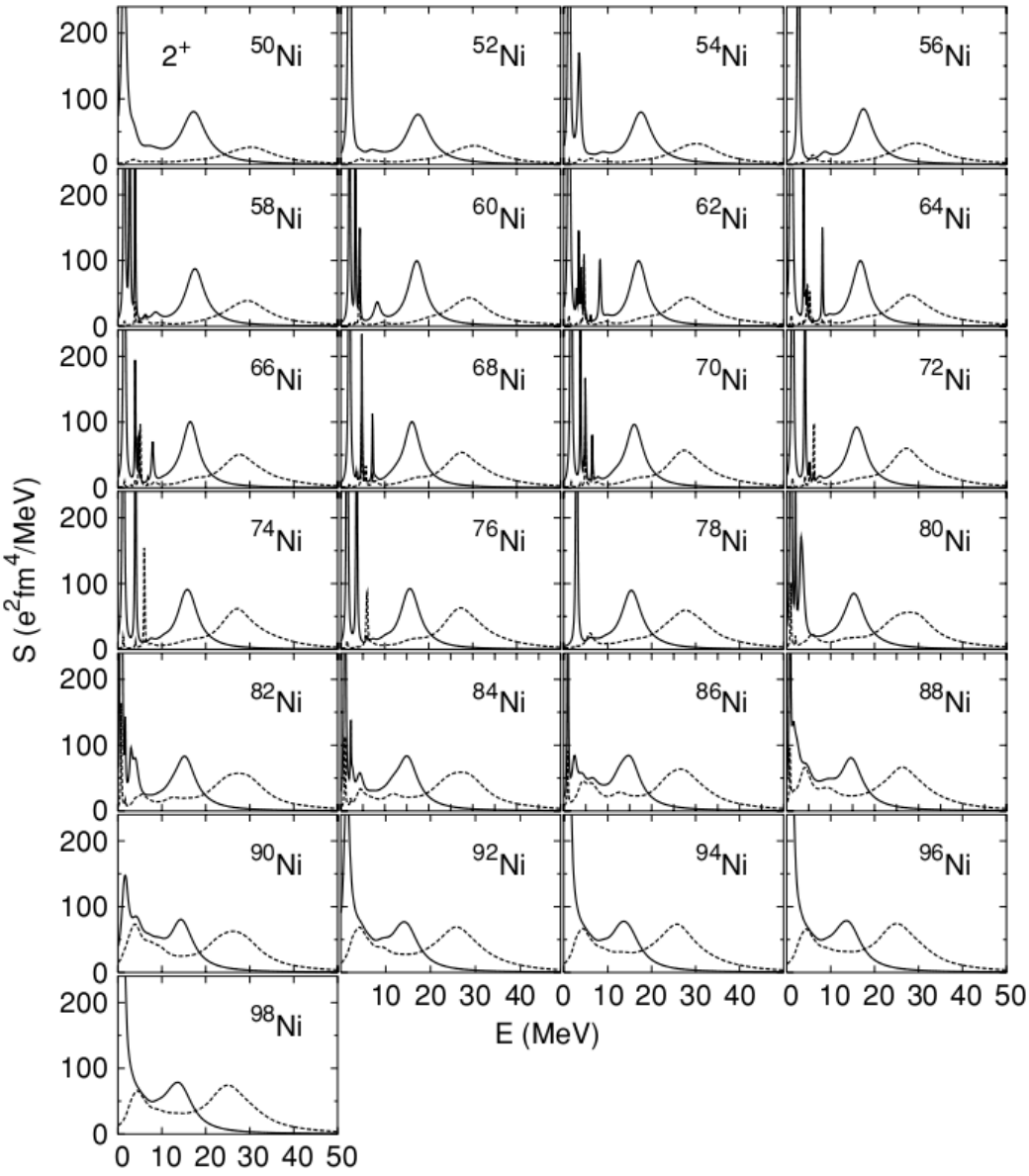

Figure 2.6: Same as Fig. 2.4 but for E2 [49].

interaction of type SkM*. The IS giant resonance peak appears around ∼16 MeV and decreases to lower energy as N increases. The isovector resonance peak appears to be around

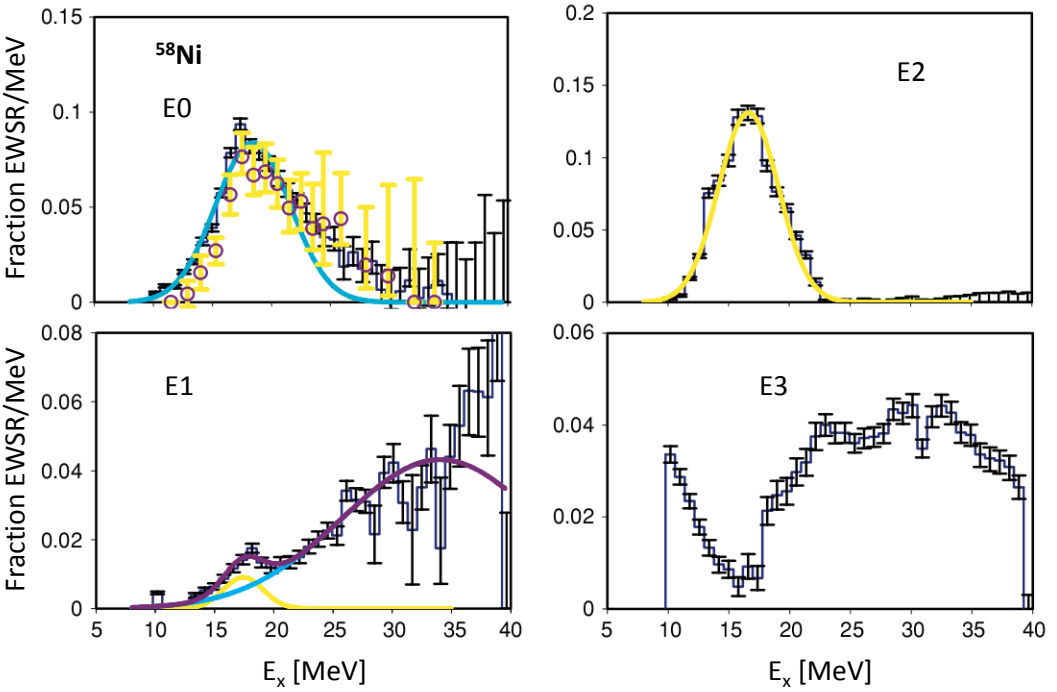

Figure 2.7: $E0$, $E1$ and $E2$ strength distributions are shown for ^{58}Ni. $E3$ distribution includes all $L \geq 3$ strengths [50]. The curves represent the Gaussian fitting to the data. The open circles in the $E0$ strength distribution are from Ref [51].

$\sim$30 MeV and decreases as N increases.

2.6.2 Experimental evidences

Previous studies from Texas A&M University [50] of the giant resonance regions in stable ^{58}Ni and ^{60}Ni isotopes were performed with inelastic scattering of α-particles at an incident beam energy of 240 MeV. In Fig. 2.7, the strength functions for $E0$, $E1$, $E2$ and $E3$ isoscalar transitions are shown for ^{58}Ni. In Fig. 2.8, the strength functions for $E0$, $E1$, $E2$ and $E3$ isoscalar transitions are shown for ^{60}Ni.

ISGMR, ISGDR and ISGQR in ^{58}Ni have also been studied by Nayak et al. [52] at RCNP with inelastic α-particle scattering at 386 MeV incident energy. In both cases, the centroid energies

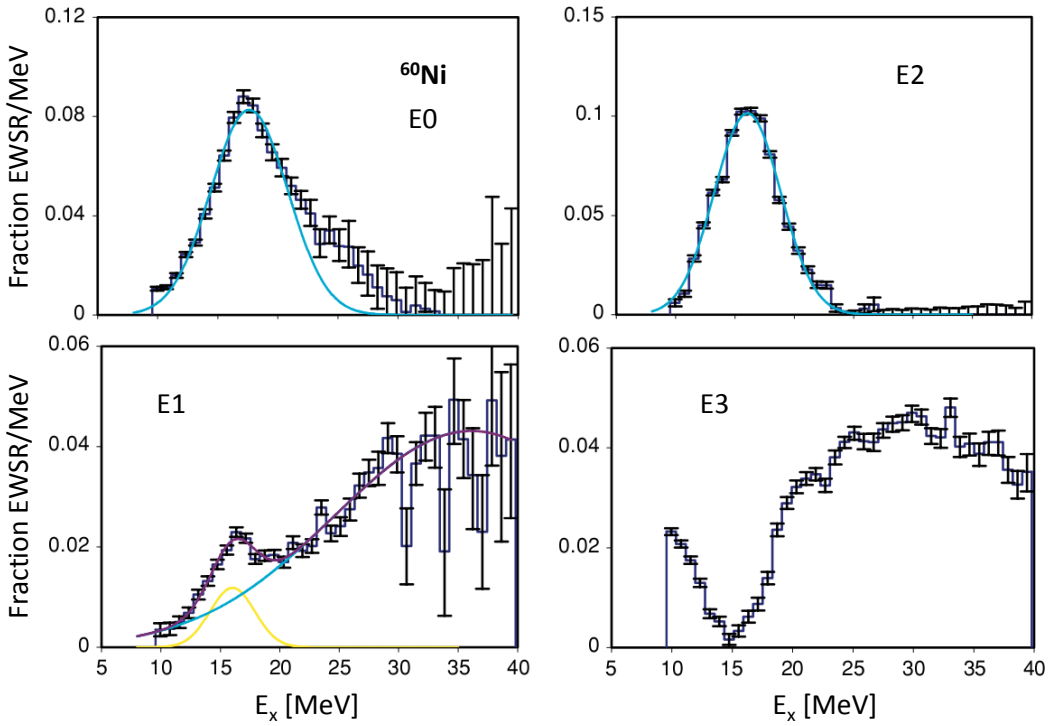

Figure 2.8: Same as Fig. 2.7 but for ^{60}Ni [50]. The curves represent the Gaussian fitting to the data.

of ISGMR and ISGQR have been found to be around 19 MeV and 16 MeV, respectively. In case of ISGDR, there is evidence for a "bi-modal" strength distribution for ^{58}Ni and ^{60}Ni with the high-energy peak appearing around $\sim$30 MeV.

ISGMR and ISGQR for the exotic neutron-deficient nucleus ^{56}Ni have been studied by Monrozeau et al. [53], by inelastic deuteron scattering in inverse kinematics with a ^{56}Ni beam at an incident energy of 50 MeV/u. The experiment was performed at the GANIL facility using the active target MAYA. In the left panel of Fig. 2.9, the efficiency corrected excitation energy is shown with the Gaussian fits for ISGQR and ISGMR. In the right panel of Fig. 2.9, the cross sections obtained from the Gaussian fits are shown. The excitation energy of ISGMR has been found to be 19.3 $\pm$ 0.5 MeV with almost 136% exhaustion of the EWSR. The excitation energy of ISGQR has been found to be 16.2 $\pm$ 0.5 MeV with almost 76% exhaustion of the EWSR.

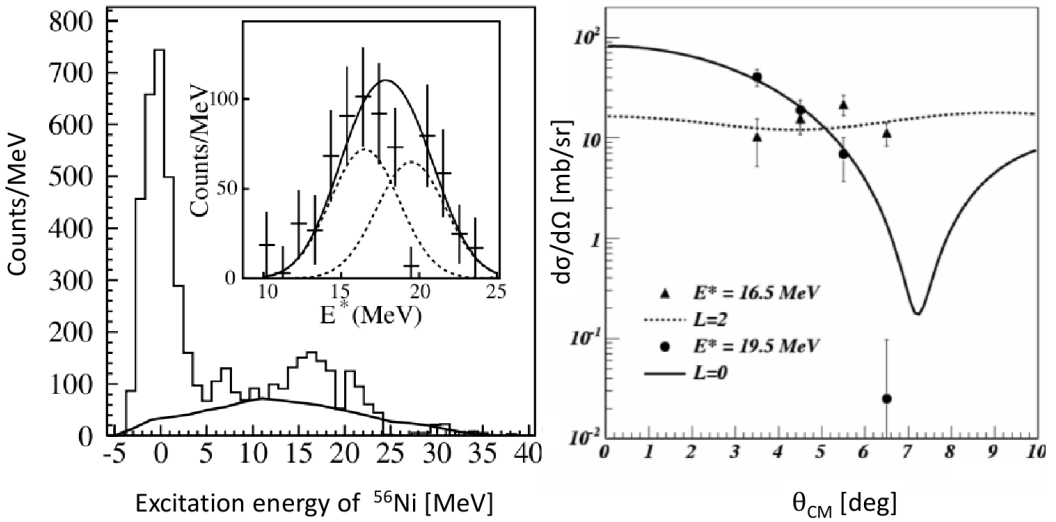

Figure 2.9: Left panel: ^{56}Ni excitation-energy spectrum corrected for geometrical efficiencies. The background due to deuteron break-up is shown by the solid line. The inset shows the background subtracted inelastic data fitted with Gaussian distributions located at 16.5 MeV and 19.5 MeV for the ISGQR and ISGMR, respectively. Right panel: cross sections for ISGQR (triangles) and ISGMR (filled circles) obtained from the Gaussian fits [53].

Giant resonances have also been studied for neutron-rich ^{68}Ni by Vandebrouck et al. [54], by inelastic α-particle and deuteron scattering in inverse kinematics with a ^{68}Ni beam at an incident energy of 50 MeV/u. This experiment was also performed at the GANIL facility using active target MAYA. In Fig. 2.10, the total excitation-energy spectrum of ^{68}Ni and excitation-energy spectrum of ^{68}Ni at 5.5° CM angle are shown with the Lorentzian fits for ISGMR, ISGQR and also for the soft-monopole mode which reflects the collectivity due to extra neutrons relative to protons. In the right side of Fig. 2.10, the angular distributions obtained from the Lorentzian fits are also shown for the soft-monopole mode and the ISGMR. The excitation energy of ISGMR for ^{68}Ni from the Lorentzian method has been found to be 21.1 $\pm$ 1.9 MeV. For comparison of the results obtained from different experiments see Chapter 6.

2.7 Theoretical predictions for angular distributions

Theoretical predictions of the angular distributions for the ISGQR, ISGMR and ISGDR are necessary to identify the nature of the GRs excited in the inelastic α-scattering experiments.

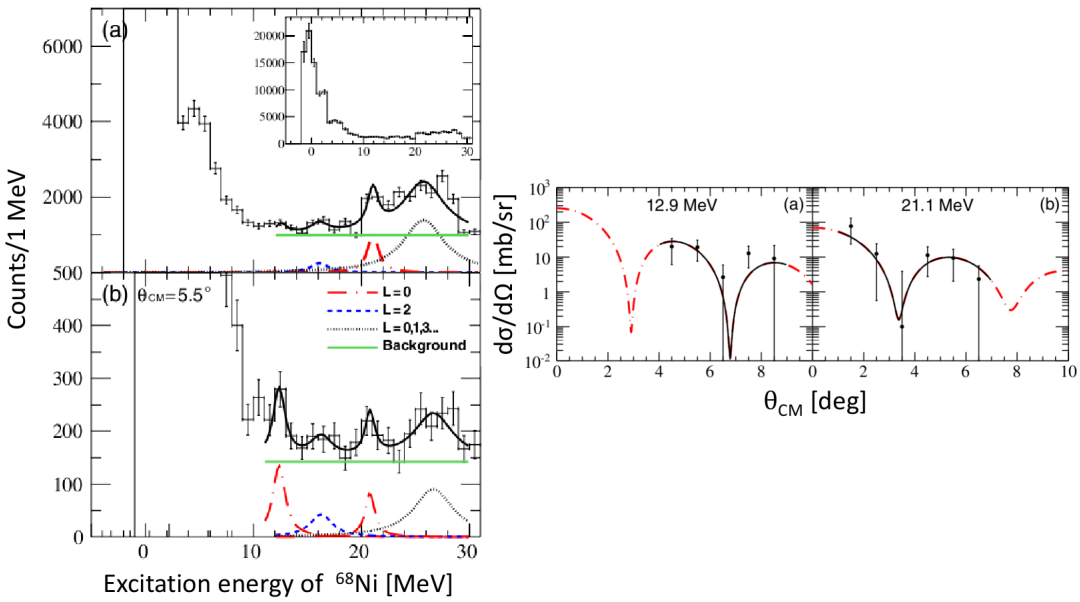

Figure 2.10: Left panel: (a) ^{68}Ni excitation-energy spectrum for all angles deduced from the alpha recoil kinematics and corrected for geometrical and reconstruction efficiencies. (b) Same for $\theta_{CM} = 5.5°$. For both spectra, the subtracted background is indicated by the horizontal green solid line. The data were fitted with Lorentzians at 12.9 MeV (red dot-dashed line), 15.9 MeV (blue short-dashed line) and 21.1 MeV (red dot-dashed line) for the low-energy mode, the ISGQR and the ISGMR, respectively. Right panel: Angular distributions for the modes located at 12.9 MeV (a) and 21.1 MeV (b). The black solid line corresponds to the fit based on DWBA calculation using microscopic RPA predictions with isoscalar $L = 0$ multipolarity. These predictions are represented by red dot-dashed lines [54].

Here, they have been made in the framework of the Distorted-Wave Born Approximation (DWBA). This formalism will be only briefly detailed since the aim is to present the conditions under which the calculations were performed. Details of the method can be found in Refs. [4, 55].

2.7.1 General formalism

To describe the scattering process one needs to solve the time-dependent Schrödinger equation using Fermi's Golden rule. In this case, it is assumed that the potential vanishes faster than $1/r$ for large r, where r is the spatial coordinate. Since the incident particles are monoenergetic, the incident wave can be considered as a plane wave. The scattered particle can be considered as an outgoing spherical wave. The scattering wave function must fulfill the

boundary conditions, i.e., being finite at the origin and showing asymptotic behavior at large r. The scattering wave function is given by:

$$\psi(\mathbf{k},\mathbf{r}) \xrightarrow{r\to\infty} e^{i\mathbf{k}.\mathbf{r}} + f(\theta,\phi)\frac{e^{ikr}}{r} \tag{2.18}$$

where $\mathbf{r}$ is the spatial vector, $\mathbf{k}$ is the wave vector and $e^{i\mathbf{k}.\mathbf{r}}$ is the incoming plane wave. The second term on the right hand side of Eqn. 2.18 represents the outgoing spherical wave where $f(\theta,\phi)$ is the scattering amplitude. The differential cross section is simply the square of the scattering amplitude:

$$\frac{d\sigma}{d\Omega} = |f(\theta,\phi)|^2 \tag{2.19}$$

2.7.2 The optical potential

In the optical model, the potential is referred to as *optical potential*. In the case of α-particles (spin 0), it contains real and imaginary volume potentials and can be defined as:

$$U(r) = V(r) + iW(r) \tag{2.20}$$

where $V(r)$ is the real potential and it corresponds to the coupling to the elastic channel where there is no change in particle flux in the output channel. $W(r)$ is the imaginary part and it arises because of the coupling to all non-elastic channels (e.g., inelastic scattering, transfer reactions etc.). A potential well of the Woods-Saxon type [56] is usually taken for both the real and imaginary terms and is given for the real potential by:

$$V(r) = -V_o f(r) = -\frac{V_o}{1 + exp(\frac{r-R}{a})} \tag{2.21}$$

where V_o is the depth of the potential, R its radius and a its diffuseness. The parameters are adjusted in a way that the cross-sections calculations for the elastic scattering and the first excited state of ^{58}Ni agree with the experimental data. Clark et al. [57] measured the α-particle elastic scattering and inelastic scattering differential cross sections for ^{58}Ni. By fitting the data, they obtained the optical-potential parameters which are listed in Table 2.1. The same parameter values have been used in this thesis to obtain the angular distributions of the GRs in ^{56}Ni, since 240 MeV total energy for the α-particle corresponds to 60 MeV/u

E_α	240 MeV
V_{o_R}	76.6 MeV
V_{o_I}	24.2 MeV
R_R	4.75 fm
R_I	5.49 fm
r_C	1.3 fm
a_R	0.8 fm
a_I	0.8 fm

Table 2.1: Optical-model parameters obtained by Clark et al. [57].

which is not that different from the 50 MeV/u beam energy used for the experiment presented in this thesis. Furthermore, ^{56}Ni is nearly equal to ^{58}Ni.

2.7.3 DWBA approximation

The DWBA is an approximation that takes into account the first-order coupling between the initial state and final state as well as the effect of the distortion of the incident wave and the scattered wave due to the optical potential acting between the projectile and the target. The transition matrix element between the initial state i (^{56}Ni and α-particle) and the final state f (scattered ^{56}Ni and recoiled α-particle) can be written as [58]:

$$T_{fi} \propto \int \chi_f^{(-)}(\vec{r}) \, \langle f|\delta U(\vec{r})|i\rangle \, \chi_i^{(+)}(\vec{r}) d\vec{r} \tag{2.22}$$

where $\vec{r}$ is the relative position between the target and the projectile. $\chi_f^{(-)}$ and $\chi_i^{(+)}$ are the distorted waves for the output channel (after scattering) and input channel (before scattering), respectively. $\delta U(\vec{r})$ is the perturbed potential caused by the residual interaction and is responsible for inelastic excitations of the nucleus after the scattering. The matrix element $\langle f|\delta U(\vec{r})|i\rangle$ contains all the information about the structure of the initial state and the final state and the interaction responsible for the transition. From the transition matrix element, it is easy to calculate the differential cross section:

$$\frac{d\sigma}{d\Omega} = \left(\frac{\mu}{2\pi\hbar^2}\right)^2 \frac{k_i}{k_f} \, |T_{fi}|^2 \tag{2.23}$$

where μ is the reduced mass of the target and the projectile, k_i and k_f are the incoming and

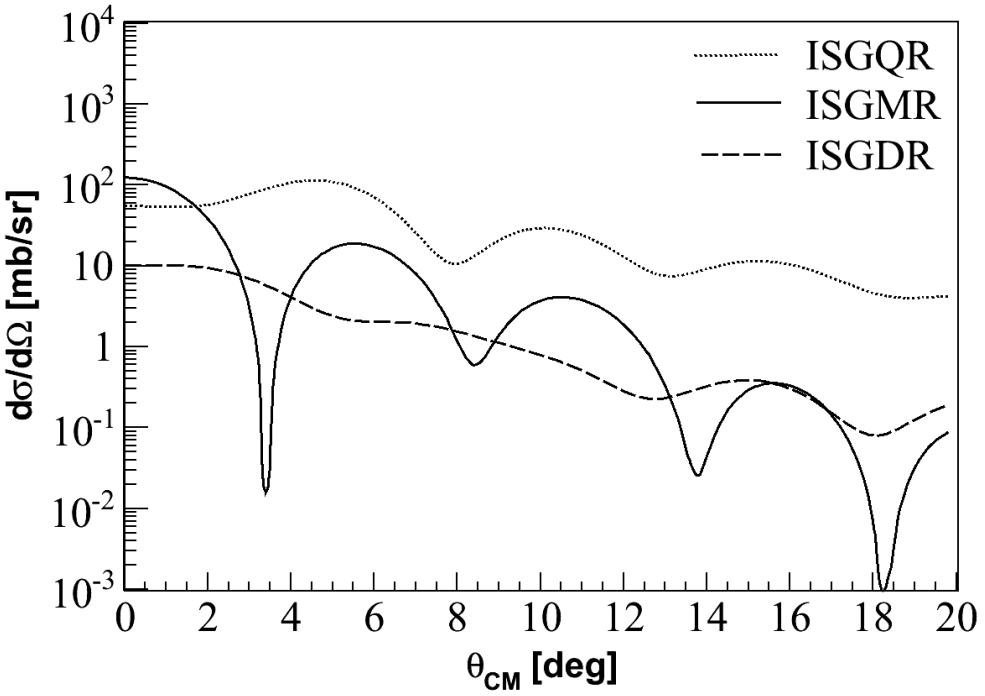

Figure 2.11: DWBA calculations for ISGMR, ISGDR and ISGQR as described in the text.

outgoing wave numbers.

2.7.4 DWBA for ^{56}Ni(α, α')^{56}Ni* reaction

The centroid energy of ISGQR in ^{56}Ni is located around 16.5 MeV [53], the centroid energy of ISGMR in ^{56}Ni is located around 19.5 MeV [53], and the centroid energy of ISGDR (with $\geq$ 50% EWSR exhausted) in ^{58}Ni is located around 30.5 MeV [52]. DWBA calculations are performed for ^{56}Ni(α, α')^{56}Ni* reaction considering the excitation energy of ^{56}Ni to be at 16.5 MeV, 19.5 MeV and 30.5 MeV for ISGQR, ISGMR and ISGDR, respectively. In these calculations, it has been assumed that there is 100% exhaustion of the EWSR. The results are shown in Fig. 2.11.

The DWBA calculations were performed using the CHUCK3 code [59]. The parameters of the optical potential used to calculate the cross sections are listed in Table 2.1. As can

be seen from Fig. 2.11, we have to measure the cross sections of the giant resonances at forward angles because as the CM angle increases the cross section diminishes by orders of magnitude. Furthermore, the angular distributions at forward angles are characteristic of the multipolarity. For example, to measure the ISGDR, it is good to measure it between 3° and 4° CM angle where it is the first minimum of the ISGMR cross section. The forward-angle measurement leads to detection of recoil α-particles having energies less than $\sim$5 MeV. Since the active target MAYA has low detection threshold, it is best suited to study the compression modes, i.e., ISGMR and ISGDR in ^{56}Ni.

Chapter 3

Experimental Setup

This chapter describes the experimental setup at the GANIL laboratory, Caen, France. This experiment used a secondary beam that was produced and purified using the LISE spectrometer. The main component of the experimental setup is the active target detector MAYA. In this chapter a brief overview of the GANIL facilities used during the experiment followed by a detailed description of the active target MAYA and its components will be given. This chapter ends with an explanation of the electronics layout used during the experiment.

3.1 Experimental method and associated constraints

From Chapter 2, we have seen that in order to study the ISGMR and the ISGDR of ^{56}Ni we need to study inelastic α-scattering at forward center-of-mass (CM) angles. For the ISGDR, it would be useful to study the inelastic scattering as low as 2° CM angle (see Fig. 2.11). Since this experiment has to be performed in inverse kinematics, i.e., ^{56}Ni beam is scattered from helium in MAYA, the recoil α-particles have to be detected at an energy as low as 2 MeV. For the ISGMR and the ISGDR it would be sufficient to study the inelastic scattering below 4° CM angle. Nevertheless, the goal is to reconstruct the excitation energies of ^{56}Ni, including the ISGDR and beyond, upto 90° scattering angle in the laboratory frame. Therefore, it is imperative to use a detector which has a low detection threshold of energy and a good angular coverage.

In order to detect the very low-energy recoil particles, an active target, where the target acts as a detector, is suitable. In our setup, we have used the MAYA active target detector: it is a time and charge projection chamber filled with gas that serves both as the target and the

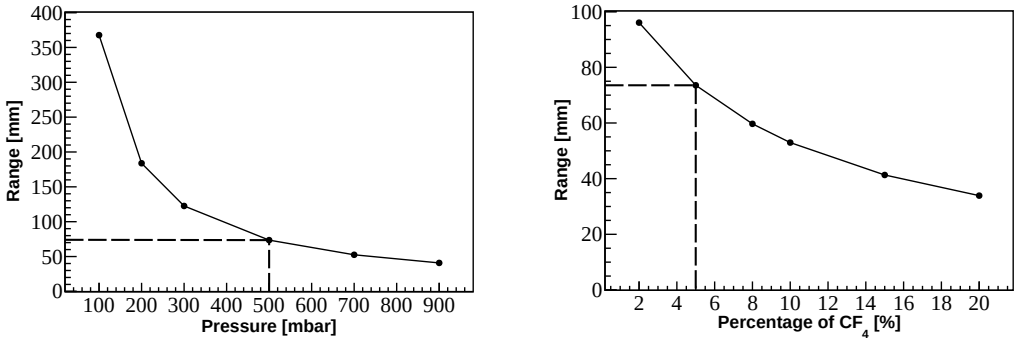

Figure 3.1: Range of 2 MeV α-particle as a function of pressure of 95% He and 5% CF_4 gas mixture (left panel) and of percentage of CF_4 in the gas mixture at 500 mbar pressure (right panel). Calculations were performed using the SRIM program [61].

detector. The other advantages of the active target detector are; i) the solid angular coverage, which is close to 4π, and ii) the target thickness that can be increased to enhance the yield of the reaction without much loss of energy resolution. A detailed description of the MAYA detector along with its working principle will be presented in the Section 3.3.

To study the inelastic scattering of α-particles with ^{56}Ni, MAYA was filled with helium gas. Since pure helium can not be used because of sparking, we used CF_4 as a quencher [60]. The pressure of the gas mixture inside MAYA and also the percentage of CF_4 should be adjusted in such a way that the low-energy recoil α-particles have a measurable range with least amount of contamination from CF_4. Therefore, MAYA was filled with 95% He and 5% CF_4 at a pressure of 500 mbar. The range of 2 MeV α-particle, plotted as a function of pressure of the gas mixture (95% He and 5% CF_4) and of percentage of CF_4 in the gas mixture at 500 mbar pressure is shown in Fig. 3.1.

3.2 Production of the ^{56}Ni beam

3.2.1 GANIL facility

Our experiment was conducted in May, 2011 at GANIL in Caen, France. GANIL (*Grand Accélérateur National d'Ions Lourds*) is one of the largest European facilities dedicated for nuclear physics research. Figure 3.2 represents a schematic diagram of the existing GANIL facility.

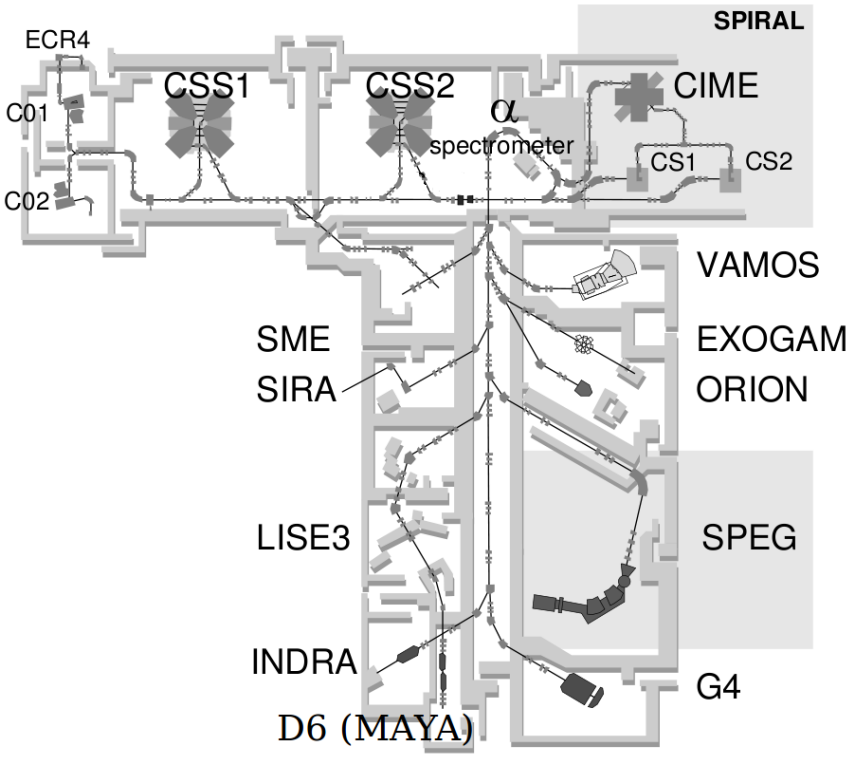

Figure 3.2: Accelerator and experimental halls at GANIL. See description in the text.

Stable beams are produced in the ECR (*Electron Cyclotron Resonance*) ion source. They are then extracted and accelerated in the *Compact Cyclotron* (C01 or C02). The extracted beam is then injected into two identical coupled *Separated-Sector Cyclotrons* (CSS1 and CSS2). The accelerated beam from CSS1 passes through some carbon foils (stripper foils) which strip off more electrons from the beam so that in the second accelerator CSS2 the highly stripped beam can be accelerated to higher energies. Typical average beam energies that can be reached with CSS1 and CSS2 are 13.7 MeV/u and 95 MeV/u, respectively for nuclei with mass number $A \leq 40$.

At GANIL, radioactive beams are produced in two different ways, depending on the energies required. For the intermediate-energy domain, *In-Flight* separation technique with the LISE separator is used, whereas for the low-energies ISOL (*Isotope Separation On Line*) technique (SPIRAL) is used.

- In the ISOL technique, radioactive nuclei are generated by spallation, fission or frag-

mentation reactions of a projectile on a thick target. The products of these reactions are ionized, separated on-line, re-accelerated and sent to different experimental areas after being extracted out of the thick target/source setup.

- In the In-Flight separation method, the radioactive isotopes are produced by projectile fragmentation or fission on a relatively thin target. The reaction products recoil out of the target almost with the same velocity as the primary beam and form secondary radioactive beams. From this cocktail beam, the reaction product of interest can be separated out with the help of magnetic spectrometer and the energy loss in a wedge, placed in the beam trajectory. Furthermore, isotopes of very short half lives ($\sim$ ms or lower) can be produced in this method because of the small transit time from the beam production area to the experimental halls.

3.2.2 Secondary beam production and purification using LISE spectrometer

The primary beam

In our experiment the primary beam was ^{58}Ni. In order to extract the primary beam of ^{58}Ni, a metallic compound of Ni is vaporized to its plasma state. This plasma is then transported to the 14.5 GHz ECR ion source which uses magnetic fields to trap plasma in an evacuated chamber. The positive ions from the plasma are extracted and accelerated in the accelerators (CSS1 and CSS2). In our experiment, ^{58}Ni was accelerated to an energy of 75 MeV/u and transported to the LISE line where it impinged on the primary target ^{9}Be to produce the secondary beam of ^{56}Ni.

The in-flight fragmentation

^{56}Ni was then produced by fragmentation of ^{58}Ni on ^{9}Be. The primary target thickness was chosen in a way to optimize the production rate of ^{56}Ni. But due to the fragmentation mechanism, not only ^{56}Ni was produced but several other isotopes of Fe, Co and Ni were also produced. The cocktail beam (see Fig. 3.5) was purified in the LISE spectrometer in order to extract the almost pure ^{56}Ni secondary beam. We managed to extract up to 97% pure ^{56}Ni. The purification procedure of ^{56}Ni will be discussed in the following and in Chapter 4.

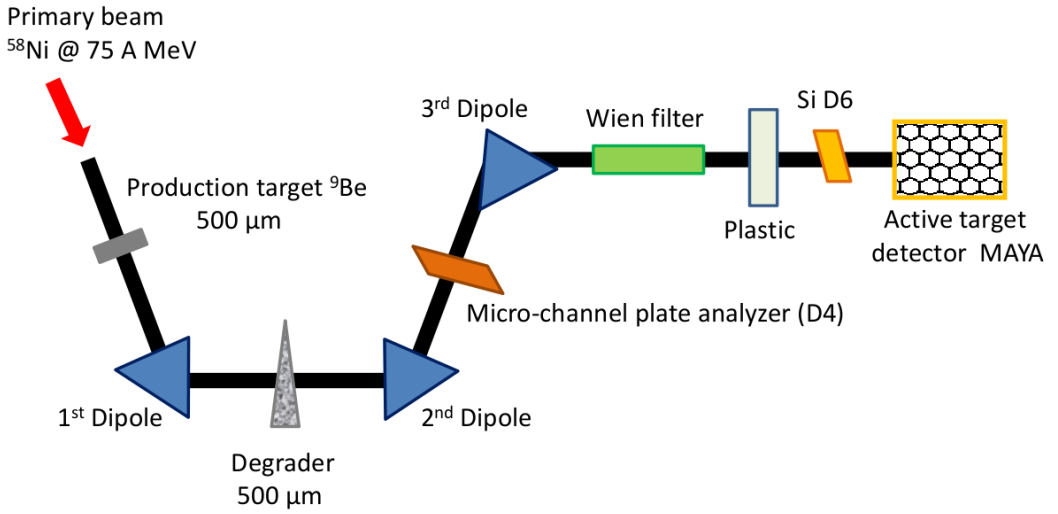

Figure 3.3: Schematic of the LISE magnetic spectrometer and the beam line to the experimental area.

The LISE spectrometer

LISE (*Ligne d'Ions Super Epluchés*) spectrometer at GANIL was designed for the production and selection of radioactive nuclei through in-flight separation technique. LISE spectrometer consists of two dipole magnets which select the fragmented products at 0° angle along with an achromatic degrader placed at the intermediate focal plane of the two dipole magnets [62]. In Fig. 3.3, a schematic setup of the LISE spectrometer is shown.

In case of non-relativistic velocity, when a charged particle passes through a magnetic field B, it deviates from its trajectory due to the magnetic force of magnitude,

$$F = qvB \propto \frac{mv^2}{\rho} \tag{3.1}$$

where q, v and m are the charge state, the velocity and the mass of the particle, respectively, and ρ is the radius of curvature of the particle trajectory.

The magnetic rigidity is,

$$B\rho \propto \frac{mv}{q} \tag{3.2}$$

which indicates that by selecting a given magnetic rigidity $B\rho$, we can select ions with the same mv/q ratio. In relativistic case,

$$B\rho \propto \gamma \frac{mv}{q} \tag{3.3}$$

where $\gamma = \frac{1}{\sqrt{1-\beta^2}}$ is the Lorentz factor and $\beta = \frac{v}{c}$. In order to have further improvement in purifying the secondary beam of interest from the cocktail beam, an achromatic degrader of ^{9}Be was put in the intermediate focal plane of the two dipoles. According to the Bethe-Bloch formula, the ions will undergo an energy loss, δE, through the degrader,

$$\delta E \propto \frac{q^2}{v^2} \tag{3.4}$$

The relative energy loss in the degrader is given by,

$$\frac{\delta E}{E} \propto \frac{m^3}{q^2} \tag{3.5}$$

By selecting proper ratio of $B_1\rho_1/B_2\rho_2$ where $B_1\rho_1$ and $B_2\rho_2$ are the magnetic rigidities of the 1^{st} and 2^{nd} dipole respectively (see Fig. 3.3), and the thickness of the degrader, only ions having the same m^3/q^2 value will be transported. This leads to a better selection of the secondary beam of interest. The third dipole helps in transporting the beam to the experimental areas.

If we assume that the ions of atomic number Z and mass number A are fully stripped of their electrons ($q = Z$), then the selection based on m and q boils down to the selection based on A and Z values of the ions.

Finally, a selection on the velocity of the particles can be done with the help of a Wien filter. In the Wien filter, both the electric field E and the magnetic field B, perpendicular to each other, are perpendicular to the ion trajectory. These fields will generate forces that will force the particle to deviate from its trajectory until the forces are compensated. From Fig. 3.4, it can be seen that only the particles having velocity equal to v_o will be transmitted since,

$$F_E = F_B \Rightarrow qE_o = qv_oB_o \Rightarrow E_o = v_oB_o \tag{3.6}$$

where, E_o and B_o are the properly adjusted electric field and magnetic field to transmit only

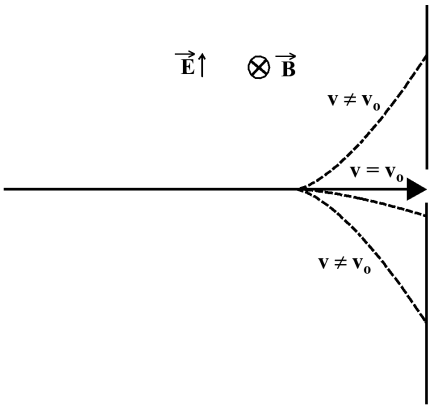

Figure 3.4: Principle of Wien filter.

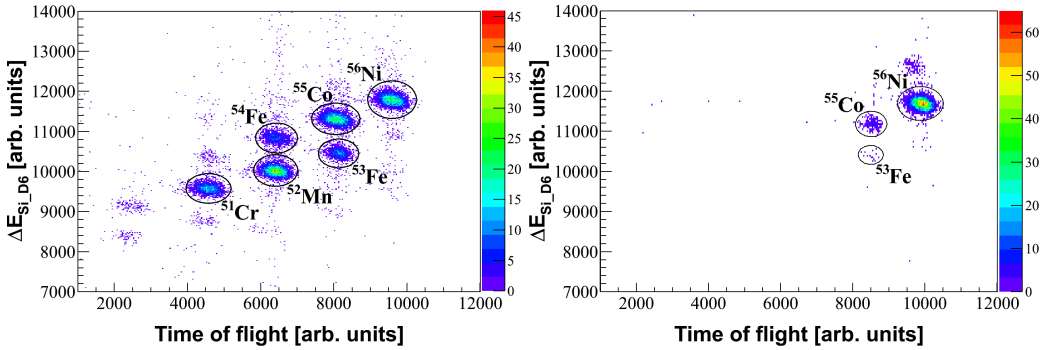

Figure 3.5: Identification matrix showing ^{56}Ni at an early stage of tuning magnetic rigidity and electronics (left panel) and at the end of tuning when almost 97% purity of ^{56}Ni was achieved (right panel).

^{56}Ni beam at 50 MeV/u. Therefore, by adjusting the bias voltage and magnetic field, the velocity of the incoming ions can be controlled. The parameters of the LISE setup are listed in Table. 3.1.

A Si detector of thickness 300 μm was placed in the experimental hall D6 for the identification of the incoming beam particles after the selection process in the LISE spectrometer. A plastic scintillator detector of 50 μm thickness, was also placed in front of the entrance of the MAYA detector for beam monitoring. Incoming particles can be identified by looking into the energy deposited in the Si detector and the time-of-flight of the particles determined by the time difference between timing signals from RF and plastic scintillator. An identification

Primary-beam intensity	$\sim$250 nA
Primary-beam energy	75 MeV/u
Production target	^{9}Be, 525.6 μm
Bρ_1	2.35 T.m
Degrader	^{9}Be, 500 μm
Bρ_2	2.11 T.m
Wien-filter electric field	$\pm$180 kV / 10 cm
Wien-filter current	$\sim$146.4 A
Secondary-beam intensity	$\sim 2\times10^{4}$ pps
Secondary-beam energy	50 MeV/u

Table 3.1: Values of different parameters in the LISE setup; primary and secondary beam intensities during the experiment are also given.

matrix is presented in Fig. 3.5, showing ^{56}Ni.

It has to be noted that the Si detector in D6 can only be used for low-intensity beams. Therefore, it was not used during the data-taking process in our experiment. Selection procedure of ^{56}Ni involving the use of the plastic scintillator during the data analysis will be discussed in Chapter 4.

3.3 Detection systems

3.3.1 The active target detector MAYA

An active target is a detector where the detection takes place at every point of the target, i.e., the target and the detector are the same. An example of such detector is IKAR [63], developed at GSI, which was used to study the elastic scattering of exotic beams at relativistic energies. Another example is MSTPC [64], built in Japan, for studying fusion reactions and nuclear astrophysics at low energies.

Description of the MAYA active target detector

MAYA [65], developed at GANIL, is a TCPC (time-charge-projection chamber) where the gas also serves as the target. MAYA can be used with a variety of gases inside the chamber upto a gas a pressure of 3 atm and thus can be utilized to study direct reactions with a wide variety of light gaseous targets. Different experiments performed with MAYA with

Beam	Energy [MeV/u]	Installations	Reaction	Gas	Pressure [mbar]	Reference
^{8}He	3.9	SPIRAL (GANIL)	^{8}He(p,p)^{8}He	C_4H_{10}	1000	C. E. Demonchy [65]
^{8}He	15.4	SPIRAL (GANIL)	^{8}He(^{12}C,^{13}N)^{7}H	C_4H_{10}	30	M. Caamaño [66]
^{56}Ni	50	SISSI (GANIL)	^{56}Ni(d,d')^{56}Ni*	D_2	1000	C. Monrozeau [53]
^{11}Li	3.6	ISAC2 (TRIUMF)	^{11}Li(p,t)^{9}Li	C_4H_{10}	92-137	I. Tanihata [67]
^{11}Li	5	ISAC2 (TRIUMF)	^{11}Li(p,t)^{9}Li ^{11}Li(p,p)^{11}Li	C_4H_{10}	150 350	T. Roger [68]
^{68}Ni	50	LISE (GANIL)	^{68}Ni(d,d')^{68}Ni* ^{68}Ni(α,α')^{68}Ni*	D_2 He + CF_4	1000 500	M. Vandebrouck [69] [54]
^{56}Ni	50	LISE (GANIL)	^{56}Ni(α,α')^{56}Ni*	He + CF_4	500	Analysis this thesis
^{8}He	15.4	G2 (GANIL)	^{8}He(^{12}C,^{13}N)^{7}H	He + CF_4	175	M. Caamaño and T. Roger [in progress]
^{12}Be	3	REX ISOLDE (CERN)	^{12}Be(p,p')^{12}Be*	C_4H_{10}	160	S. Sambi [in progress]

Table 3.2: Different experiments with MAYA. Different gases were used depending on the purpose of the experiments.

different gas mixtures inside the chamber are listed in the Table 3.2. MAYA is placed inside a stainless steel box. The beam enters into the MAYA volume through a Mylar window of 13 mm diameter and of 6 μm thickness .

In Fig. 3.6, the schematic view of the MAYA detector is shown. MAYA is divided into two main zones:

- An active area where the reaction and the electron drift takes place. The volume of the active drift zone is 28 $\times$ 25 $\times$ 20 cm^3 which is defined by the cathode plate at the top and the Frisch grid at the bottom. The Frisch grid is maintained at the ground potential and the cathode plate at -3000 V. The electric potential increases linearly from the cathode plate to the Frisch grid. The homogeneity of the field is maintained by metallic strips which cover the side and the rear walls of the detector. The wall in the downstream is covered with field

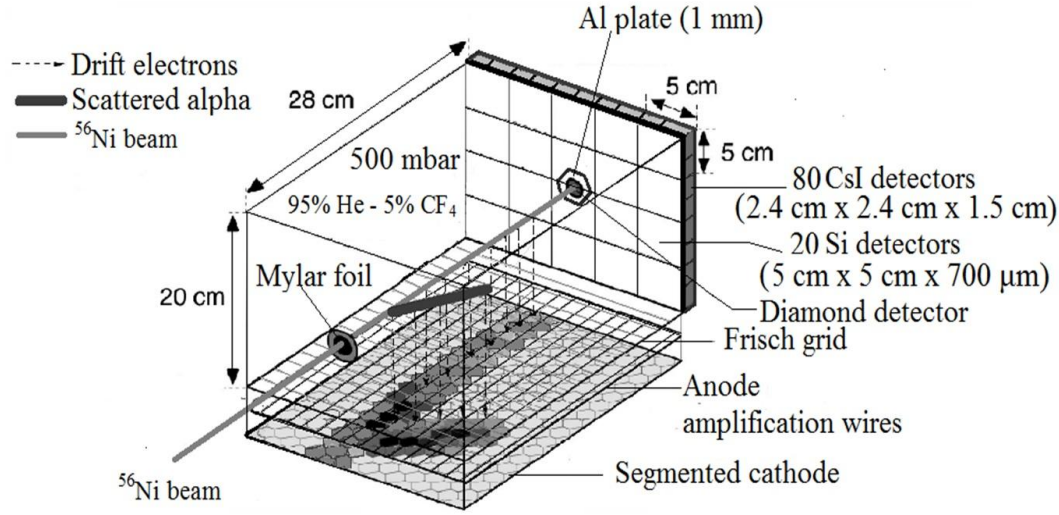

Figure 3.6: The active target MAYA. Shown here is an example of inelastic scattering of ^{56}Ni with ^{4}He.

wires in order to avoid interaction with the forward escaping particles.

The electrons, after being produced by the ionization process, drift downwards towards the Frisch grid because of the applied electric field. The percentage of the gas mixtures along with several other parameters chosen for the experiment are summarized in Table. 3.3.

- The detection zone of MAYA consists of amplification anode wires, located 8.6 mm below the Frisch grid and a segmented cathode plate located 10 mm below the plane of the amplification wires (see Fig. 3.7). The voltage on the amplification wire has to be set in such a way that there is maximum gain while staying below the breakdown voltage. The amplification wires, having a diameter of 10 μm, run parallel to the beam axis. The potential applied between the cathode and the anode, and the distance between the anode and the segmented cathode plate determines the width of the induction pattern on the cathode pad. A part of the segmented cathode pad is shown in Fig. 3.8. The cathode pad is segmented in 32$\times$32 hexagonal pads each of which measures 5 mm per side. The pads are arranged in rows parallel to the amplification wires. In the new generation of active targets, e.g. ACTAR [70], square shaped pads are used.

The segmented-cathode pad plane is connected to a set of GASSIPLEX chips. The signals from the cathode pads are recorded and stored in the GASSIPLEX (*GASSIlicium multiPLEXing chip*) [71] through a *Track and Hold* procedure, triggered by the signals from the amplification wires, until they are sent to the acquisition. These chips are connected in series and

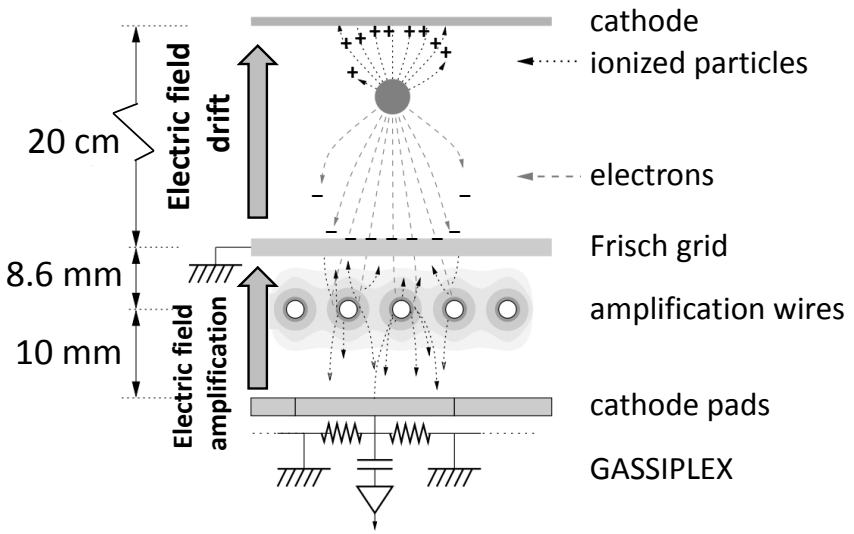

Figure 3.7: Principle of MAYA time-charge-projection chamber. Figure is not to scale.

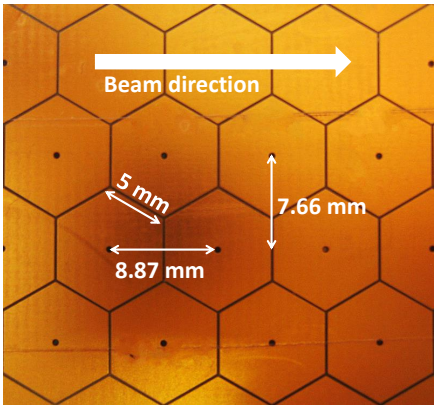

Figure 3.8: Dimensions of the cathode pad.

there is a combination of four chips to form a card. Each card is connected to two rows of cathode pads, resulting in total of 16 cards. Two consecutive cards are serialized resulting in total of 8 outputs from 1024 pads.

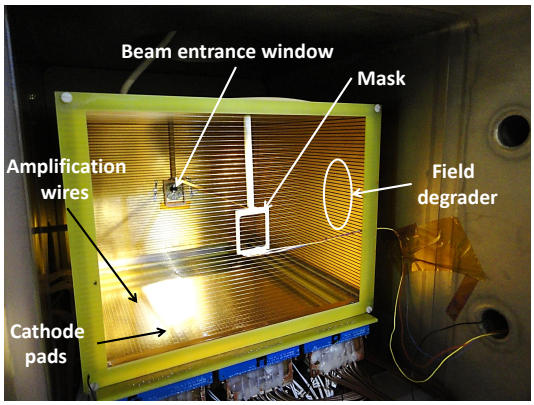

Figure 3.9: Picture of the active target MAYA taken from the back. The beam enters through the Mylar window.

Working principle of MAYA detector

The operating principle of MAYA is similar to a time-projection chamber or gaseous drift chamber with 3-dimensional tracking of particles (see Fig. 3.7). When a particle passes through MAYA it ionizes the gas generating electrons. Because of the applied electric field, the positively charged ions migrate towards the cathode plate, i.e., upper plate of MAYA and the electrons travel towards the Frisch grid which is grounded. The electrons enter the amplification area after passing through the grid, where they are subjected to a much more intense electric field. Therefore, they are accelerated and ionize the gas in the vicinity of the amplification wires causing an avalanche. This induces signals on the cathode pads which are then recorded, amplified and sent to the data-acquisition system by the GASSIPLEX chips. A picture of MAYA is shown in Fig. 3.9.

The charge signal induced on the cathode pad is proportional to the energy of the ionizing particle. When a signal is induced on a cathode pad, its neighboring pads also receive part of the signal. The whole charge projection on the cathode pads gives the range of the ionizing particle and its scattering angle but projected in two dimension. The third dimension can be reconstructed from the timing information of the amplification wires. With this information, the energy of the ionizing recoil α-particle and its laboratory scattering angle can be calculated and from the two-body kinematic calculation, both the scattering angle in the center of mass and excitation energy of ^{56}Ni can be reconstructed. The principle of extracting information from the MAYA detector is detailed in Chapter 4.

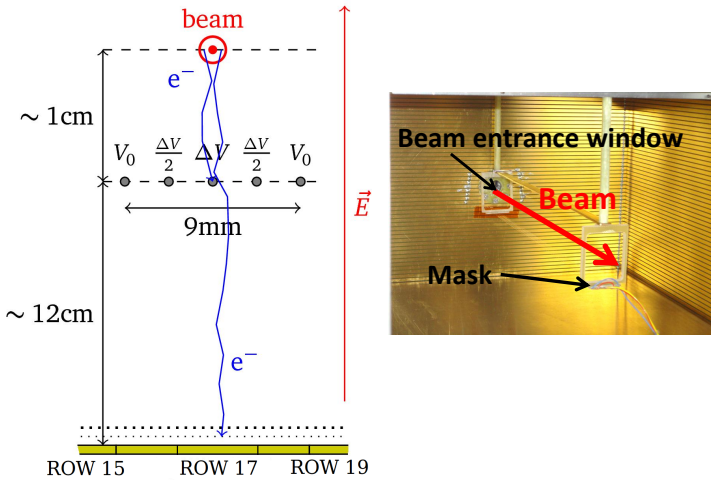

Figure 3.10: Left panel: Schematic representation of the mask. Right panel: Mask in reality along with the beam path above it.

3.3.2 The electrostatic mask

An electrostatic mask [74] has been designed and used in MAYA in order to detect both the heavy- and the light-particle charge projections on the cathode pads without any saturation of the detector and the electronics. The mask was placed 1 cm below the beam axis (see Fig. 3.10). Since the mask is extended throughout the beam width, the transverse width of the mask is from row#15 in the cathode pad to the row#19.

There were three different voltages applied to the mask for the mask to be opaque. The wires at the outer-most position were at the same potential as that generated by the electric field at that height (V_0 in the left panel of Fig. 3.10). The center-most wire was set to more positive potential with respect to V_0 in order to capture electrons to some extent, generated from the beam ionization. If the mask has to be operated in complete transparency, then all the wires are put at the same potential equal to that generated by the drift electric field at the height of the mask.

The simulation result for the electric field in the presence of the mask is shown in Fig. 3.11. There are fewer electrons reaching the amplification wires and the traces generated on the cathode pads have much lower charge than would have been generated by the beam particle without the mask.

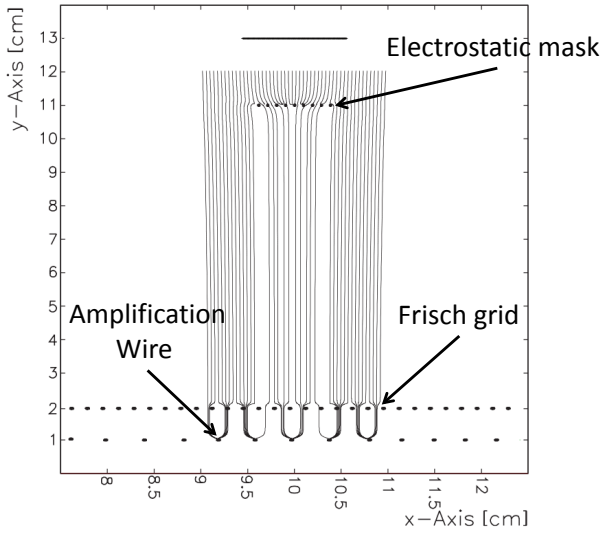

Figure 3.11: Simulated result for the electron drift in the presence of the partially transparent mask without consideration of the diffusion of the electrons in the gas [74].

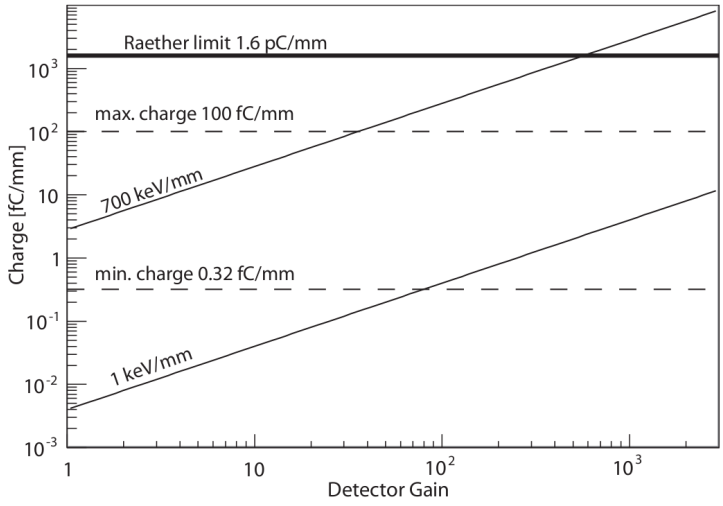

Figure 3.12: Total charge deposition per mm as a function of the gain of the detector for a heavy particle (having energy loss 700 keV/mm) and for a light particle (having energy loss 1 keV/mm) [74].

As previously stated, the primary goal of using the electrostatic mask is to solve the problem

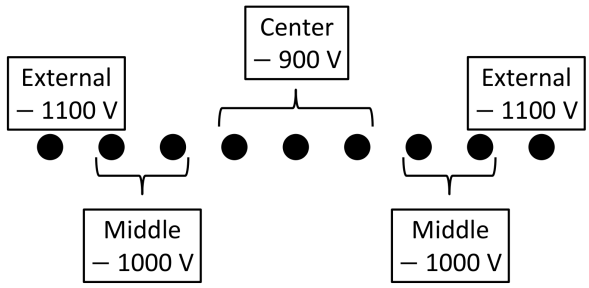

Figure 3.13: Potential applied to different wires of the electrostatic mask.

Target	He
Reaction	^{56}Ni(α,α')^{56}Ni*
Gas mixture	95% He + 5% CF_4
Pressure	500 mbar
Cathode voltage	-3000 V
Anode wire voltage	+1300 V
Mask voltage	$\begin{cases} V_{External} = -1100 \text{ V} \\ V_{Middle} = -1000 \text{ V} \\ V_{Centre} = -900 \text{ V} \end{cases}$

Table 3.3: Operating parameters for the MAYA chamber during the experiment.

of the dynamic range of the charge deposition on the cathode pads. The dynamic range is defined as the difference of the smallest and the largest detectable charges on the cathode pads. Figure 3.12 illustrates this issue, where the charge deposited by an ionizing particle is shown as function of the detector gain. If we consider a heavy particle having an energy loss of 700 keV/mm and a light particle having an energy loss of 1 keV/mm then there is no possible gain adjustment of the detector to detect both particles simultaneously in the acceptance range of the electronics. Hence, by using a mask the amount of electrons reaching the amplification wires after being generated by the ionizing heavy particle can be reduced. Therefore, the charge deposited on the cathode pads (per mm) is lower and we can detect both the heavy- and the light-particle traces on the pads without any saturation of the electronics (GASSIPLEX).

In our experiment a potential of -1100 V was applied to the outermost wires, -1000 V to the middle wires and -900 V to the central wire (see Fig. 3.13).

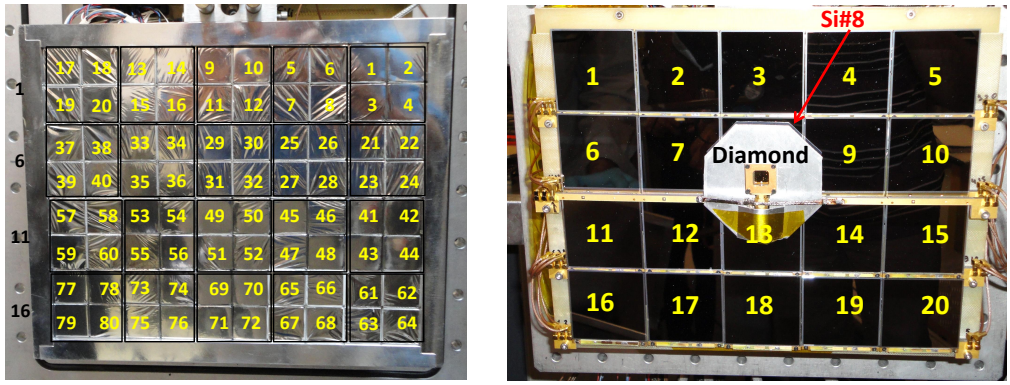

Figure 3.14: Left panel: CsI detectors mapping. Behind every Si detector there are four CsI detectors. Black squares on the CsI detectors depict the Si detectors. Right panel: Si detectors mapping. Si#8 is shown in red. Diamond detector is also shown.

3.3.3 The ancillary detectors

Si and CsI detectors

^{56}Ni is a neutron-deficient nucleus. Due to inelastic scattering with helium, ^{56}Ni is excited above the particle emission threshold, from where it can decay mainly by emitting protons or α-particles. Since these decay particles have almost the same energy per nucleon as the beam, they will not stop inside the MAYA volume. To detect these decay particles we have placed ancillary detectors in the forward direction.

In total we have 20 Si (5×5 cm^2) detectors each having a thickness of 700 μm placed at a distance of 50 mm from the MAYA active volume. In order to protect it from light (spark), it was covered with an aluminized-Mylar foil. Behind every Si detector there is a group of 4 CsI detectors. In total we have used 80 CsI detectors each having a thickness of 1.5 cm. The mapping of the Si and CsI detectors is shown in Fig. 3.14.

These Si and CsI detectors allow particle identification using the ΔE-E method. A coincidence study can be made by gating on the particle in the ΔE-E plot and looking back into the charge projection on the cathode pads produced by the recoil particle.

Diamond detector

The diamond detector what we used in our experiment is a poly-crystalline diamond of 1 cm^2 surface area and a thickness of 100 μm. The diamond detector (see Fig. 3.14) is resistant to damage by the incident radiation and it has a very good temporal resolution (a few tens of ps) which makes it a good counter for the number of incident particles. It also acts as a beam dump. Since ^{56}Ni beam is produced by the fragmentation process, the emittance is larger than that of stable beams. The surface of the diamond detector is not large enough to cover all the incident beam particles and many of them are also detected in Si#8 situated just behind the diamond detector. An aluminum plate was also placed behind the diamond detector. The diamond detector was not functioning during our experiment and, therefore, was not producing any information. It was only used as beam dump.

3.3.4 Electronics

A full schematic drawing of the electronics for the MAYA setup and the ancillary detectors is shown in Fig. 3.19.

The data-acquisition system is governed by the GMT (*Ganil Master Trigger*) module. When it receives a trigger signal it generates a FTA (*Fast Trigger Analysis*) which starts the data-readout process within the DT (*Dead Time*) also determined by the GMT.

Electronics for the amplification wires and the cathode pad

Two observables are measured with the amplification wires: the charge collected on the wires and the timing information. The pre-amplified (PA) signal from each wire is then split into two signals:

- One is a *slow* signal which is first treated in the SA (*Spectroscopic Amplifier*) and then sent to the ADC (*Analogue to Digital Converter*) module for data acquisition. This signal is a measure of the amount of charge collected on each wire.

- The other signal, called *fast* signal, provides the timing information. This signal is amplified in the FA (*Fast Amplifier*) and then sent to a LTD (*Low-Threshold Discriminator*). The output signals from LTD are then divided into two parts. For the first part, signals for all 32 wires are OR-ed and used for triggering the GMT for data acquisition. A down-scaled (10^{-4}) version of the OR-ed wire signal was also selected as the triggering signal.

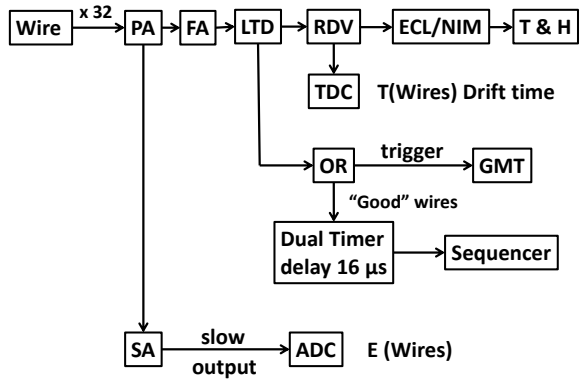

Figure 3.15: Electronics scheme for the anode wires.

In the second part, the output signals from the LTD are fed to a RDV (*Retarde Durée Variable*). Signals from RDV are again split into two different parts.

One part is fed to the TDC (*Time to Digital Converted*) to track down the timing information for the amplification wires. The start of the time measurement is the FTA signal fired by the Si trigger. It is to be noted that this is not the case when Si detectors do not fire. In that case the amplification wire which receives electrons first acts as start of the TDC and the wire receives electrons at the end used as the stop of the TDC.

The other part of the signal from RDV is used for the triggering of the readout process of the charge collected on the cathode pads. When a wire is fired, it creates a *Track and Hold* (T & H) signal which is sent to the corresponding row of the cathode pads to read the charges on the pads. But then another *Track and Hold* signal is sent to the next row in the direction of the ionizing-particle trajectory to read the charges of the pads in that row. This process ensures that the charges of all the pads in the particle trajectory are read so that the Bragg peak of the particle ionization can be easily reconstructed. A schematic drawing of the electronics for the anode wires is shown in Fig. 3.15.

In case of wire trigger, from the OR-ed output of 32 LTD signals for 32 wires, the *good wires* signals (the wires outside the beam region, i.e., wires#10, 11, 12, 13 for the left side of the beam and wires#22, 23, 24, 25 for the right side of the beam, see Fig. 4.1) are chosen. These wires are termed as *good wires* because for both long and short recoil-particle tracks (for definitions of long and short tracks see Chapter 4) these *good wires* are triggered. The *good wires*' signals are then OR-ed and this OR-ed signal is delayed using a *Dual Timer* for about

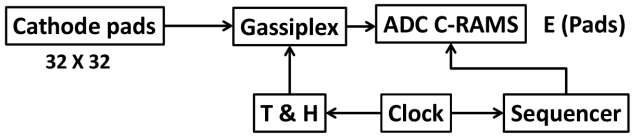

Figure 3.16: Electronics scheme for the cathode pads.

16 μs[1] until all the electrons from the entire ionization path of the ionizing particle have drifted down towards the amplification wires. After that the GASSIPLEX chips record the amplitude of the charge induced in each cathode pad when a *Track* signal arrives. Each GASSIPLEX chip performs amplification, shaping and multiplexing of the signals from 16 cathode pads. The GASSIPLEX holds it in memory for the *Hold* time and returns it in the multiplexed form when requested by the sequencer. The signals are then sampled in C-RAMS (*Caen Readout for Analog Multiplexed Signals*) based on the clock signal provided by the sequencer. Each rising front of the clock gets modified based on the amplitude of the recorded signal from each pad. This signal is then sent to an ADC for reading. After a proper alignment in which the pads are gain matched, it is possible to apply a general threshold to read only the pads with non-zero signal (pedestal subtraction), thus reducing the data-acquisition dead time. An *Inhibit* signal prevents the interference of any other trigger signal during the readout process. A schematic drawing of the electronics for the cathode pads is shown in Fig. 3.16.

Electronics for the ancillary detectors

Si detector

Regarding the Si detector, the signal from the pre-amplifier is fed into the SA. The SA produces two signals: *slow* and *fast*.

- The *slow* signal is proportional to the energy of the particle which stops in the Si detector or to the energy deposited in case of punching through the Si detector. This signal is sent to the ADC for recording.

The normal *slow* output from the SA is also amplified 10 times in order to increase the dynamic range keeping a reasonably good resolution for detection of light particles (proton,

[1] 16 μs corresponds to the maximum drift-time of the electrons.

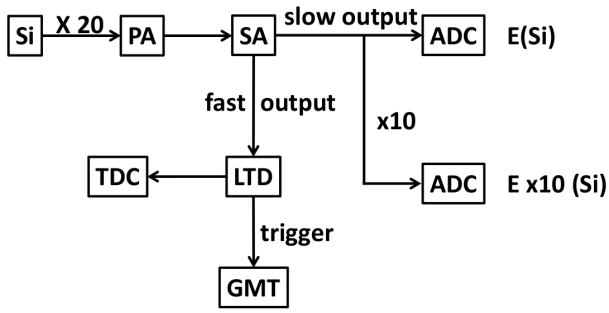

Figure 3.17: Electronics scheme for the Si detectors.

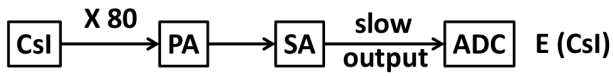

Figure 3.18: Electronics scheme for the CsI detectors.

deuteron, triton).

- The *fast* output from the SA is sent to a LTD (*Low-Threshold Discriminator*). The generated fast signals from the different Si detectors are OR-ed. This OR-ed Si signal triggers the GMT and acts as a start of the data acquisition. In this OR-ed Si signal, signals from all the Si detectors are OR-ed except Si#8. Si#8 is situated behind the diamond detector (see Fig. 3.14) which is facing the incoming beam particles. The signal from Si#8 is scaled down by a factor of 100 and afterwards put into the GMT. When a Si triggers, the signal is delayed until the anode wires are also triggered by the electrons from the ionizing particles drifting towards them. A schematic drawing of electronics for the Si detectors is shown in Fig. 3.17.

CsI detector

The signals from the CsI detectors were not used for triggering. The signals from the CsI detectors were simply fed into the SA and the *slow* output signals were sent to the ADC for recording. Together with the Si detectors, the CsI detectors serve the purpose of particle identification via the ΔE-E method. A schematic drawing of electronics for the CsI detectors is shown in Fig. 3.18.

Diamond detector

During our experiment the diamond detector was not functioning. Hence, we could not monitor the incoming beam particles with it. It was simply used as the beam dump.

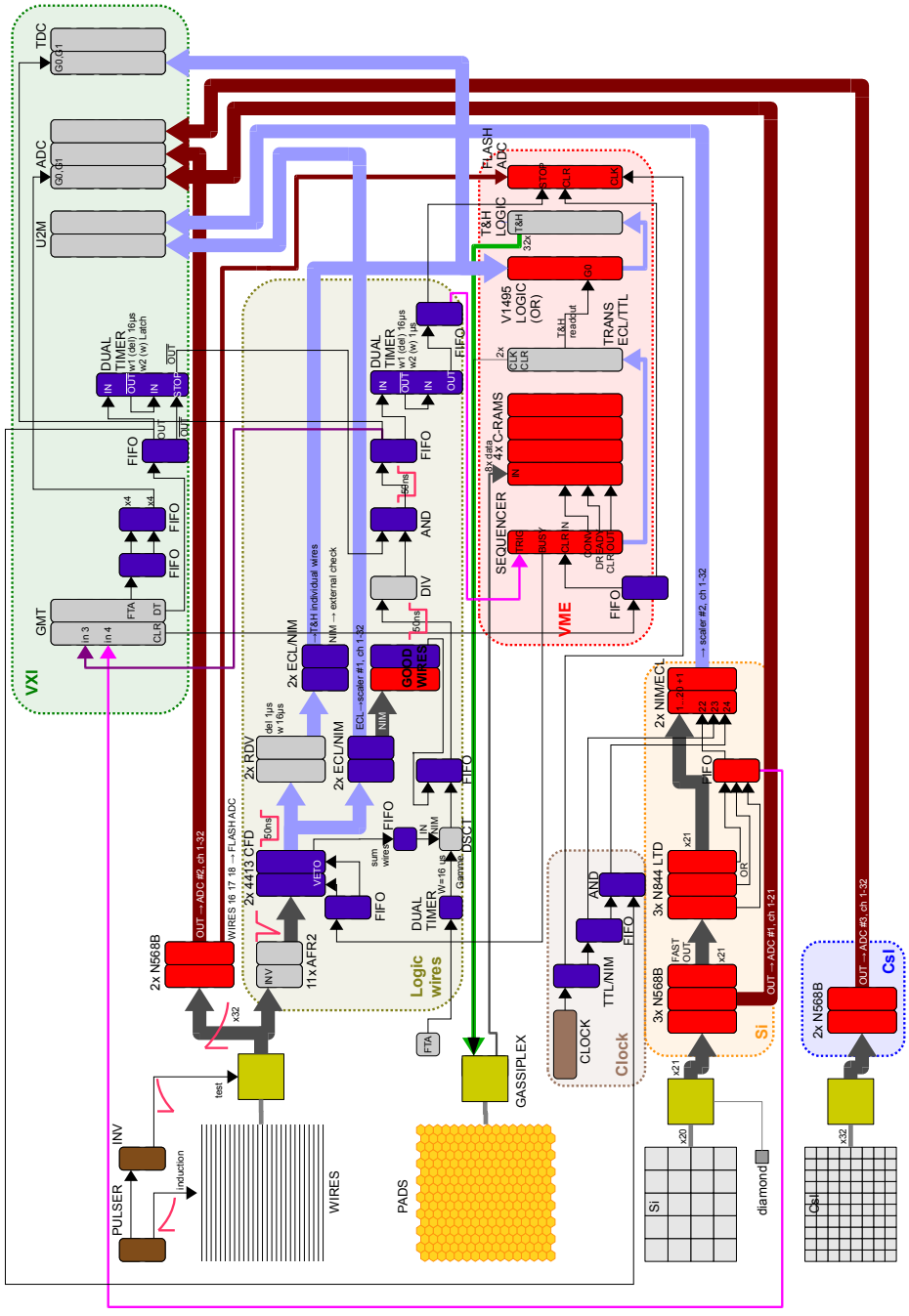

Figure 3.19: Electronics scheme of MAYA and ancillary detectors.

Chapter 4

Data Analysis

The main objective of this chapter is to describe how the kinematics observables, i.e., energy and scattering angle of the recoil particles are reconstructed. Before extracting the information from the raw data, calibration of different components of the detector setup is needed. This chapter begins with the conventions used during data taking and data analysis followed by the details of the calibration procedures. Methods for track reconstruction inside MAYA, drift-time measurement and identification of the incoming ^{56}Ni beam and the recoil α-particle will be discussed.

4.1 The conventions

An event is composed of the following raw data:

- charges induced on the cathode pads in MAYA,
- charges deposited on the anode wires (the charges deposited on the wires have not been used for track reconstruction or particle identification),
- timing information from the amplification wires,
- charges in the Si detectors,
- charges in the CsI detectors.

In addition, the plastic scintillator before MAYA (see Fig. 3.3) gives information about the number of incoming beam particles.

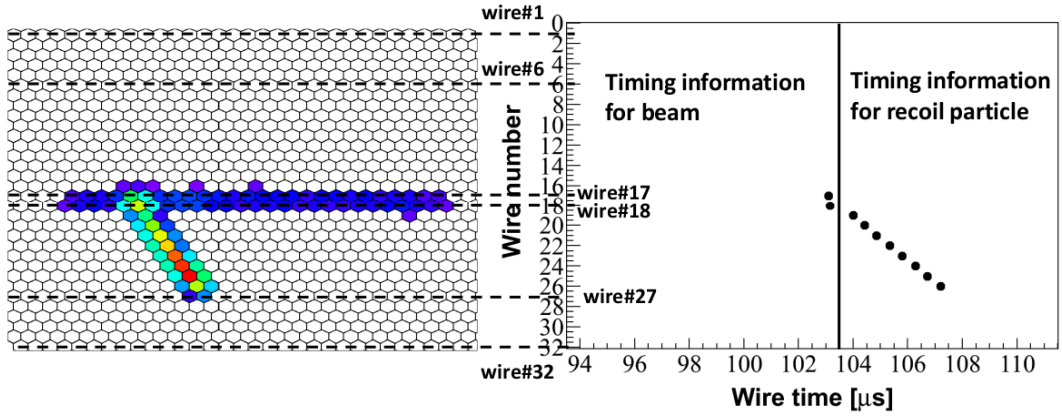

Figure 4.1: An event with the charge projection from the beam and the recoil-particle ionization (left panel) and the timing information from the corresponding amplification wires (right panel).

Convention for the anode wires and the cathode pads

In Fig. 4.1, a typical event with two-dimensional charge projection of the beam and recoil particle is shown. The third dimension is obtained from the timing information of the anode wires. Reconstruction of the drift-time will be discussed in Section 4.3.2.

Figure 4.2 shows the conventions used throughout the analysis procedure concerning the cathode pads. The segmented cathode plane in MAYA is divided in two areas by the beam: left side with respect to beam direction includes the rows of pads below wire#17 and right side includes rows above wire#17. Each pad is labeled with indexes (i, j) with i being the column number and j the row number. The corresponding charge on the pad (i, j) is denoted as q_{ij}. The origin $(0, 0)$ is selected at the top left corner of the pad with the positive y-axis pointing downwards, opposite to the Cartesian co-ordinates.

Since ^{56}Ni is an exotic nucleus and it is produced by *In-Flight* fragmentation (see Section 3.2.1), the beam is not a pencil beam; it has an emittance. Although the ^{56}Ni beam is parallel to row#17 but it spreads over three-four rows from row#15 to row#19.

The anode wires run parallel to the rows of the cathode pad plane. Wires#16,17,18 will see electrons drifting downward mainly from the beam ionization path. From Fig. 4.1, it can be seen that the wires#19-27 will see electrons drifting downward from the ionization path due to the passage of the recoil particle.

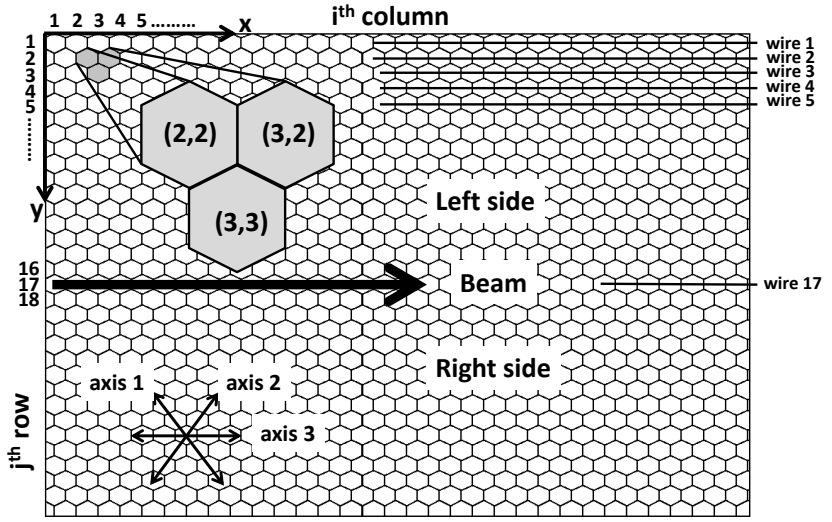

Figure 4.2: Convention used for the cathode pad in MAYA.

For the recoil particles that stop[1] inside MAYA, the range of the particles and therefore their energies can be extracted. From the charge projection of the recoil particle, the Bragg peak can be identified. The position of this peak provides information about the range of the recoil particle but projected in "two dimensions" (R_{2d}). The angle between the projected beam and recoil particle trajectory is the two-dimensional scattering angle (θ_{2d}). From the timing information of the anode wires, both R_{2d} and θ_{2d} can be corrected for the third dimension. Details of extraction method of range and scattering angle for the recoil particle will be discussed in Section 4.3.

The relationships between the actual range (R) and the scattering angle (θ) and their two-dimensional projections on the cathode pad plane which eventually give R_{2d} and θ_{2d} along with the ϕ angle obtained from the timing information from the wires are shown in Fig. 4.3. The co-ordinate axes are also shown.

[1]Recoil particles that punch through MAYA volume are discarded in the present analysis.

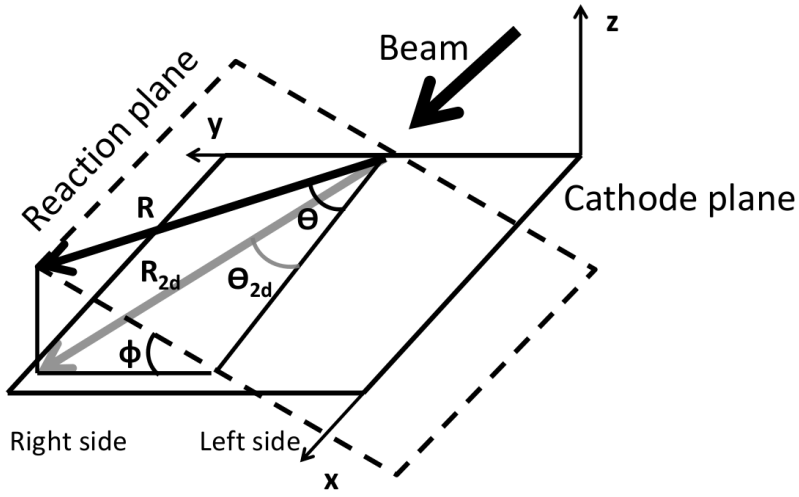

Figure 4.3: Relations between projected range (R_{2d}) and scattering angle (θ_{2d}) and actual range (R) and scattering angle (θ) are shown. The ϕ angle is the angle of the reaction plane with respect to the plane parallel to the cathode pad plate.

4.2 Calibrations

4.2.1 Calibration of the cathode pads

In order to ensure that all 1024 pads (32×32) have identical response to the same signal, i.e., they are gain matched, a proper gain matching of the pads is needed which is in turn useful for placing a common threshold for all pads. To proceed with the pad gain matching, we used a pulse generator. A signal was sent to the 32 amplification wires to mimic a real event in which wires are fired by the electrons drifting towards them and charges are induced on the pads. This process was repeated for five pulse signals of different amplitudes not separated equally from each other (see Fig. 4.4) to test the non-linearity especially in the lower channels of ADC, since we expect signals from low-energy recoil particles. A linear fit is performed to correct for the response of each pad.

In Figs. 4.4 (a) and (b), charges seen by the pads have been plotted against the corresponding pad numbers. The first two rows of the cathode pads are unusable as they were not functioning during our experiment. Also few pads in row#7 were not functioning. Furthermore, there are also side effects which make the pads closer to the edges of the cathode pad plate unusable, too. To overcome these problems, simulations have been done accordingly

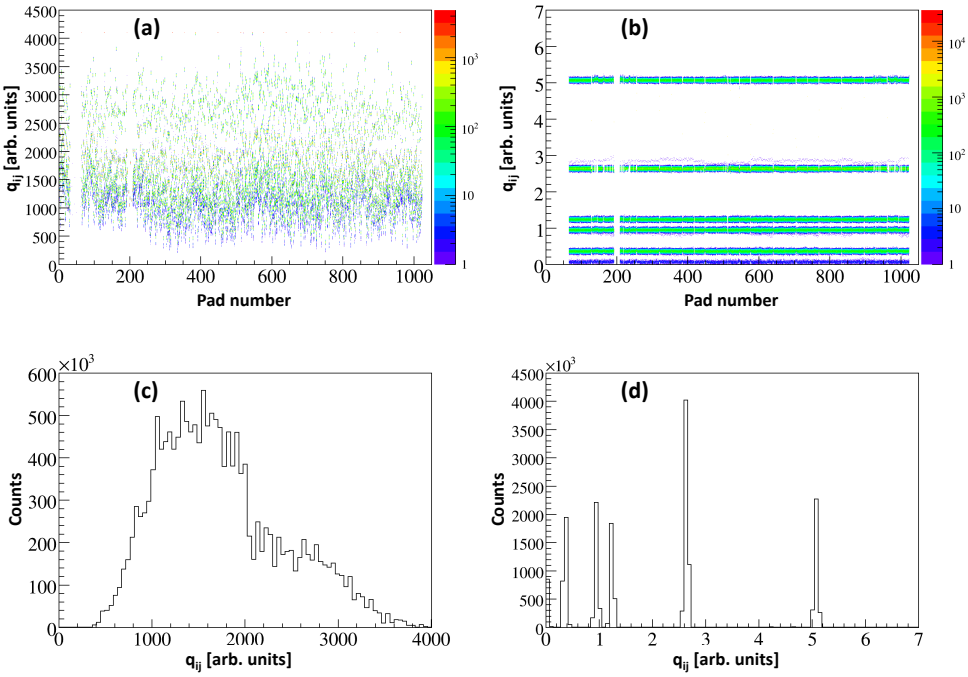

Figure 4.4: Cathode Pad calibration: Responses from all cathode pads are plotted against pad numbers a) before gain matching and b) after gain matching. Responses from all cathode pads are shown c) before gain matching and d) after gain matching.

in order to take care of this effect for the efficiency correction (see Chapter 5).

In Figs. 4.4 (c) and (d), the charges on the pads are shown before and after gain matching. They are obtained by projecting the charges on the y-axis in Figs. 4.4 (a) and (b), respectively. The peak at position 0 after gain matching shows the pedestal. It should be noted here that this is a relative gain matching and there is no equivalence at this point between the charges induced on the pads and the energy of the ionizing particle.

Typical relative charge-resolution of a single pad is 2.3%. Although the charges on the pads are proportional to the energy of the ionizing particle, energy of the particle is not deduced from the charges on the pads because of the poor charge-resolution but rather from the range, obtained by projecting the pad-charges. A comparison of energy-resolution of the ionizing particle obtained from the pad-charges and from the range, is given in Chapter 5.

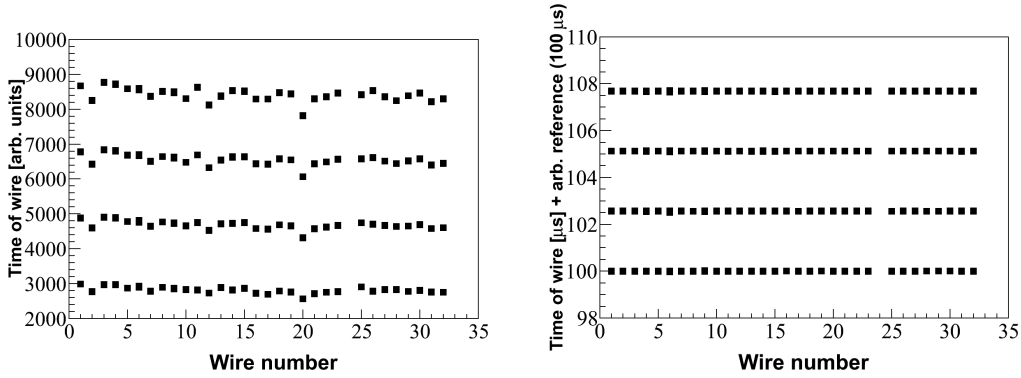

Figure 4.5: Time responses of 32 amplification wires for a pulse signal of period 2.56 μs generated by a Time-Calibrator module before calibration (left panel) and after calibration (right panel).

4.2.2 Time Calibration of the amplification wires

To obtain the same timing response of the amplification wires, a time calibration of the wires is necessary. A Time-Calibrator module, which generates pulses with a period of 2.56 μs within a range of 10.24 μs, was used for this purpose. In order to get the channel to time equivalence, a linear fit for the response of each wire is performed. Figure 4.5 shows the results of time calibration. Wire#24 was not functioning during the experiment. Typical time resolution of an anode wire is 3.5 ns (FWHM).

For an ADC, when no event is recorded, a value is produced which corresponds to the pedestal (or 0 if calibrated). But in case of TDC an event can occur at time $t = 0$ and in TDC it belongs to channel zero. In order to avoid such confusions in defining "no-event" condition and since only the relative timing information is relevant in the analysis for this experimental setup (see Section 4.3.2), a non-zero time-offset (in this case 100 μs) is applied to each wire so that $t = 0$ also means that there is no event.

4.2.3 Calibration of the ancillary detectors

Si detectors

For calibration of the Si detectors (see right panel of Fig. 3.14), a 4α-line source was used. The source is ^{226}Ra, which emits α-particles of energies 4.78 MeV, 5.49 MeV, 6.0 MeV and 7.69 MeV (the smaller peaks in Fig. 4.6 (d) are also due to the decay α-particles in the decay

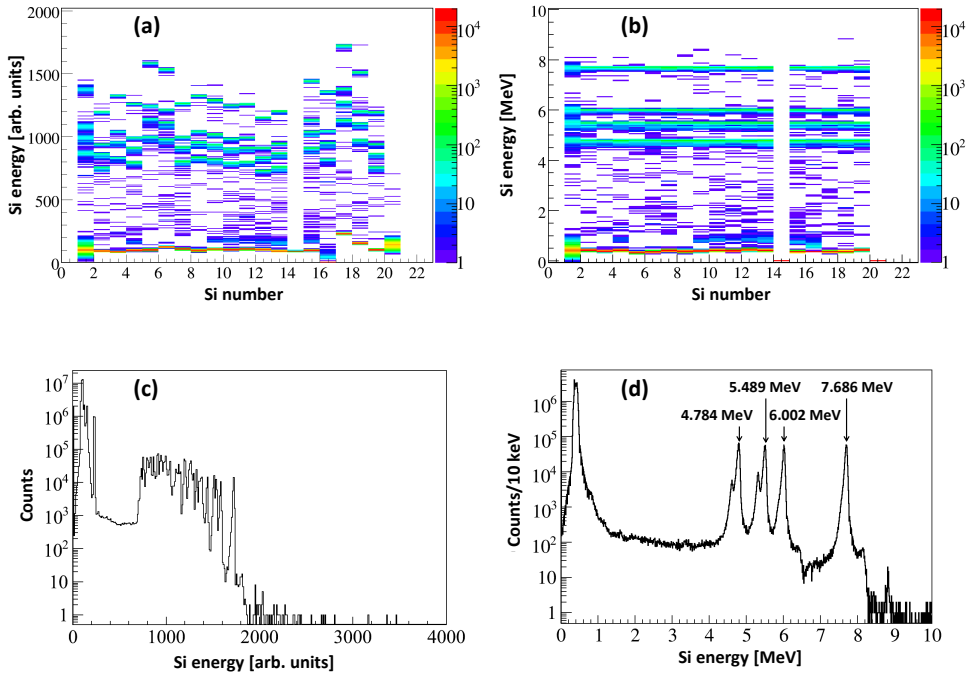

Figure 4.6: Si normal output calibration (see text for details).

chain, see Appendix A) through its daughter nuclei (^{222}Rn, ^{218}Po and ^{214}Po) [72]. Each energy peak is fitted with a Gaussian and a linear fit is performed for the peak positions to get the channel to energy correspondence. In Fig. 4.6 (a) and (b), the energy deposited in the Si detectors is plotted versus the Si-detector number to show the goodness of Si-detector calibration. It is clear from the figure that Si-detector#14 is not functioning and Si-detector#1 (hereafter refereed to as Si#) is noisy as compared to the other Si detectors. The total response of all Si detectors before and after the calibration is shown in Fig. 4.6 (c) and (d), respectively.

The energy resolution of one Si detector is typically 60 keV (FWHM) for the 7.69 MeV peak. The total energy resolution of all Si detectors for the same 7.69 MeV peak is 65 keV (FWHM) which means that the error introduced from the effect of imperfect gain matching is 25 keV (FWHM).

Since the normal outputs from the Si detectors are amplified 10 times (10×) to increase the ADC dynamic range for detection of light particles, calibration has also been done for 10×

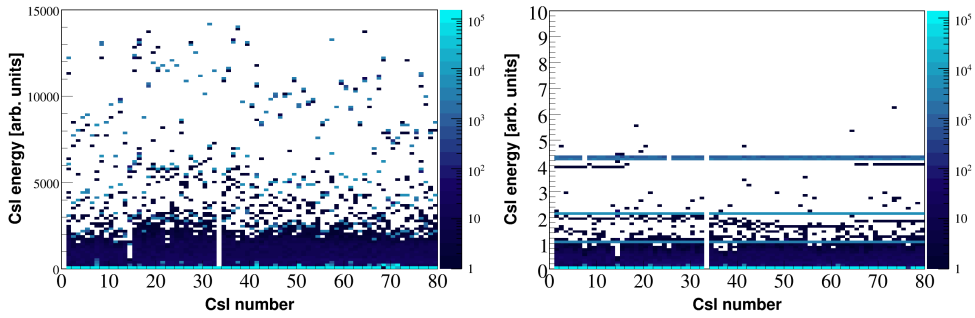

Figure 4.7: Responses of CsI detectors before (left panel) and after (right panel) pulser gain matching.

output of the Si detectors using the same 4α line-source for the dynamic range of 0 to 8 MeV. Energy resolution of 10$\times$ output of Si detector is also $\sim$60 keV (FWHM) for the 7.69 MeV peak.

CsI detectors

Calibration of the CsI detectors (see left panel of Fig. 3.14) is not straight-forward because of the non-linear response and of the particle-dependence light emission for the same energy loss in the CsI detector [73]. A three-step calibration procedure for the CsI detectors has been performed:

- Pulser signals of three different amplitudes were sent to the CsI detectors. To gain-match 80 individual CsI detectors, the responses from those detectors were fitted linearly:

$$V_{pulser} = a_{pulser} * channel + b_{pulser} \tag{4.1}$$

where V_{pulser} is the pulser amplitude. The slope and the offset of the linear fit are a_{pulser} and b_{pulser}, respectively.

Figure 4.7 shows results before and after the pulser signal gain matching. CsI#33 was not functioning during experiment. Due to high gain in CsI#7 & 25, the last pulser peak was out of the range.

- The absolute response of each CsI detector was checked with the same 4α-line source used for Si detectors calibration. The α-peak of energy 7.69 MeV is well separated from the other three peaks (see Fig. 4.8). For each CsI detector, the position of the 7.69 MeV α-

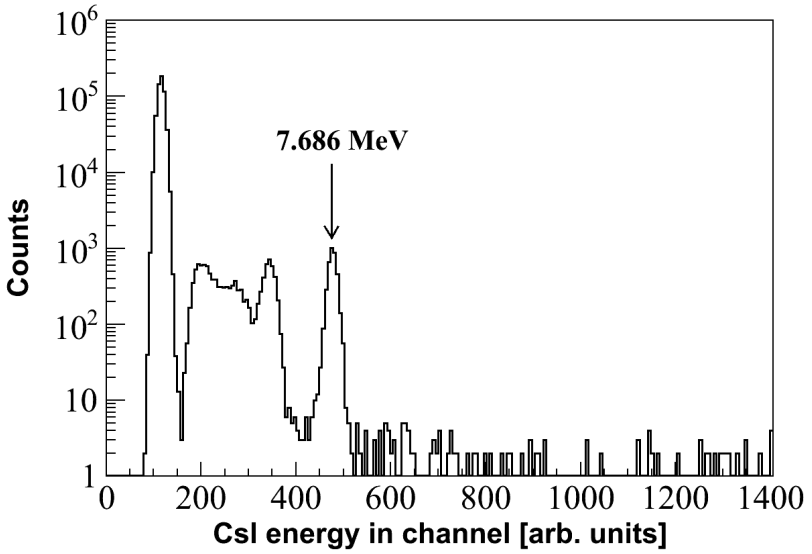

Figure 4.8: 4α-source run for CsI detectors.

peak was determined in terms of channel number (x_α). Typical relative resolution of a CsI detector for the 7.69 MeV α-peak is roughly 4%.

The peak position (in channel) was converted into the equivalent pulser gain (V_α) for each CsI detector:

$$V_\alpha = a_{pulser} * x_\alpha + b_{pulser} \tag{4.2}$$

A correspondence factor γ between the pulser voltage V_α and energy is obtained per detector from the following relation:

$$\gamma = \frac{7.69}{V_\alpha} \tag{4.3}$$

So the calibration parameters for each CsI detector are $\gamma * a_{pulser}$ and $\gamma * b_{pulser}$, which serve as the slope and the offset of a polynomial of order 1, respectively.

- Due to inelastic scattering with helium inside MAYA, ^{56}Ni can be excited above the particle-emission threshold. It then can decay by emitting neutrons, protons and alpha par-

(1)17	18	(2)13	14	(3)9	10	(4)5	6	(5)1	2
19	20	15	16	11	12	7	8	3	4
(6)37	38	(7)33	34	(8)29	30	(9)25	26	(10)21	22
39	40	35	36	31	32	27	28	23	24
(11)57	58	(12)53	54	(13)49	50	(14)45	46	(15)41	42
59	60	55	56	51	52	47	48	43	44
(16)77	78	(17)73	74	(18)69	70	(19)65	66	(20)61	62
79	80	75	76	71	72	67	68	63	64

Figure 4.9: Si-CsI mapping with Si-detector numbers in parenthesis. Each Si detector is backed by four CsI detectors. Different colors represent the different pre-amplifiers connected to the CsI detectors.

ticles. These decay particles, having high energy (almost same energy per nucleon as the beam), will not stop inside the MAYA volume. They are forward focused and can be detected in the forward Si-CsI telescope.

Figure 4.9 shows the mapping of the Si detectors (in parenthesis) and CsI detectors. The CsI detectors are behind of Si detectors. Combination of Si#9 and CsI#25 was chosen as the reference because this combination is located at the central region of Si-CsI mapping and Si#8 is facing the beam. A real beam-time run (run#70) was chosen to obtain ΔE-E plots for Si-CsI detectors.

The loci of the energy loss in Si#9 (ΔE) versus the energy deposited in CsI#25 (E) are shown in Fig. 4.10 with red dots. The ΔE-E spectrum for Si#12 and CsI#56 is shown with black dots. Since the α-particle identification loci for the two different combinations were not gain-matched, effort has been put to change the correspondence factor γ manually per CsI detector so that the ΔE-E plots for α-particle identification for both Si-CsI combinations fall on top of each other. This procedure has been repeated for all possible combinations of Si-CsI detectors taking Si#9 and CsI#25 as the reference.

In the above procedure of calibrating the CsI detectors with respect to the ΔE-E identification plot for α-particle it has been found that identification loci for particles other than α-particle (p,d,t....) are also aligned. In Fig. 4.11, the ΔE-E identification is shown for all possible Si-CsI combinations with and without the light-output correction for the CsI detectors [73]. The solid lines in the right side of Fig. 4.11 represent the calculated energy losses in Si and CsI detectors. It shows the goodness of Si and CsI detectors gain-matching.

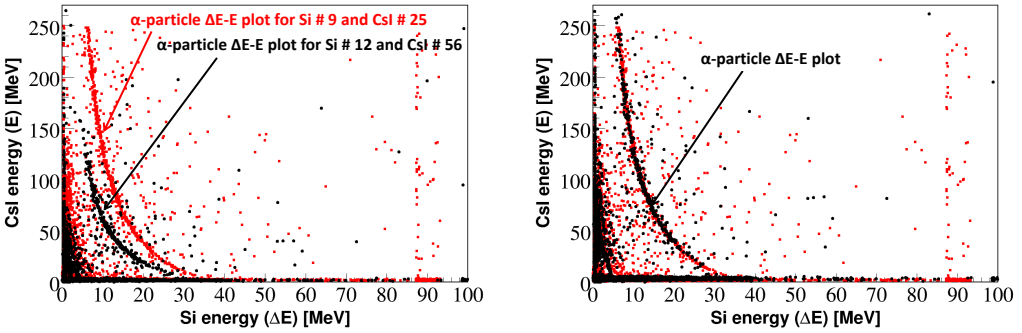

Figure 4.10: Δ*E*-*E* spectrum for Si-CsI detectors before calibration of CsI detectors (left panel) and after calibration of CsI detectors (right panel). The red dots represent the Δ*E*-*E* spectrum for Si#9 and CsI#25 combination (reference combination) whereas the black dots represent the Δ*E*-*E* spectrum for Si#12 and CsI#56 combination.

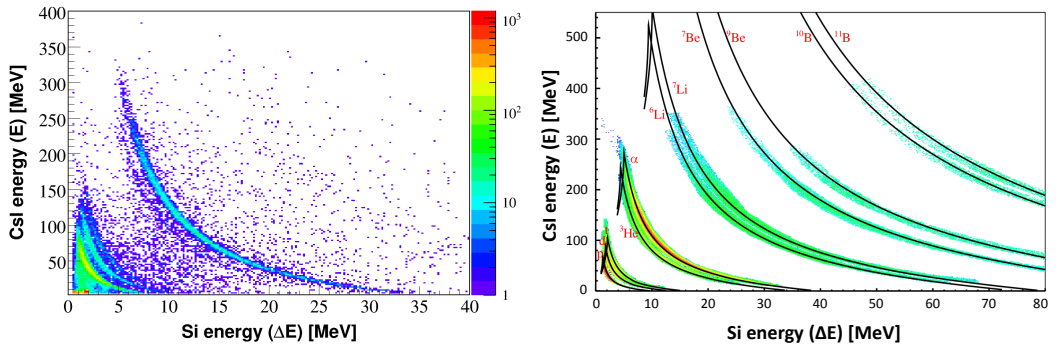

Figure 4.11: Δ*E*-*E* spectrum for all possible combinations of Si-CsI detectors without (left panel) and with (right panel) the light-output correction. In the Δ*E*-*E* spectrum without light-output correction (left panel) only one beam-time run has been considered whereas in the Δ*E*-*E* spectrum with light-output correction (right panel) all the beam-time runs are taken into account. For the plot in the right panel cuts have been made around the particle-identification loci.

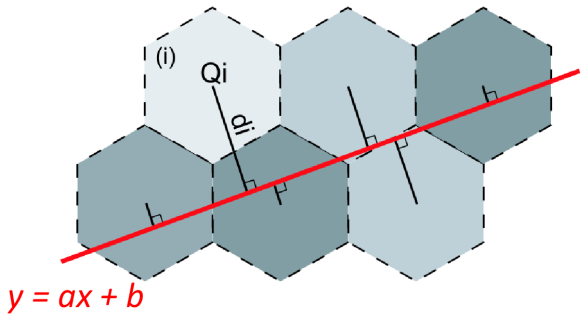

Figure 4.12: Global fitting method for track reconstruction [75].

4.3 Reconstruction of scattering angle and energy of the recoil particle

4.3.1 Trajectory reconstruction

To extract the direction of trajectories from the induced charge pattern on the cathode pads, the "so-called" *global fitting method* [75] is used. The basic principle of this method is based on a fit of the whole charge distribution of the ionizing particle by means of orthogonal-distance-regression method. This method aims at minimizing the perpendicular distances of the cathode pads weighted by the corresponding charges on the pads from the fitted trajectory line (see Fig. 4.12). Fitting the trajectory leads to finding the proper trajectory equation $y = ax + b$, where the fitted line passes through the Center of Gravity (C.O.G) of the whole charge distribution and the quantity χ^2, defined in the following, is minimized:

$$\chi^2 = \frac{\sum_i Q_i d_i^2}{\sum_i Q_i} \tag{4.4}$$

where,

$$d_i = \sqrt{\frac{(y_i - (ax_i + b))^2}{1 + a^2}} \tag{4.5}$$

is the perpendicular distance to the fitted trajectory from the center of the i-th pad of coordinate (x_i,y_i) assuming the charge Q_i is localized at the center of the pad.

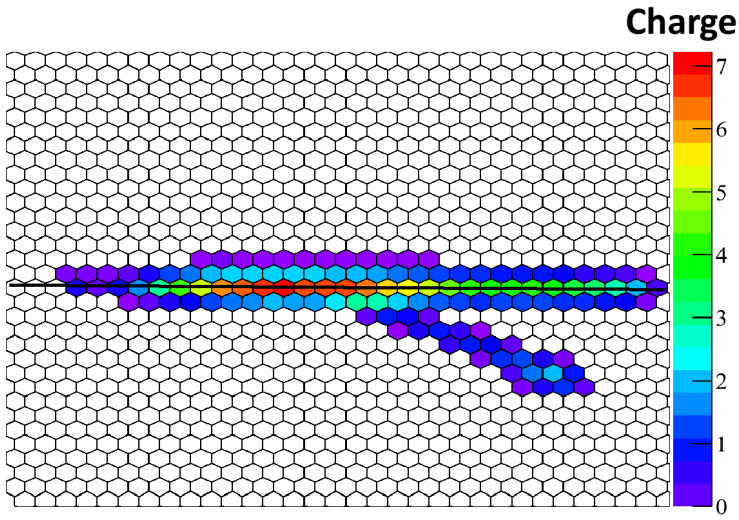

Figure 4.13: Beam trajectory reconstruction.

Since ^{56}Ni (α,α') ^{56}Ni* is a two-body reaction, there are two particles trajectories in MAYA: beam trajectory (^{56}Ni beam) and recoil-particle trajectory (recoil α-particle). The following sections describe the different steps followed in the trajectory reconstruction.

Beam trajectory reconstruction

Though the beam is spread from row#15 to row#19, a beam path is identified as a trajectory in which each of the rows#16, 17 and 18 of the cathode pad plane has at least 20 out of the possible 32 pads with non-zero charges.

The edges of the beam region (below row#16 and above row#18) can be identified from the multiplicity of pads in each row with non-zero charges. After identification of the beam path, the global fitting procedure is applied for beam trajectory reconstruction (see Fig. 4.13).

Beam subtraction

For better recoil-particle track reconstruction including the reconstruction of the vertex of the interaction, the charges due to the beam on the pads along its path have to be subtracted. In this data analysis, this subtraction is performed on an event-by-event basis. The steps of the event-by-event beam subtraction procedure are:

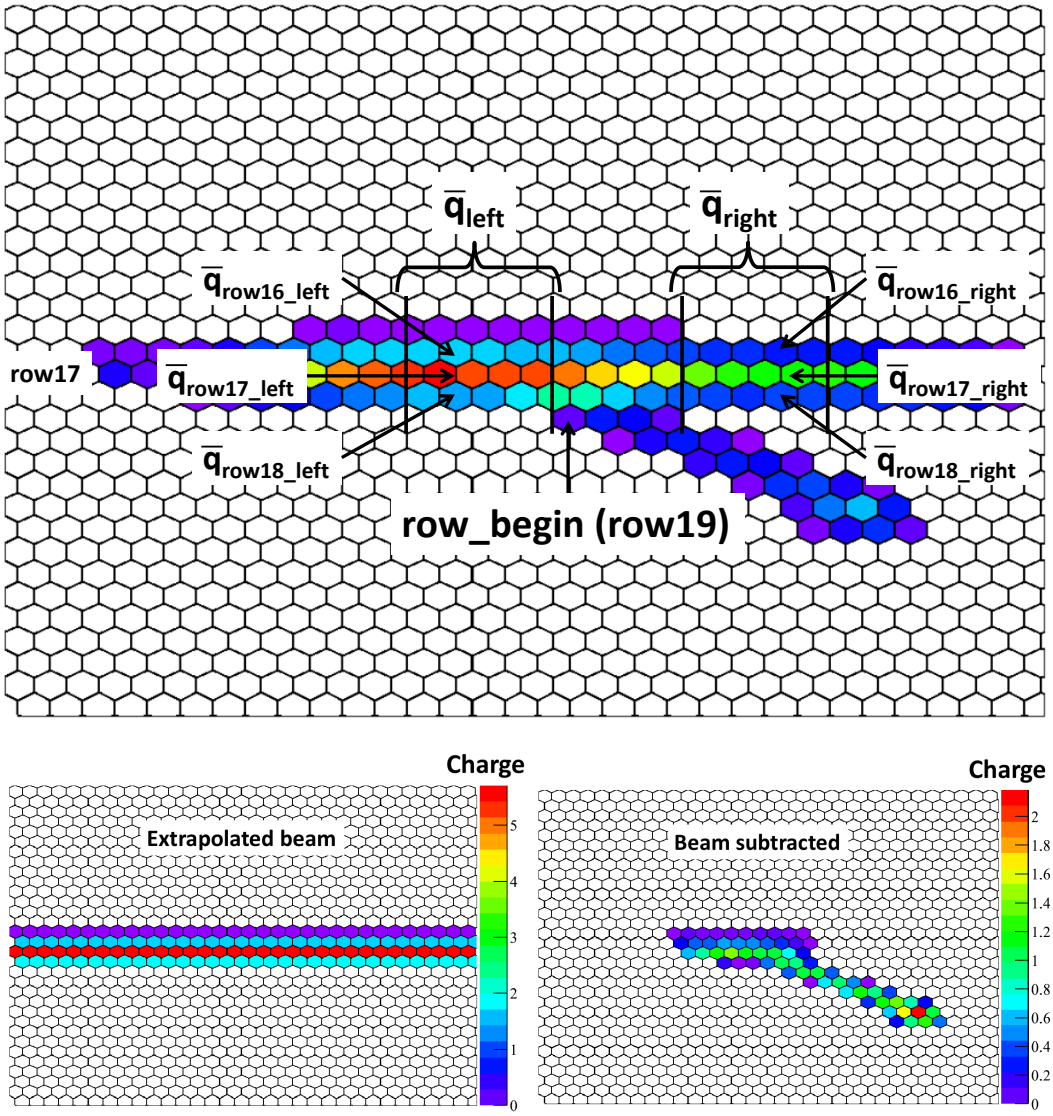

Figure 4.14: Beam subtraction method is defined in the top figure. In the bottom left figure the averaged beam which is to be subtracted is shown. The figure in the bottom right shows the result after subtracting the averaged beam. Note the difference in the scale of colors for the extrapolated beam and the beam subtracted recoil-particle track.

- For each event the beam region and the recoil-particle region are determined by looking

into the multiplicity of pads with non-zero charges in each row. In the beam region, out of 32 pads in each row there should be on average at least 20 pads with non-zero charges whereas in the recoil-particle region there should be on average 4 pads with non-zero charges in each row. With the help of this study the row is identified where the multiplicity of pads with non-zero charges changes significantly. In Fig. 4.14, the multiplicity of pads with non-zero charges changes from 26 in row#18 to 4 in row#19. Here, row#19 is termed as row_{begin} for the recoil-particle track.

- Above this row in the beam region (i.e., row#18 in Fig. 4.14) charge average $\overline{q}$ is taken for four consecutive columns on both sides of the recoil-particle track region ($\overline{q}_{i,left}$ and $\overline{q}_{i,right}$ for left and right sides of the recoil-particle track, respectively, with i as the row number). This process is applied for each row in the beam region.

- The averaged value per row is then subtracted along the entire beam region.

In Fig. 4.14, the beam subtraction method is schematically shown at the top, the extrapolated beam which is to be subtracted is shown at the bottom left and the result after the beam subtraction is shown at the bottom right. One more example of beam subtraction is also shown in Fig. 4.18.

Reconstruction of the recoil-particle trajectory

Due to the computational issue, reconstruction of the recoil-particle tracks has been divided into two categories:

- **Short-Tracks**: Recoil-particle tracks whose two-dimensional charge projection does not cross row#12 (if the recoil particle is scattered to the left side of the beam) or row#22 (if the recoil particle is scattered to the right side of the beam) (see Fig. 4.15).

- **Long-Tracks**: Recoil-particle tracks whose two-dimensional charge projection eventually cross row#12 (if the recoil particle is scattered to the left side of the beam) or row#22 (if the recoil particle is scattered to the right side of the beam) but does not reach to the edges of the cathode pad plane (see Fig. 4.15). In that case it is discarded as it could punch through the MAYA volume.

After beam subtraction the recoil particle is also fitted with the global fitting method within the region of recoil-particle charge projection. In the following sections, fitting procedures of long and short recoil-particle track will be discussed in details.

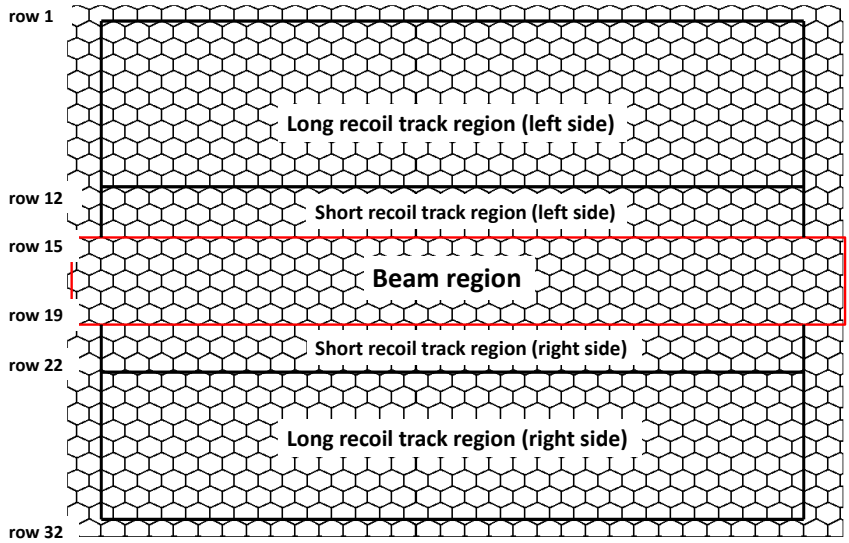

Figure 4.15: Beam and (short and long) recoil-particle track region in the cathode pad.

Fitting of long recoil-particle track

For fitting of the long recoil-particle tracks, the row for which the multiplicity of the pads with non-zero charges changes significantly is identified as row_{begin} and the first column of this row which has a pad with non-zero charge is identified as $column_{begin}$. Similarly the last row where the particle stops is identified as row_{end} and the last column of this row with a non-zero pad-charge is identified as $column_{end}$. After that a first fit for this long-track is performed within the region defined by (row_{begin}, $column_{begin}$) and (row_{end}, $column_{end}$).

The intersection point of the fitted trajectories for the recoil particle and the beam is calculated. This gives the vertex of interaction. The fitting procedure is described in the beginning of this section. A second fit for the long recoil track is performed with the vertex as the origin to get the proper two-dimensional range of the recoil particle, although the two-dimensional scattering angle (θ_{2d}) is not improved significantly for this second fit.

Figure 4.16 summarizes the whole procedure for the fitting of long recoil-particle track. Beam subtraction for long-track is less effective but it improves the scattering angle, the vertex of interaction and the reconstruction of the recoil-particle energy for short recoil-

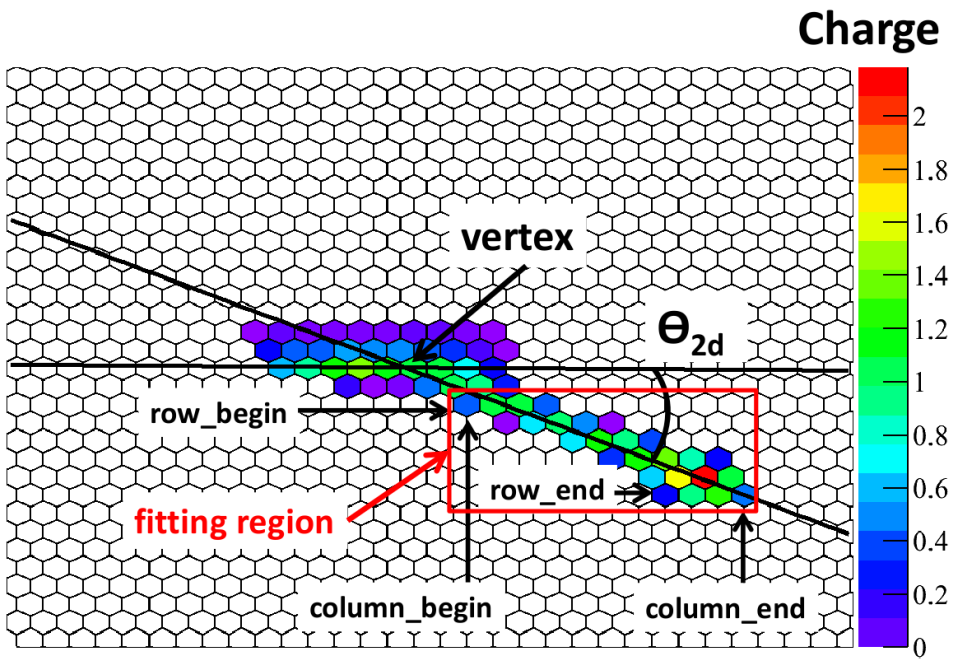

Figure 4.16: Fitting of long recoil track after beam subtraction.

particle tracks (see next Sub-section).

Fitting of short recoil-particle track

Fitting of short recoil-particle track is exactly the same as the fitting of long recoil-particle track, i.e., by finding out the row_{begin}, $column_{begin}$, row_{end} and $column_{end}$ for the recoil-particle track. But before subtraction of the beam and fitting of the recoil-particle track, a search for real short recoil-particle track is performed in order to avoid some fake "short-track" events due to statistical fluctuations of the detected charges of only beam events (i.e., no scattering of ^{56}Ni beam with the gas particles inside MAYA). The selection method is described below.

The row is identified as row_{begin} where the multiplicity of pads with non-zero charges changes significantly. Below this row in the beam region (i.e., row#15 in Fig. 4.17) average of pad-charges is taken within the columns of pads through which the recoil-particle track is extended ($\overline{q}_{short\_track}$). Averages of pad charges for this row are also taken on both sides of the recoil particle track and defined as $\overline{q}_{short\_track,left}$ and $\overline{q}_{short\_track,right}$ for left and right side, of

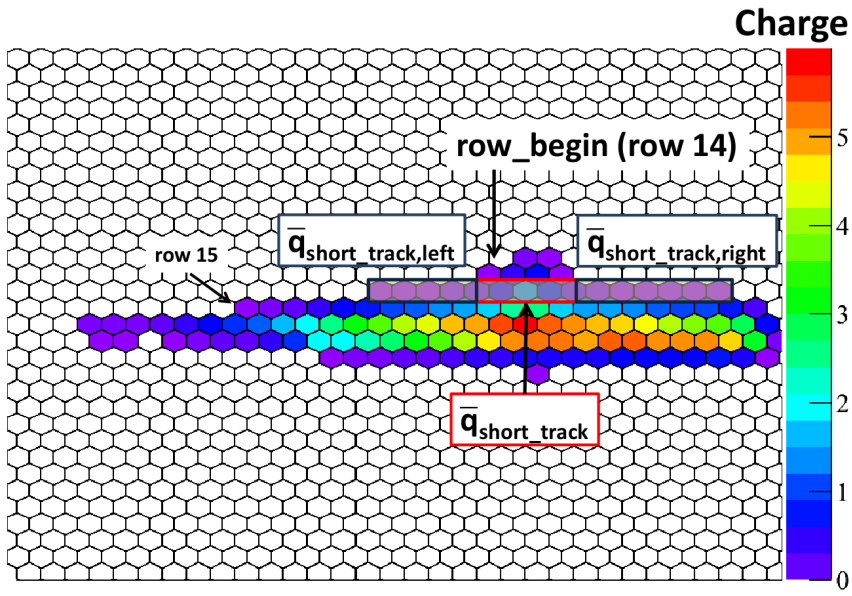

Figure 4.17: Selection of short recoil track.

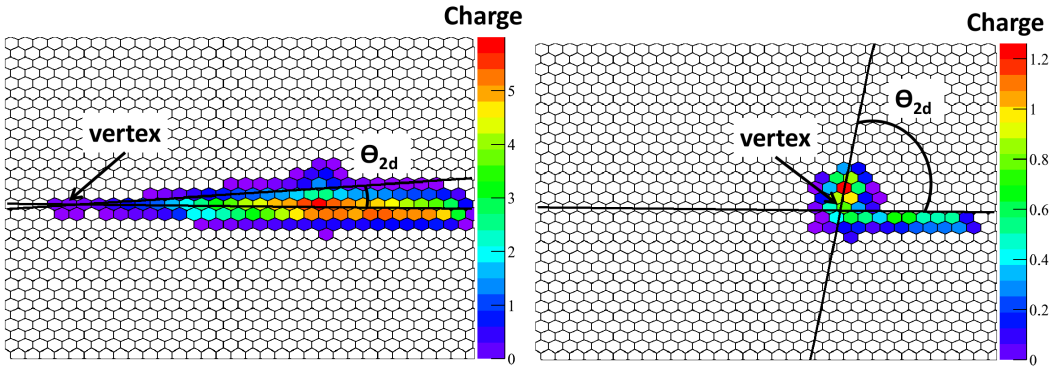

Figure 4.18: Fitting of short recoil track before (left panel) and after (right panel) beam subtraction.

the recoil-particle track, respectively.

Events are identified with real short-track recoil particle if and only if $\bar{q}_{short\_track} > \bar{q}_{short\_track,left}$ and $\bar{q}_{short\_track} > \bar{q}_{short\_track,right}$. After that the short recoil track is fitted in the same way as the long-track fitting.

Figure 4.18 shows the short track fitting before and after the beam subtraction. Here, beam subtraction improves the vertex, scattering angle and two-dimensional range reconstruc-

tion.

4.3.2 Determination of reaction plane

^{56}Ni(α, α')^{56}Ni* is a two-body reaction. The reaction occurs in a plane which is not necessarily parallel to the cathode pad. Since MAYA is a time-charge-projection chamber, to retrieve the third dimension, timing information from the anode wires is needed to measure the drift-time of the electrons from the recoil-particle ionization. From the measured drift-time, the inclination-angle of the reaction plane with respect to the cathode pad plane (ϕ angle) can be determined.

Let us assume that some electrons from the ionizing particle arrive at the anode wire j at position y_j at time t_j. Therefore, the drift-distance of the electrons is:

$$d_j = V_d \times t_j \tag{4.6}$$

where V_d is the drift-velocity of the electrons in the gas mixture (95% He + 5% CF_4) at 500 mbar pressure. The i-th wire will receive the electrons at time t_i. t_i can be larger or smaller than t_j depending on the recoil-particle path (see Fig. 4.19). The drift-distances (d_j) are then plotted against the positions of the corresponding wires (y_j) and a linear fit is performed through the points (see Fig. 4.20).

The slope of the fit leads to the angle of the reaction plane (ϕ) with

$$\tan\phi = a_{fit} \tag{4.7}$$

where a_{fit} is the slope of the linear fit $a_{fit}x + b_{fit}$. Therefore, to obtain the ϕ angle, besides the timing information of the amplification wires, the drift-velocity of electrons in 95% He + 5% CF_4 gas mixture is also necessary. In the next sub-section, measurements leading to the drift velocity of the electrons are described.

Drift-velocity measurement

Since the electrostatic mask is extended from row#15 to row#19, the MAYA chamber was rotated by an angle of 8° with respect to the incoming beam direction in order to get proper drift-velocity measurement. In this way part of the beam trajectory is out of the mask region

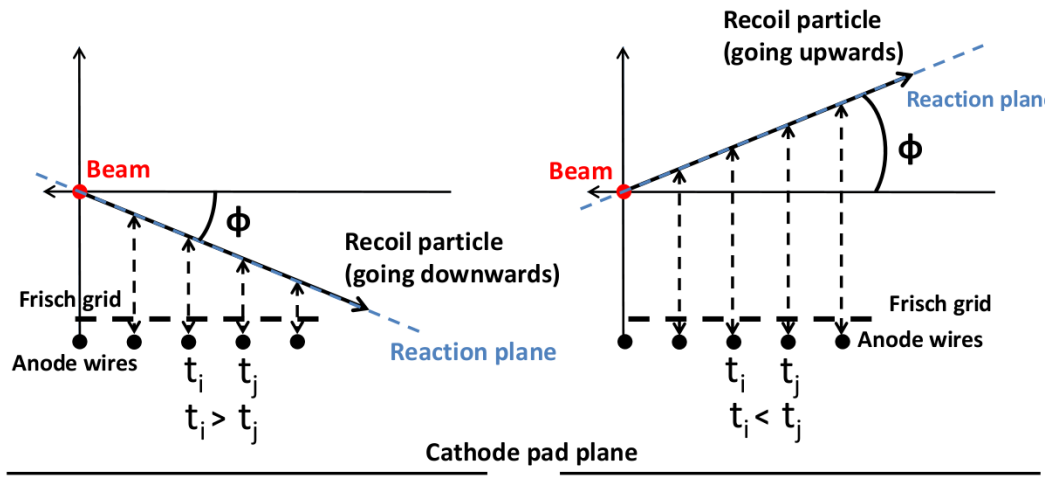

Figure 4.19: Determination of reaction-plane angle. Left panel: recoil-particle track is going downwards; right panel: recoil-particle track is going upwards.

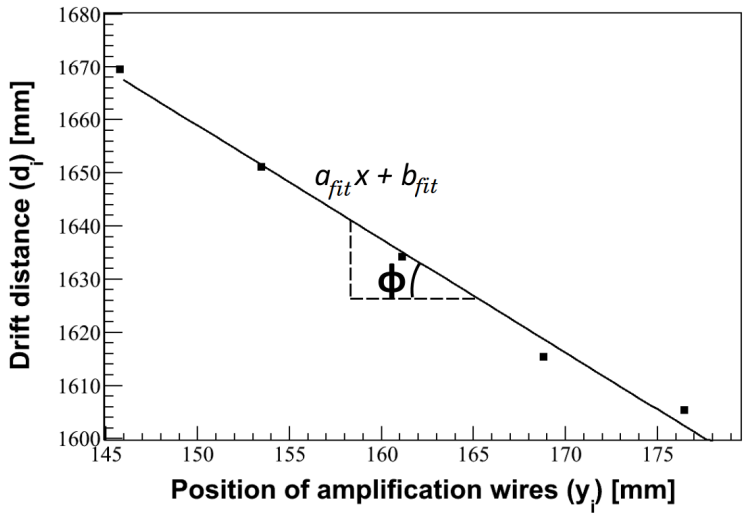

Figure 4.20: Determination of ϕ angle.

(see Fig. 4.21).

In this orientation of the MAYA chamber, more amplification wires can see the drifting electrons from the beam ionization compared to the normal position of MAYA where four or

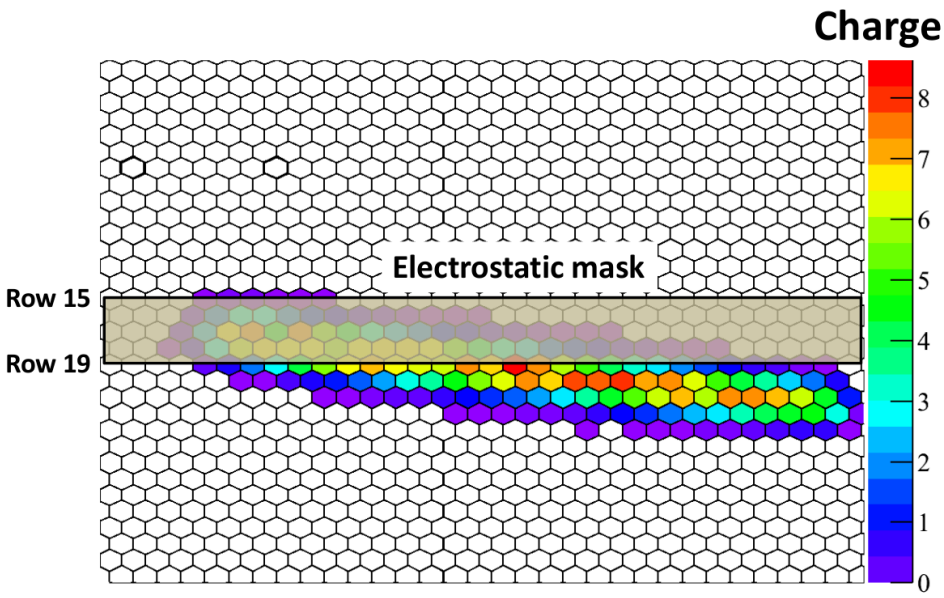

Figure 4.21: Rotation of MAYA chamber with respect to the incoming beam.

five wires only can receive the drifting electrons. In this case the beam is not hitting the beam stopper but rather Si#9.

With the Si trigger the timing information from the wires was encoded, i.e. the drift time T_d plus the delay time D imposed on the wire signal (see Fig. 4.22). The delay time D is obtained with the self-triggering of the amplification wires. It is basically the response time of the electronics. In Fig. 4.22, the timing response of wire#20 both for Si-trigger and wire self-trigger are shown.

In this way, the drift time for every wire which receives the electrons is measured and an average drift time of 6.05 μs is obtained. The drift distance is the distance between the beam plane and the Frisch grid considering the beam to be in the middle between the upper cathode plate and the Frisch grid. This is the region of constant drift. With this method, the measured drift velocity of the electrons in 95% He + 5% CF_4 gas mixture at 500 mbar pressure is measured to be 16.5 mm μs^{-1} which is in agreement with the results of the GARFIELD simulations [76] [77].

GARFILED is a program developed by CERN to simulate the electron drift in gaseous detectors. From the simulations, the drift velocity of the electrons in 95% He + 5% CF_4 gas mixture at 0.48 atm pressure is calculated to be 17.5 mm μs^{-1} at an electric field of 150 V cm^{-1} (see

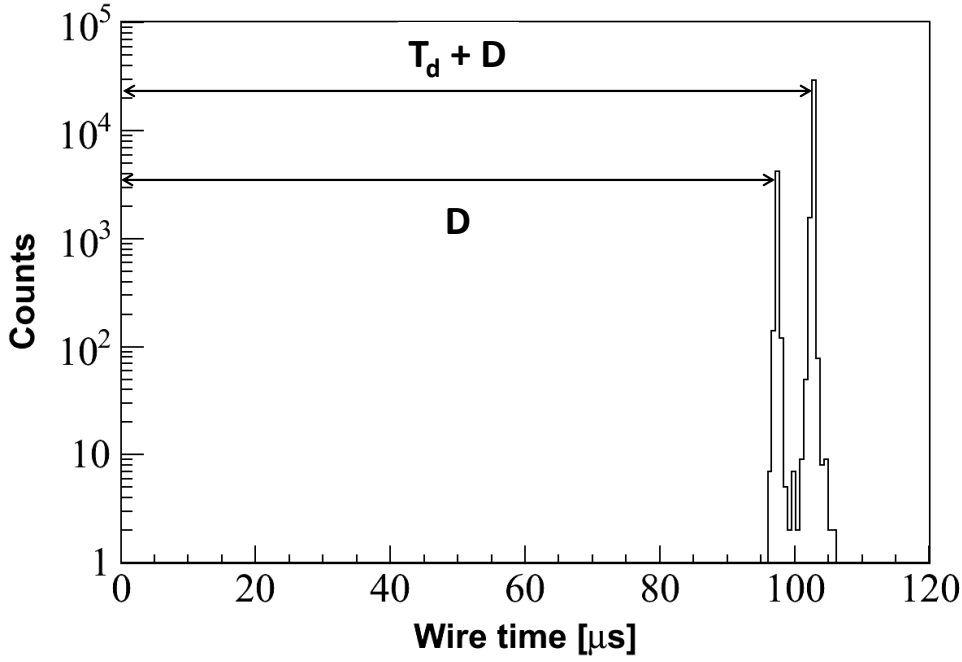

Figure 4.22: Drift time (T_d) plus delay time (D) with Si trigger and delay time (D) with wire self-trigger for wire#20.

Fig. 4.23)[2].

4.3.3 Range and scattering-angle reconstruction of the recoil particle

When a charged particle travels through a gas it loses its energy by ionizing the gas. As the energy of the particle decreases, the interaction cross section with the gas particles increases. Therefore, in the energy-loss profile a peak occurs before the particle completely stops. This is known as the Bragg peak.

In MAYA, charges induced on the cathode pads are proportional to the energy of the ionizing particle and charges are localized at the center of each pad. The whole track length on

[2]In MAYA, distance of the cathode plate at the top to the Frisch grid is 20 cm. Cathode plate is maintained at -3000 V and Frisch grid is maintained 0 V. Therefore, the electric field is 150 V cm^{-1}.

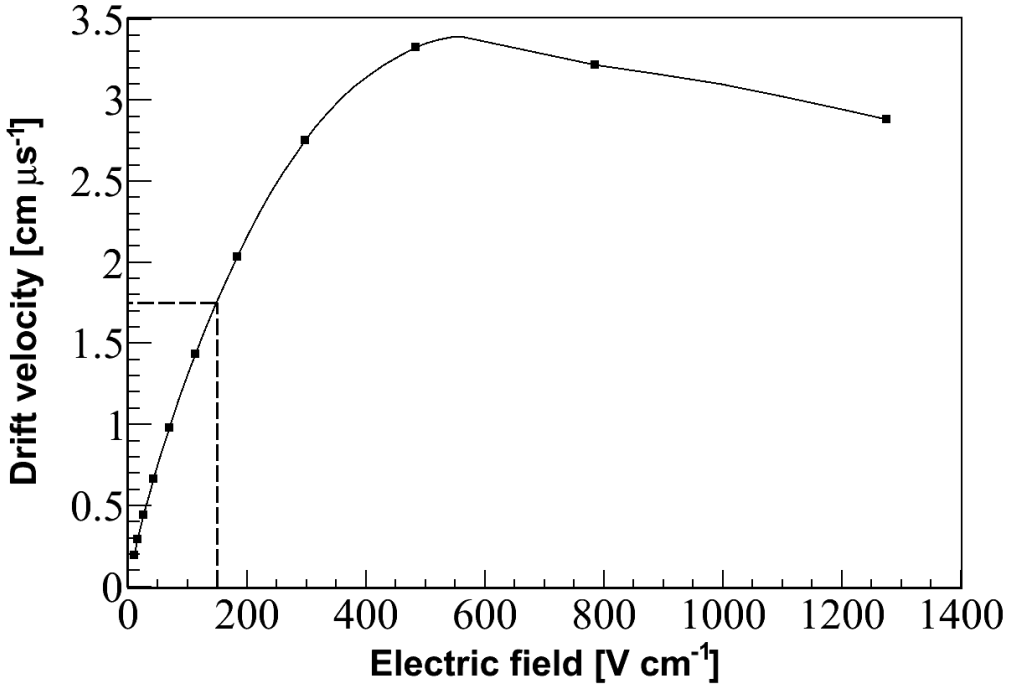

Figure 4.23: Electron drift velocity using GARFIELD simulation.

the cathode pads is a projection of the ionization profile of the particle in two dimensions.

It is convenient to obtain the charge projection along any of the three symmetry axes of a hexagon (see Fig. 4.2) because of the hexagonal shape of the cathode pads. The symmetry axis which is the closest to the normal to the fitted particle trajectory is chosen as the axis on which the charges are to be projected on the cathode pads. The cumulative sum of the charges on the pads are projected along the normal onto the chosen symmetry axis and plotted versus the distance from the vertex of interaction. This process is carried out throughout the whole path of the recoil particle and it therefore gives the energy-loss profile and the Bragg peak of the particle in two dimensions. In Fig. 4.24, examples of obtaining charge projections along three symmetry axes of hexagon are shown.

Once the maximum of the ionization profile is identified as the Bragg peak, 20% of the height of the Bragg peak[3] (details will be given in Chapter 5) is taken and the corresponding

[3]20% of the Bragg peak is taken as the range of the particle and it is validated by SRIM.

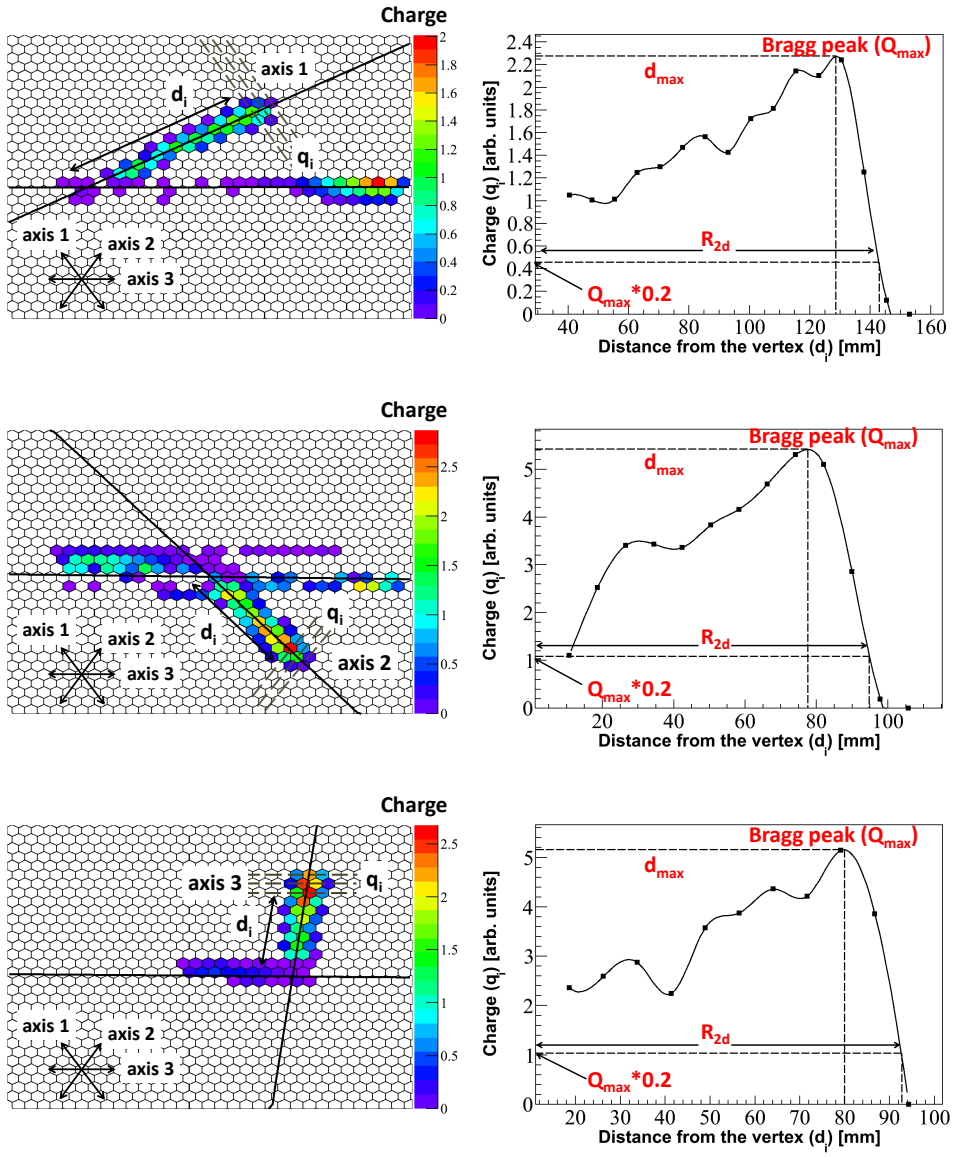

Figure 4.24: Examples of range and scattering-angle reconstruction along three symmetry axes of the hexagon.

distance is defined as the two-dimensional range R_{2d}.

The two-dimensional scattering angle θ_{2d} is the angle between the fitted trajectories of the

beam and the recoil particle. Since the ϕ angle can be obtained from the timing information of the amplification wires, the proper range (R) and scattering angle (θ) in 3-dimensions can be reconstructed from R_{2d} and θ_{2d}.

From Fig. 4.3, it can be shown that:

$$R = R_{2d}\sqrt{1 + \sin^2\theta_{2d}\tan^2\phi} \tag{4.8}$$

and

$$\cos\theta = \frac{\cos\theta_{2d}}{\sqrt{1 + \sin^2\theta_{2d}\tan^2\phi}} \tag{4.9}$$

From the range of the particle, energy of the recoil particle can be extracted as discussed in the following.

4.3.4 Energy reconstruction of the recoil particle

Since the range of a particle in a certain medium is uniquely related to its energy it is possible to extract the energy of the recoil particle in MAYA once its range is known. One should emphasize that it is possible to extract the energy only for the particles that stop inside MAYA and do not punch through the sides.

In this data analysis, energy of the recoil particle is measured from its range using tables from the SRIM program [61]. Figure. 4.25 shows the relationship between the range and energy of α-particle in 95% He and 5% CF_4 gas mixture at 500 mbar pressure.

4.4 Event selection

4.4.1 Selection of the ^{56}Ni beam

In our experiment, the ^{56}Ni beam was contaminated with a few percent of ^{55}Co and ^{53}Fe. The identification matrix for ^{56}Ni shown in Fig. 3.5 is obtained using the energy deposit (ΔE) in the Si detector placed in the experimental hall D6. Since the Si detector in D6 can only be used for low-intensity beam, it was not used for beam selection during the data-taking process.

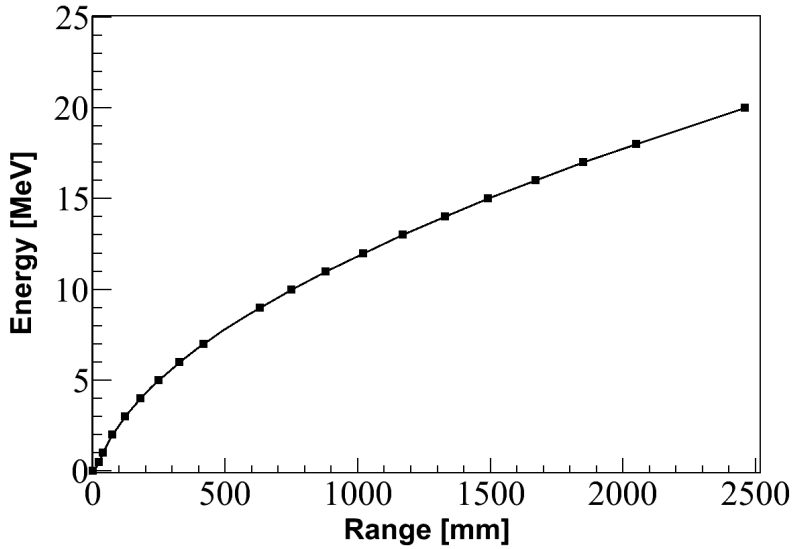

Figure 4.25: Calculation of energy of α-particle from its range in a gas mixture of 95% He + 5% CF_4 at 500 mbar pressure using SRIM [61].

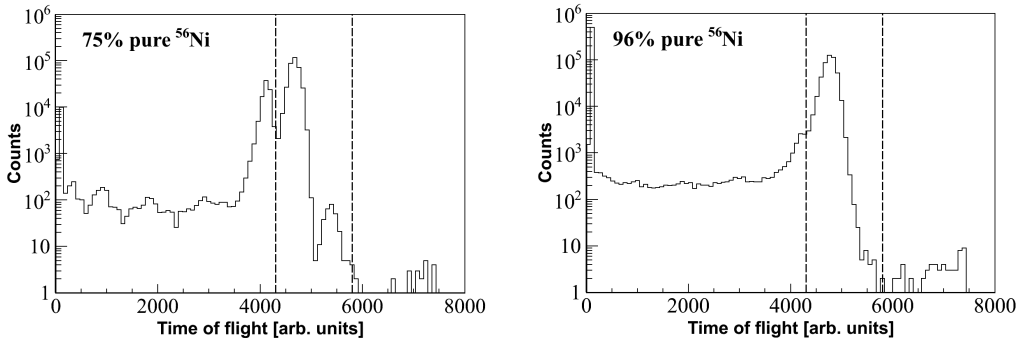

Figure 4.26: ^{56}Ni selection: identification matrix of ^{56}Ni using energy deposited in Si detector in D6 and time-of-flight between MCPA and plastic scintillator (left panel), one-dimensional time-of-flight between MCPA and plastic scintillator (right panel).

The incoming beam particles can be identified by looking into the time-of-flight of particles between the Micro-Channel-Plate-Analyzer (MCPA) and the plastic scintillator detector (see Fig. 3.3). From Fig. 4.26, it is clear that the peak between the channel numbers 4300 and 5800 depicts ^{56}Ni. In the left panel of Fig. 4.26 where the purity of ^{56}Ni beam is 75%, the

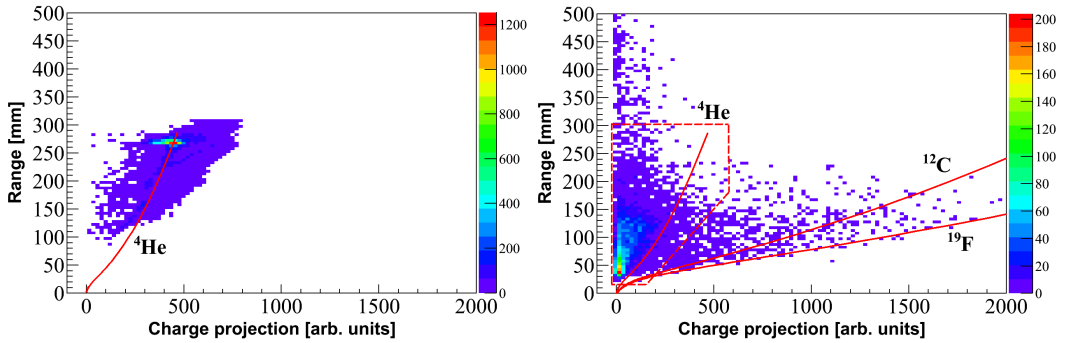

Figure 4.27: Left panel: identification matrix for α-source run. the red solid line represent the range vs. energy relationship calculated for He at 95% He and 5% CF_4 gas mixture at 500 mbar pressure. Right panel: Identification matrix for the recoil particles as measured inside MAYA with ^{56}Ni beam runs. The red solid lines represent the range vs. energy relationship calculated for He, C and F in 95% He and 5% CF_4 gas mixture at 500 mbar pressure. The normalization factor between the charge projection and energy is obtained from alpha source run as shown in the left panel. The events are considered which are inside the area defined by the red dashed polygon.

peak below channel number 4300 could be the contributions from ^{55}Co or ^{53}Fe. In the right panel of Fig. 4.26 where the purity of ^{56}Ni beam is 96%, the peak below channel number 4300 disappears. However, the upper limit of the selection window has been set to channel number 5800 which includes the small peak appearing at channel number around 5500 for 75% purity of ^{56}Ni beam which also disappears for 96% pure ^{56}Ni beam.

4.4.2 Selection of the recoil α-particle

Since the charges on the cathode pads are proportional to the energy of the ionizing particle and since there is a unique relationship between range, energy and nature of the recoil particle, it is possible to select recoil α-particles from recoil carbon and fluorine[4] to reduce the background. Identification for the recoil particle can be done by plotting its range (R) and total charge (Q) for its whole track length starting from the vertex of the interaction till its stopping point inside MAYA, with Q defined as:

$$Q = \sum_k q_k \tag{4.10}$$

[4]The gas mixture inside MAYA is composed of 95% He and 5% CF_4.

where k is the index running over the cathode pads within the recoil particle path and q_k is the corresponding charge on the pad.

The left panel of Fig. 4.27 shows the range vs. charge projection plot for α-source (^{239}Pu; E_α = 5.2 MeV) run. The red solid line represents the range-energy relationship for He, calculated at 95% He and 5% CF_4 gas mixture at 500 mbar pressure. Since there is no absolute calibration of the charge of the pads in energy, SRIM calculation for He has been normalized with respect to the α-source run. In the right panel, the identification matrix for the recoil particles with ^{56}Ni beam runs is shown. The same normalization factor obtained from the α-source run has been applied to the SRIM calculations for He, C and F and these calculations are shown in red solid lines in the right panel of Fig. 4.27. These calculated lines shows the upper limit of the particle identification. Therefore, only events which are in the area defined by the red dashed polygon are considered in this analysis.

4.4.3 Geometrical selections of the events in MAYA

Kinematic variables are only reconstructed for those events which stop inside the MAYA volume. The following geometrical cuts are made during data analysis in order to choose the proper events:

- The range (R) of the recoil particle should be less than 350 mm which is the maximum possible track length for a recoil particle that stops inside the MAYA volume.

- The two-dimensional scattering angle (θ_{2d}) should be greater than 10° because for smaller laboratory scattering angles, the recoil particle is too close to the beam path. It is, therefore, impossible to distinguish whether the charge distribution comes from recoil particle ionization or from beam ionization.

The elastic scattering occurs around 90° in the laboratory frame. There is no inelastic scattering above 90° scattering angle. But due to the angular resolution of MAYA, especially for short recoil particles, an upper limit of 100° has been set.

- The x-coordinate of the vertex of interaction should be between 50 mm and 250 mm. Figure 4.28 shows the distribution of the x-coordinates of the vertex of interaction (along the beam line) for events from the beam-time runs. Below 50 mm there is an increase of counts because of the geometrical acceptance of the MAYA detector and the fake recoil particle events caused by the reactions in the entrance window.

The selection of the upper limit of the x-coordinate of the vertex of interaction as 250 mm

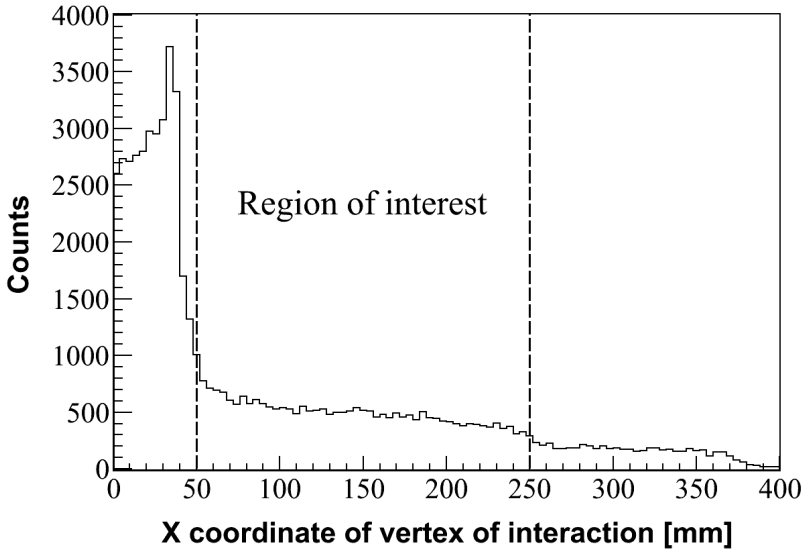

Figure 4.28: Selection of the vertex of interaction.

eliminates events that can be generated from the interaction of the beam with the beam-stopper (diamond detector).

- The multiplicity of pads with non-zero charge in each row outside the beam region (i.e., row#1 to row#14 on the left side of the beam and row#20 to row#32 on the right side of the beam) should be less than 10, otherwise it could be due to fake events caused by sparking inside the active volume.

- If the recoil-particle track has non-zero pad-charges at the edges of the cathode pad plane (i.e., in row#1 or row#32 or column#2 or column#31 and outside of the beam region) the event is discarded because the recoil particle may punch through MAYA (see Fig. 4.15).

One should note that the above geometrical selections have also been considered in analysing the data produced by the simulations and any inefficiencies so created could be taken care of during the efficiency correction.

Chapter 5

Simulation

Simulations were performed in order to calculate the acceptances and the efficiencies (geometric and event reconstruction) of the MAYA detector and to estimate the resolutions in reconstructing the kinematic variables. This chapter begins with the description of the method of simulating events in MAYA. The methods of extracting the range and the scattering angle of the recoil particle are the same as for the experimental data and are described in the previous chapter. This chapter ends with the estimation of the resolutions for the CM scattering angle, the excitation energy of ^{56}Ni and with discussions on acceptances and efficiencies.

5.1 Event generation in MAYA

Events are generated in MAYA for excitation energies of ^{56}Ni ranging from 0 MeV (elastic scattering) to 50 MeV in steps of 200 keV. For each excitation energy of ^{56}Ni, 500 events are generated for each CM angle ranging from 0° CM to 10° CM in steps of 0.1°. For each event, the vertex of interaction is randomized throughout row#17 of the cathode pad plane, i.e., along the beam direction (see Fig. 4.2), and the ϕ-angle is randomized from $-180°$ to +180° considering the fact that the recoil particle can be scattered in any direction isotropically in MAYA and a reaction can take place anywhere along the beam path.

5.1.1 Energy-loss calculation for the ^{56}Ni beam and the recoil α-particle

Energy losses of all charge particles were calculated using SRIM [61] for a mixture of 95% He and 5% CF_4 at a pressure of 500 mbar.

Energy loss of ^{56}Ni beam particle

The incoming beam of ^{56}Ni has an energy of 50 MeV/u. In the simulations, it has been considered that the beam is always in a plane, parallel to the cathode pad plane.

Energy loss of recoil α-particle

Since the ϕ angle, i.e., the reaction-plane angle is also randomized for the simulated events, energy loss for the recoil α-particle for a given excitation energy of ^{56}Ni is calculated in a multi-step process. From Eqn. 4.8, when ϕ = 0, R_{3d} (also denoted as R) = R_{2d}, i.e., the three-dimensional range is equal to its two-dimensional projection length on the cathode pads. But if $\phi \neq 0$ then $R_{2d} < R_{3d}$ which means that the projected two-dimensional range is smaller than the three-dimensional range. Therefore, the two-dimensional energy-loss profile is also squeezed (see Fig. 5.2) and this leads to variations of the pad charges for different ϕ angles of the recoil α-particles. Taking into account all these factors, energy loss of the recoil α-particle for a given θ_{CM}, ϕ angle and excitation energy of ^{56}Ni is calculated in the following way:

i) Laboratory scattering angle (θ or θ_{3d}) is calculated corresponding to the given θ_{CM} angle using LISE++ software [78].

ii) As the laboratory scattering angle is known for a given θ_{CM}, energy of the recoil α-particle (E_{3d}) can be deduced for the given excitation energy of ^{56}Ni.

In the left panel of Fig. 5.1, the relationship between θ and θ_{CM} is shown for 0 MeV (elastic scattering), 20 MeV and 30 MeV excitation energy of ^{56}Ni. As an example, let us consider 5° CM angle. The corresponding laboratory angles for 0 MeV, 20 MeV and 30 MeV excitation energy of ^{56}Ni are obtained from this plot and defined as $\theta_{Lab\ 0\ MeV}$, $\theta_{Lab\ 20\ MeV}$ and $\theta_{Lab\ 30\ MeV}$, respectively. In the right of Fig. 5.1, the kinematics curves for the recoil α-particle energy versus the laboratory scattering angle are shown for 0 MeV (elastic scattering), 20 MeV and 30 MeV excitation energy of ^{56}Ni. Here, $E_{3d\ 0\ MeV}$, $E_{3d\ 20\ MeV}$ and $E_{3d\ 30\ MeV}$ are the energies of the recoil α-particle for 5° CM angle for 0 MeV (elastic scattering), 20 MeV and 30 MeV excitation energy of ^{56}Ni, respectively.

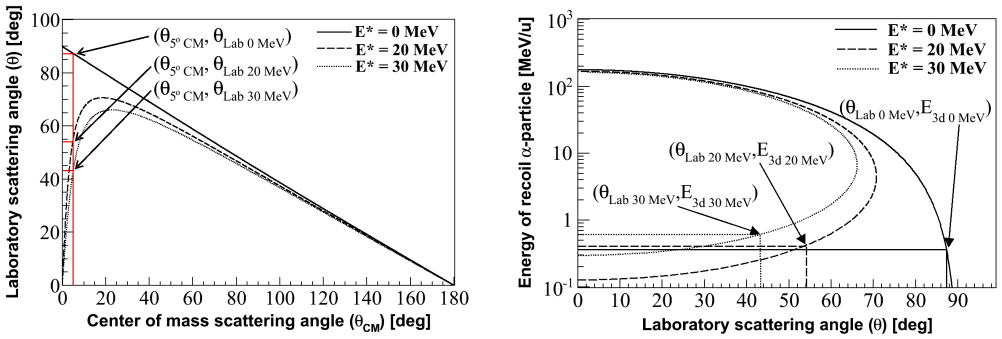

Figure 5.1: Left panel: relation between CM angle and laboratory angle of the recoil α-particle for 0 MeV, 20 MeV and 30 MeV excitation energy of ^{56}Ni. Right panel: plot of laboratory angle versus energy of recoil α-particle for 0 MeV, 20 MeV and 30 MeV excitation energy of ^{56}Ni. These figures are obtained for an incoming energy 50 MeV/u for ^{56}Ni.

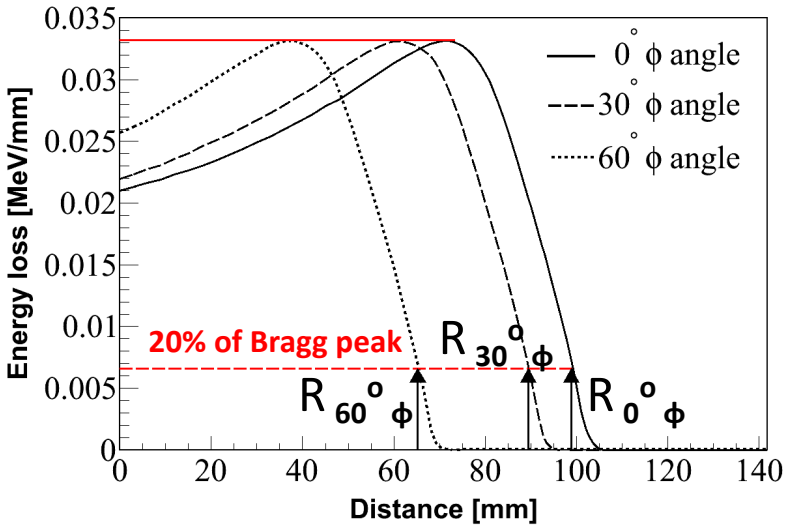

Figure 5.2: Two-dimensional range of the recoil α-particle for 0°, 30° and 60° ϕ angles for 20 MeV excitation energy of ^{56}Ni and θ_{Lab} = 60°.

iii) After obtaining the laboratory scattering angle θ_{3d}, the two-dimensional laboratory scattering angle (θ_{2d}) is calculated for a given ϕ angle using Eqn. 4.9.

iv) Since the energy (E_{3d}) of a particle is uniquely related to its range (R_{3d}) (see Fig. 4.25), R_{3d} (i.e. R) can be calculated and then the two-dimensional range (R_{2d}) of the recoil α-particle can be calculated from Eqn. 4.8 for the given ϕ angle once θ_{2d} is known from step iii).

v) The "two-dimensional" energy (E_{2d}) of the recoil α-particle can be obtained from the range to energy relationship once (R_{2d}) is known.

vi) Energy loss for recoil α-particle of energy E_{2d} is then obtained using SRIM.

It is to be noted here that when $\phi = 0$ then $E_{2d} = E_{3d}$, $R_{2d} = R_{3d}$ and $\theta_{2d} = \theta_{3d}$, otherwise $E_{2d} < E_{3d}$, $R_{2d} < R_{3d}$ and $\theta_{2d} < \theta_{3d}$, provided that the particle stops inside MAYA.

In Fig. 5.2, the two-dimensional energy loss of α-particle at 60° laboratory scattering angle for 20 MeV excitation energy of ^{56}Ni is shown for 0°, 30° and 60° ϕ angles. It is clear that when $\phi \neq 0$, the two-dimensional range is smaller than the three-dimensional range but the two-dimensional range has to be corrected for the given ϕ-angle to get the proper three-dimensional range. The three-dimensional range is independent of ϕ-angle. From the energy loss of the ionizing particle obtained from SRIM, charges are projected on the pads in the simulation.

5.1.2 Two-dimensional charge projection from energy-loss profile of beam and recoil α-particle

Following the work of Lau et al. [79], one can show that the charge distribution in a precision cathode-strip chamber agrees better with the *Hyperbolic Secant Squared* (SECHS) analytic function than any other analytical functions (e.g. Gaussian, Lorentzian) (see Fig. 5.3). Therefore, here the charges are also distributed on the cathode pads in MAYA following the SECHS method.

According to the SECHS method, the charge on a pad is defined as:

$$Q = \frac{a_1}{\cosh^2\left(\pi(x - a_2)/a_3\right)} \tag{5.1}$$

where a_1 is the overall normalization, a_2 is the centroid, and a_3 is the width of the charge distribution. In MAYA, a_2 is the position of the center of the cathode pad.

To obtain a_3, i.e., the width of the charge distribution, 5000 events with no scattering of ^{56}Ni beam with helium inside the MAYA chamber (the so-called beam-only events) from the experimental data are chosen and averaged out (see left panel of Fig. 5.4). Then, the to-

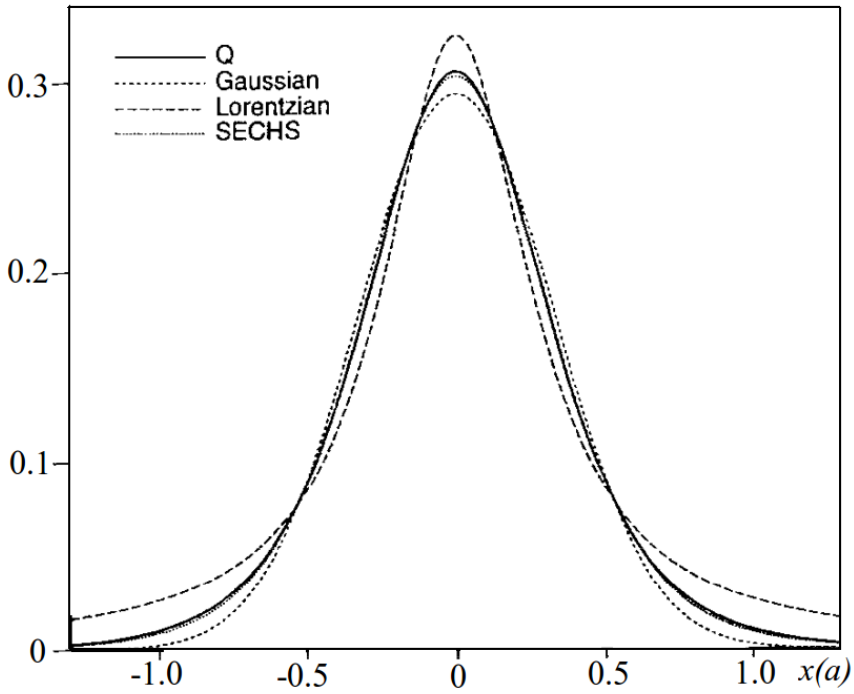

Figure 5.3: Fitting of the charge distribution in a precision cathode-strip chamber with different analytical functions [79].

tal charge of each row has been plotted against the distance of the corresponding row from the 1^{st} row of the cathode pad. The data points are then fitted with the SECHS formula mentioned in Eqn. 5.1 to obtain the width parameter a_3. The results of the fit are shown for the experimental data (see Fig. 5.4: right panel; solid line) and the simulated data (see Fig. 5.4: right panel; dashed line). The value of the width parameter obtained for the simulated data is 31.4 mm whereas for the experimental data it is 31.1 mm. There is also a difference in the centroid positions of the fits for the simulated and the experimental data, because of the symmetric beam simulation and in experiment, the beam is not symmetric due to the presence of the electrostatic mask under the beam. However, this effect is negligible and will not affect the reconstruction of kinematic variables and efficiency corrections because in the analysis the angle between the beam and the recoil particle is calculated on an event-by-event basis.

When charges are induced on a certain cathode pad, charges are also induced on its neighbor pads (see Fig. 5.5). Since the charges are localized at the center of the cathode pads, the

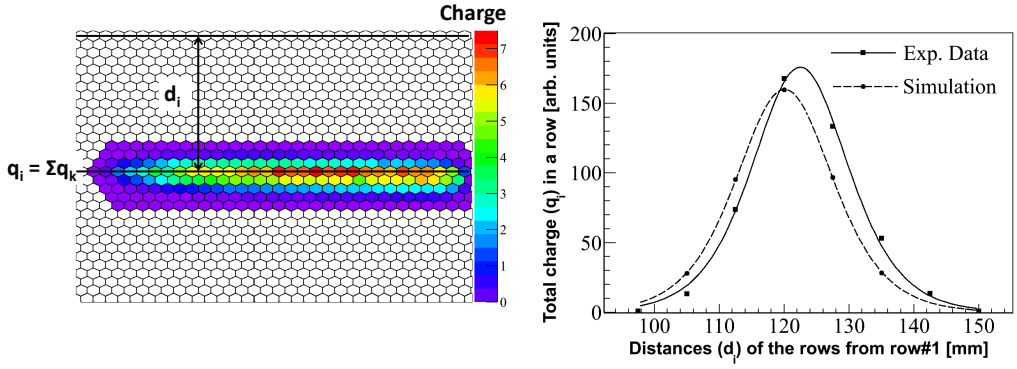

Figure 5.4: Determination of the width of the charge distribution. Left panel shows the averaged charge distribution due to beam from the experimental data. Right panel shows the SECHS fitting for experimental data (solid line) and simulated data (dashed line).

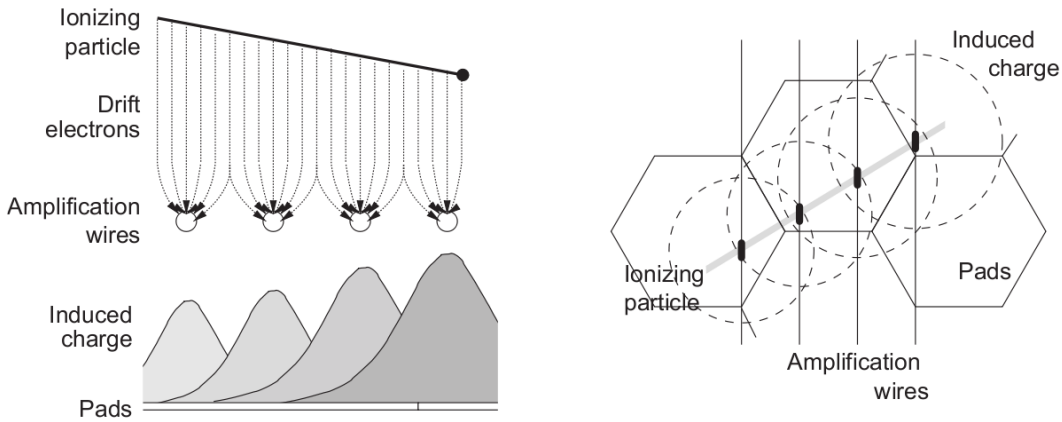

Figure 5.5: Schematic representation of distribution of charges induced on neighboring pads due to avalanches on amplification wires [75].

quantity "$x - a_2$" from Eqn. 5.1, is the distance of the center of the main pad from the center of its neighboring pad (see Fig. 5.6). In this simulation, next-to-next neighbors of the main pad (see Fig. 5.6) have also been taken into account using the distance between the centers of the main pad and next-to-next neighboring pads. Note that, here the parameter a_1 is the charge of the main pad, calculated from dE/dx, i.e., the energy loss per unit length.

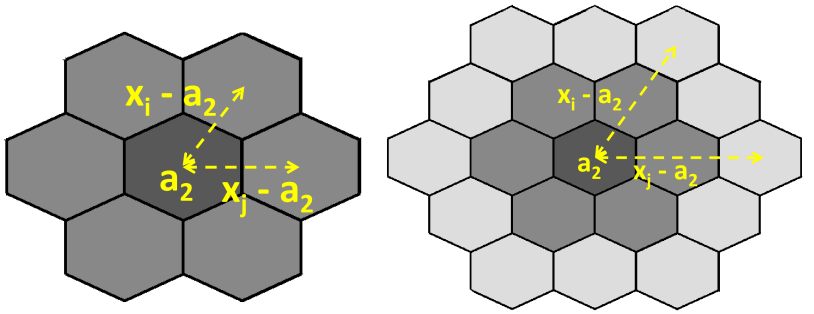

Figure 5.6: Next (left figure) and next-to-next (right figure) neighbor pads of the main pad.

Two-dimensional beam-path reconstruction

Since in the present experiment, the ^{56}Ni beam is parallel to row#17, pads in this row are considered as the main pads for the charge distribution of the beam. In the simulations, it has also been considered that the beam is in a plane parallel to the cathode pad plane. The energy loss of the ^{56}Ni beam calculated from SRIM is integrated over the pads corresponding to row#17 considering the first pad of row#17 to be the origin of the beam path inside MAYA.

Two-dimensional recoil-path reconstruction

Since the recoil particle can be scattered in any direction, efforts have been made to calculate the proper energy loss of the recoil particle taking into account all possible directions of scattering. Eventually, the vertex of interaction can be anywhere along the beam path, therefore it has been randomized in the simulation throughout row#17.

For a given ϕ angle and θ_{CM} angle, θ_{2d} is calculated and pads are filled with charges corresponding to the energy loss of the recoil α-particle having energy E_{2d} (see Sub-section 5.1.1) at θ_{2d} angle from the origin, i.e., the given vertex of interaction. After that, the next-neighbor and next-to-next neighbor pads are filled with charges according to SECHS distribution.

Efficiency correction due to end effects on the cathode pads

The first two rows of the cathode pads were not functioning during our experiment. From Fig. 4.4, the breaks in the pulser alignment of the cathode pads lead to the fact that the corresponding pads were not functioning. To take into account these inefficiencies, simulations

have been done accordingly, i.e., in the simulation the cathode pads which were not functioning during the experiment are also not filled with charges. Note that this is done not only for efficiency correction but also to test if this generates spurious structures in the reconstruction of kinematic variables.

5.1.3 ϕ angle simulation

For ϕ angle simulation, simulation of the timing resolution of the amplification wires is needed. From the kinematics and the given ϕ-angle, the number of wires that could possibly fire outside the beam region can be calculated. Therefore, each wire outside the beam region is assigned with a time in μs in such a way that the extracted ϕ-angle is equal to the given ϕ-angle within the experimental uncertainty. In order to simulate the time response of the wire, we used the drift velocity of the electrons at our experimental conditions which is 16.5 mm/μs and the distance between the consecutive wires which is 7.6 mm. In Fig. 5.7, the ϕ-angle distributions for experimental data and simulated data are shown. The discrepancies between the simulated data and the experimental data above 60° ϕ-angle could be due to the presence of the mask under the beam. The extension of ϕ-angle is from $-90°$ to

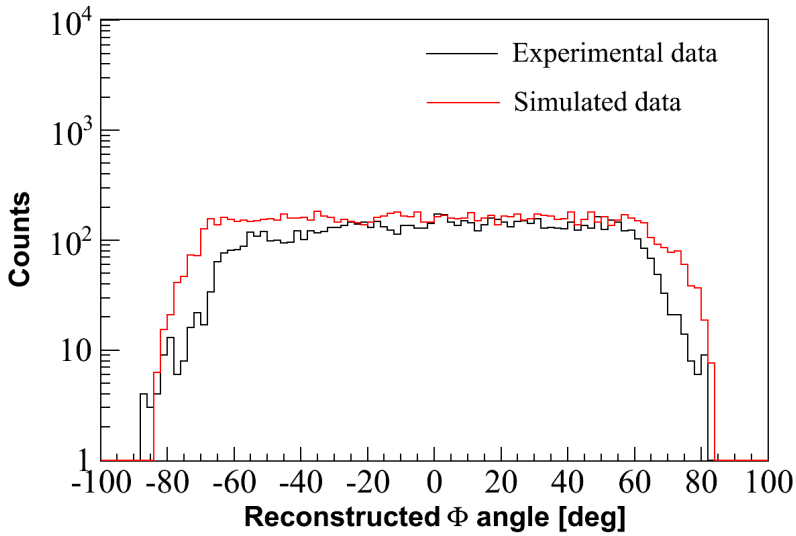

Figure 5.7: Reconstructed ϕ-angle for experimental data (black solid line) and for simulated data (red solid line).

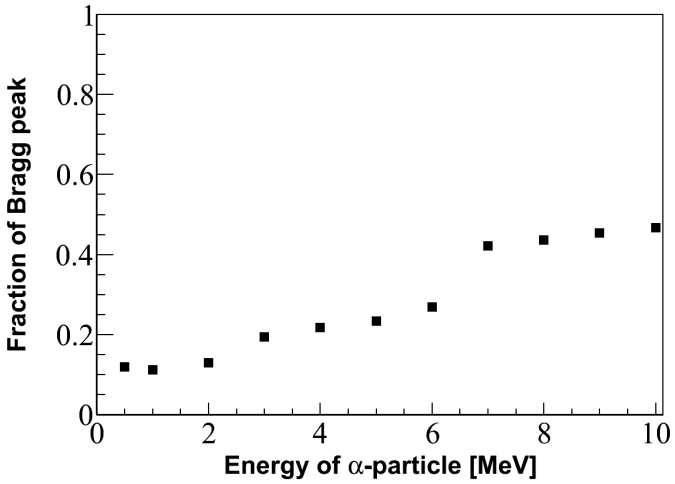

Figure 5.8: Fraction of the Bragg peak to be taken as the definition of the range in order to match the range given by SRIM.

$+90^\circ$ instead of -180° to $+180^\circ$ which is due to the conventions used during the analysis.

5.2 Definition of range

As stated in Chapter 4, we defined the range as the distance to 20% of the height of the Bragg peak. A study has been made to validate the definition of range taken as the distance of 20% of the height of the Bragg peak from the origin. α-particles of energy ranging from 0.5 MeV to 10 MeV have been considered. Then for each α-particle, the percentage of Bragg peak defined as range in SRIM [61] has been calculated in our experimental conditions. From Fig 5.8, it is clear that as the energy of the α-particles increases, the percentage of Bragg peak defined as range, converges to 50% of the height of the Bragg peak. Since in our case only low-energy recoil α-particles (below 6 MeV) are of interest, 20% of the height of the Bragg peak is taken as the range.

Furthermore, to the check this point, simulated events are considered at 0° ϕ angle, i.e., parallel to the cathode pad plane, where two-dimensional and three-dimensional ranges are the same (see Eqn. 4.8). Two different cases are considered:

i) 60° laboratory angle for 20 MeV excitation of ^{56}Ni. The calculated energy of the recoil

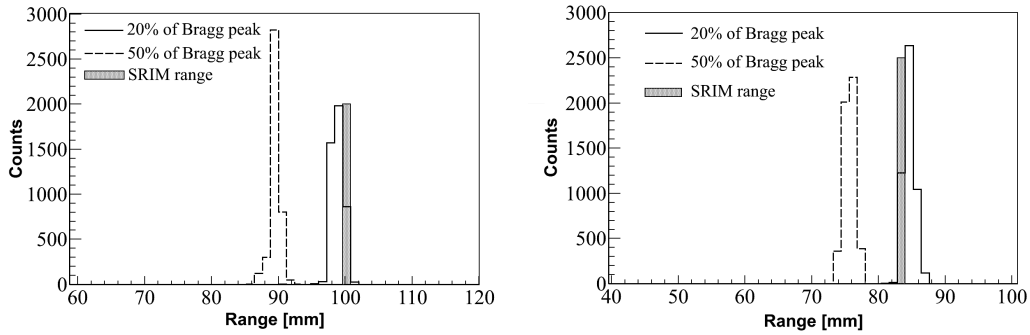

Figure 5.9: Definition of range; left panel: range of recoil α-particle at 60° laboratory angle for 20 MeV excitation energy of ^{56}Ni, right panel: range of recoil α-particle at 40° laboratory angle for 30 MeV excitation energy of ^{56}Ni. In both cases, the dashed histogram and solid histogram represent the range of the recoil α-particle which is defined as 50% and 20% of the height of the Bragg peak, respectively. The filled histogram represents the range obtained from SRIM.

α-particle in this case is 2.54 MeV. The calculated range of the α-particle with this energy is 99.6 mm.
ii) 40° laboratory angle for 30 MeV excitation of ^{56}Ni. The calculated energy of the recoil α-particle in this case is 2.2 MeV. The calculated range of the α-particle with this energy is 83.4 mm.

In both cases, the energy of the recoil α-particle is obtained from kinematical calculation with LISE++ [78]. Ranges of α-particles are obtained from SRIM [61] code calculated at our experimental conditions.

In both cases, 5000 events are simulated. In Fig. 5.9, the range of the recoil α-particle defined as 50% of the height of the Bragg peak from the two-dimensional charge projection is shown as the dashed histogram, whereas the range which is defined as 20% of the height of the Bragg peak from the two-dimensional charge projection is shown as the solid histogram (for the details of extraction of range from two-dimensional charge projection, see Sub-section 4.3.3.). The corresponding range given by SRIM is shown by the filled histogram. The range defined as 20% of the height of the Bragg peak from the two-dimensional charge projection is in agreement with the SRIM calculation.

Although the above method is good enough to test that 20% of the height of the Bragg peak matches with the SRIM calculation, however, we want to see what is the effect of this definition of the range of the recoil α-particle on the reconstructed excitation energy of ^{56}Ni.

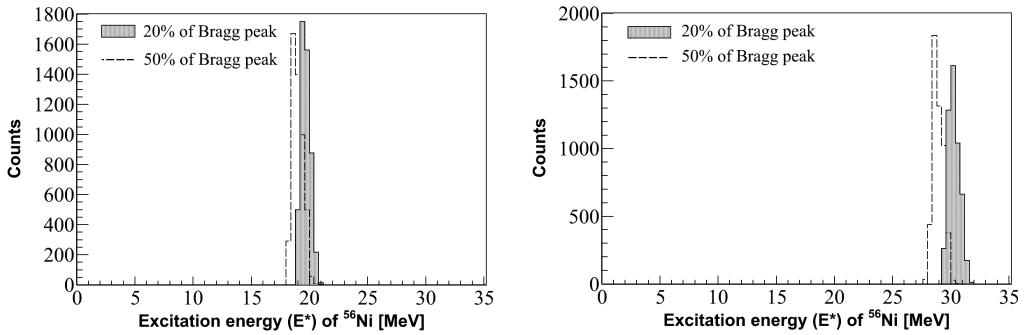

Figure 5.10: Reconstructed excitation energy; left panel: reconstruction of 20 MeV excitation energy of ^{56}Ni, right panel: reconstruction of 30 MeV excitation energy of ^{56}Ni. In both cases, the dashed histogram represents the range of the recoil α-particle taken as 50% of the height of the Bragg peak while the filled histogram represents the range of the recoil α-particle taken as 20% of the height of the Bragg peak.

From the kinematics calculation, one can determine the excitation energy of ^{56}Ni once the energy (or range) of the recoil α-particle is known. The reconstructed excitation energy is shown in Fig. 5.10 where the filled histogram shows the reconstructed excitation energy assuming the range to be 20% of the height of the Bragg peak while the dashed histogram shows the reconstructed excitation energy assuming the range to be 50% of the height of the Bragg peak. Since we are simulating events for 20 MeV and 30 MeV excitation energy of ^{56}Ni, the definition of range which is 20% of the height of the Bragg peak leads to better agreement between reconstructed excitation energy and actual excitation energy of ^{56}Ni than the definition of range of 50% of the height of the Bragg peak.

Finally, during our experiment we also had runs with an α-source (^{239}Pu; E_α = 5.2 MeV). In Fig. 5.11, the extracted energy of α-particles from the source is shown where the range is considered to be 20% of the height of the Bragg peak. The extracted energy is in agreement with the energy of the α-particles from the source itself.

Comparison of energy resolution obtained from range and charges on the pads

As stated in the previous chapter, the charge resolution of the cathode pads is poor. Therefore, energy of the ionizing particle is not extracted from these pads although their collected charges are proportional to the energy of the ionizing particle. To illustrate this point, recoil α-particles are considered at 60° laboratory angle and at 0° ϕ-angle for 20 MeV excitation

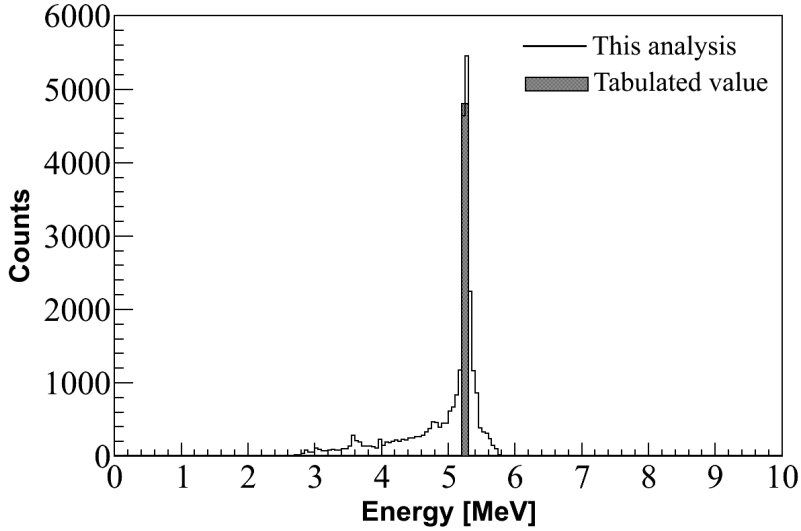

Figure 5.11: Reconstructed energy of the α-particle from ^{239}Pu source shown in black solid histogram. The filled histogram shows the tabulated value of energy of emitted α-particle from ^{239}Pu source [72].

energy of ^{56}Ni. Such an event is shown in Fig. 5.12.

The resolution of the extracted range from the two-dimensional charge projection is $\sim$2.1%. One should note again here that for 0° ϕ-angle, the two-dimensional and three-dimensional ranges are the same. Since the range and the energy of a particle are uniquely related, one can also deduce the energy-resolution which in this case is $\sim$1.9% which is obtained from range-energy relationship as shown in Fig. 4.25.

However, if we want to extract the energy of the ionizing particle from the charges on the pads, we first have to take into account how many pads are fired. In this case almost 60 pads are fired and since the relative charge-resolution of a pad is $\sim$2.3% (see Sub-section 4.2.1), for all 60 pads the total relative charge resolution will be $\sqrt{60} \times 2.3\% \sim 18\%$.

In summary, the energy of the ionizing particle is not deduced from the charges on the pads. Charges on the pads are only used to reconstruct the Bragg peak and in turn used to determine the range of the particle that stops inside MAYA.

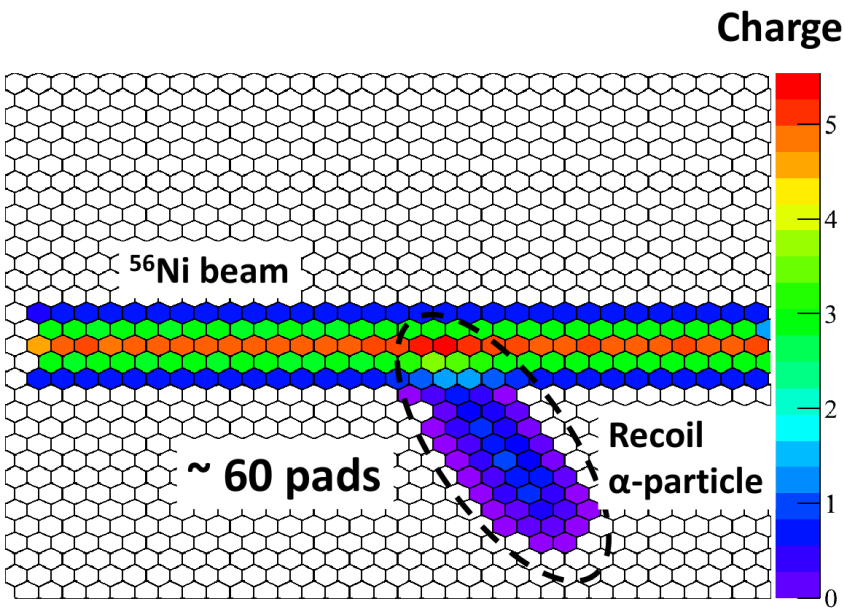

Figure 5.12: Simulated event at 20 MeV excitation energy of ^{56}Ni at 60° scattering angle and at 0° ϕ-angle.

5.3 Kinematics variables reconstruction uncertainties

From simulated events, it is possible to estimate the uncertainties involved in the reconstruction of CM scattering angle and excitation energy of ^{56}Ni. Since we have categorized tracks depending on the recoil two-dimensional track length (see Section 4.3), uncertainties in reconstructing kinematic variables have been calculated separately for long tracks and short tracks.

5.3.1 Errors in CM-angle reconstruction

The absolute error in CM-angle reconstruction ($\triangle\theta_{CM}$) is given as:

$$\triangle\,\theta_{CM} = \theta_{CM,Sim} - \theta_{CM,Rec} \tag{5.2}$$

where $\theta_{CM,Sim}$ is the given CM angle and $\theta_{CM,Rec}$ is the reconstructed CM angle. In Fig. 5.13, the absolute error in the CM-angle reconstruction is shown as a function of given CM angle

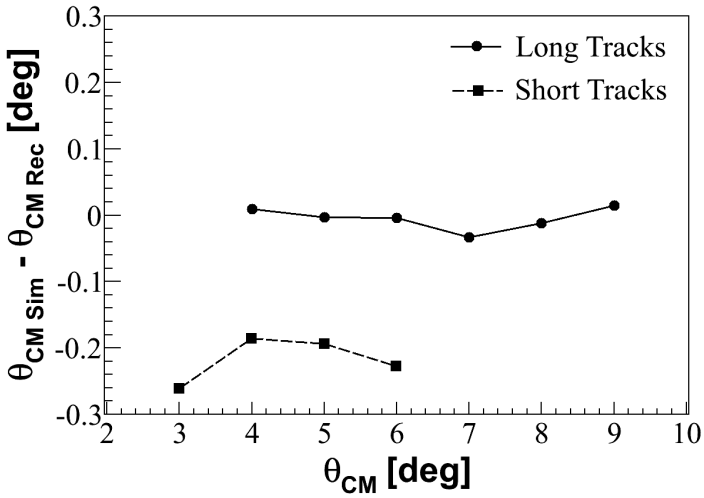

Figure 5.13: Errors in CM angle reconstruction for 20 MeV excitation energy of ^{56}Ni. Solid line shows the errors for long two-dimensional tracks while the dashed line shows the errors for short two-dimensional tracks.

for 20 MeV excitation energy of ^{56}Ni.

The errors in CM-angle reconstruction for events having long two-dimensional tracks are less than those for events having short two-dimensional tracks. This reflects the fact that if the track is closer to the beam, it is more difficult to reconstruct the trajectory and consequently the scattering angle. Even for short tracks, the absolute error in CM angle is less than 0.3°. Figure 5.13 also shows the angular domains covered by our definitions of long and short tracks.

5.3.2 Uncertainties in excitation-energy reconstruction

Uncertainties in scattering-angle reconstruction also induce uncertainties in reconstruction of excitation energy of ^{56}Ni. The absolute error for excitation energy reconstruction ($\triangle E^*_{^{56}Ni}$) is given as:

$$\triangle E^*_{^{56}Ni} = E^*_{^{56}Ni,Sim} - E^*_{^{56}Ni,Rec} \tag{5.3}$$

where $E^*_{^{56}Ni,Sim}$ is the given excitation energy and $E^*_{^{56}Ni,Rec}$ is the reconstructed excitation

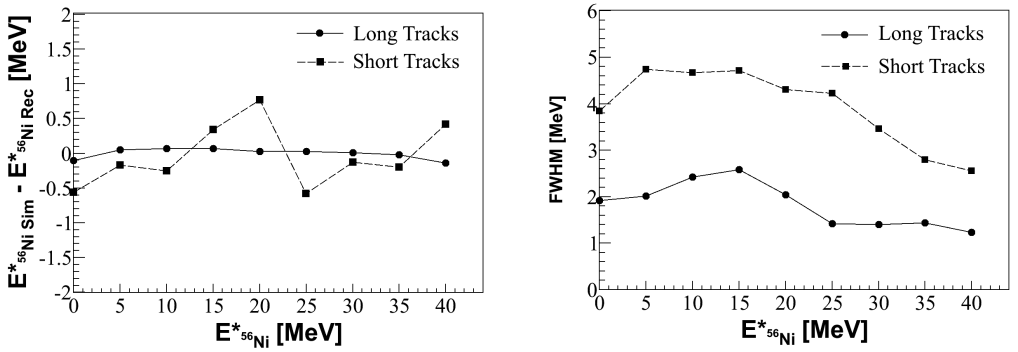

Figure 5.14: Left panel: uncertainty in excitation-energy reconstruction, right panel: FWHM of the Gaussian fit for the reconstructed excitation energy. In both cases, the solid line represents the tracks having long two-dimensional track length and the dashed line represents the tracks having short two-dimensional track length.

energy of ^{56}Ni. In Fig. 5.14, the absolute errors for the centroids of the reconstructed excitation energies are shown (left panel). The FWHM of the Gaussian fits for the reconstructed excitation energies are also shown (right panel of Fig. 5.14).

The excitation-energy reconstruction for events having short two-dimensional tracks has errors larger than those for events having long two-dimensional tracks. For the short tracks, the FWHM of the Gaussian fit of the reconstructed excitation energy is also larger than the long tracks. However, in both cases the uncertainty for the centroid value of the reconstructed excitation energy is on the average less than 0.5 MeV.

5.4 Excitation energy versus vertex of interaction

Since the limited volume of MAYA generates a cut in the phase space, events reconstruction is not uniform for all excitation energy of ^{56}Ni ranging from 0 MeV to 50 MeV. As the excitation energy of ^{56}Ni increases, the recoil α-particle energy also increases (see the right panel of Fig. 5.1), which in turn increases the chance for the recoil particle to punch through the MAYA volume. The higher the excitation energy of ^{56}Ni is, the lower the acceptance is and in turn the smaller the effective target thickness is.

In Fig. 5.15, the reconstructed excitation energy is plotted as a function of the reconstructed interaction vertex. This is shown for both the experimental data (left panel) and simulated data (right panel). Elastic scattering (i.e., 0 MeV excitation) off ^{56}Ni can be reconstructed

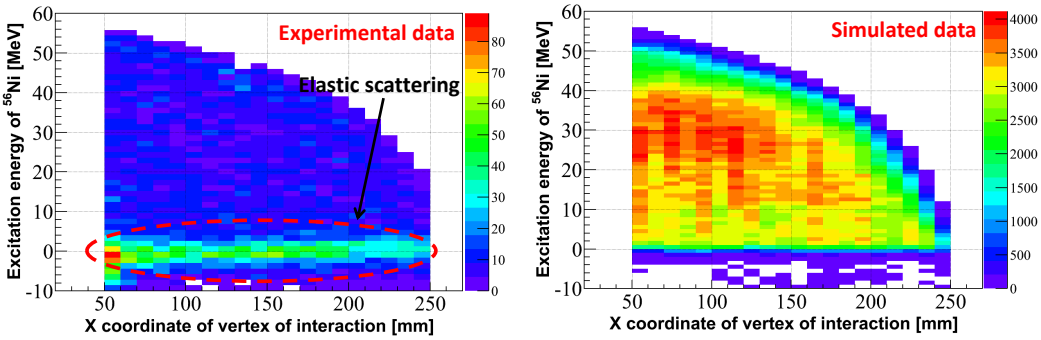

Figure 5.15: Plot of excitation energy as a function of the x coordinate of the interaction vertex for the experimental data (left panel) and simulated data (right panel).

throughout the whole accessible region in MAYA. But as the excitation energy increases the acceptance of the detector decreases. The sharp cut at 50 mm for the vertex of interaction reflects the fact that we are considering events having a vertex of interaction above 50 mm to avoid reactions from the beam-entrance window (see Fig. 4.28). The same lower limit has also been put for simulated events. Eventually the upper limit for the vertex of interaction is also the same as the experimental data which is 250 mm. During the efficiency correction of the experimental data, the effective target thickness has to be taken into account because it also affects the cross-section calculation (see Eqn.6.2).

5.5 Efficiency and acceptance

Figure 5.16 shows the efficiency (geometric and reconstruction) plot of reconstructed excitation energy of ^{56}Ni versus θ_{CM} scattering angle. In this analysis, the bin size for excitation energy of ^{56}Ni is taken to be 1 MeV and that for CM angle to be 1° and the efficiency correction is performed bin-by-bin. For reconstructing the simulated data we applied the same geometrical cuts as stated for data in the Sub-section 4.4.3.

Below 20 MeV it is difficult to reconstruct the events below 3° CM angle since the recoil α-particles have very low-energy (< 0.6 MeV). At this energy, the α-particles barely come out of the beam region, making it hard to distinguish between the beam and the recoil particle. However, as the excitation energy increases, the energy of the recoil α-particles also increases allowing them to go further out of the beam region. At all energies, however,

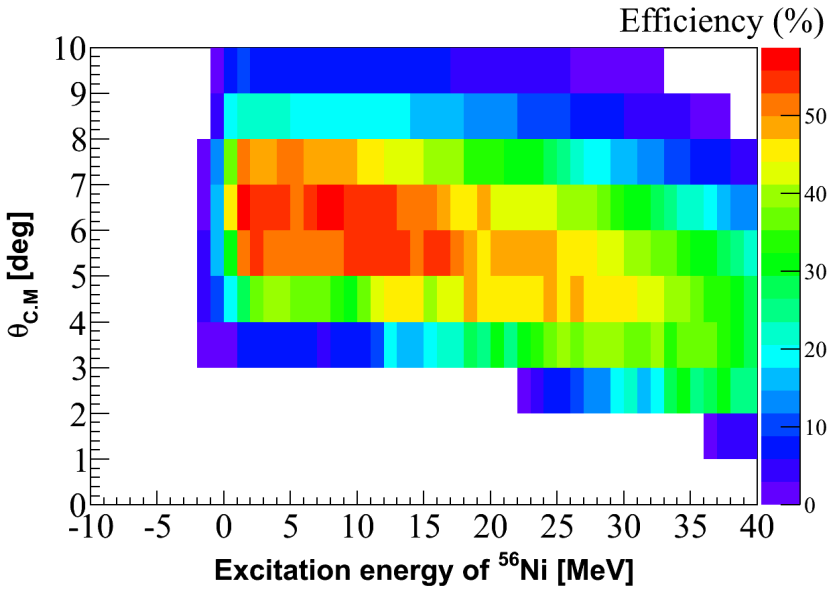

Figure 5.16: Reconstruction efficiency combined with geometrical acceptances as a function of excitation energy of ^{56}Ni versus θ_{CM}.

it is impossible to detect recoil α-particles below 2° CM angle for excitation energies below 35 MeV. Above 8° CM angle, recoil α-particles have high energies and, therefore, punch through MAYA. Although events at high CM angles can be detected if the recoil α-particles have larger ϕ angles, they have low efficiency due to the detector acceptance as the particles have higher energies enabling them to punch through the detector volume.

Chapter 6

Results and discussion

In this chapter the results of the measurements for the elastic scattering and the giant resonances states of ^{56}Ni will be presented. The experimental data are processed according to the methods described in Chapter 4. In a second step, the angular distributions will be compared with the predictions made within the DWBA approximation. The angular distributions described in this chapter correspond to ^{56}Ni (α, α) ^{56}Ni reaction (elastic scattering) and ^{56}Ni (α, α') ^{56}Ni* (inelastic scattering).

6.1 Events in the laboratory frame

The ^{56}Ni beam selection and the geometrical and event-reconstruction selection conditions for the recoil α-particles are detailed in Chapter 4. The kinetic energies of the recoil α-particles are plotted versus their laboratory scattering angles (θ) in Fig. 6.1. The solid lines represent the LISE++ kinematics calculations for 0 MeV (elastic scattering), 2.7 MeV (first excited state), 16 MeV, 20 MeV and 30 MeV excitation energy of ^{56}Ni.

From Fig. 6.1, it is clear that the high density of counts around the angle of 90° corresponds to the elastic scattering and is much larger than the inelastic ones. From this figure, it can also be seen that recoil α-particles having energies greater than $\sim$600 keV can be detected which sets the detection threshold at 600 keV. It is also to be noted here that due to the uncertainty in the determination of the laboratory scattering angle, the extension of the elastic scattering region goes down to around 83° in the laboratory frame. This is the region where the low-lying excited states of ^{56}Ni are situated, e.g., the first-excited state (2^+ state) of ^{56}Ni, which has an energy of 2.7 MeV [72]. However, the experimental resolution is not good

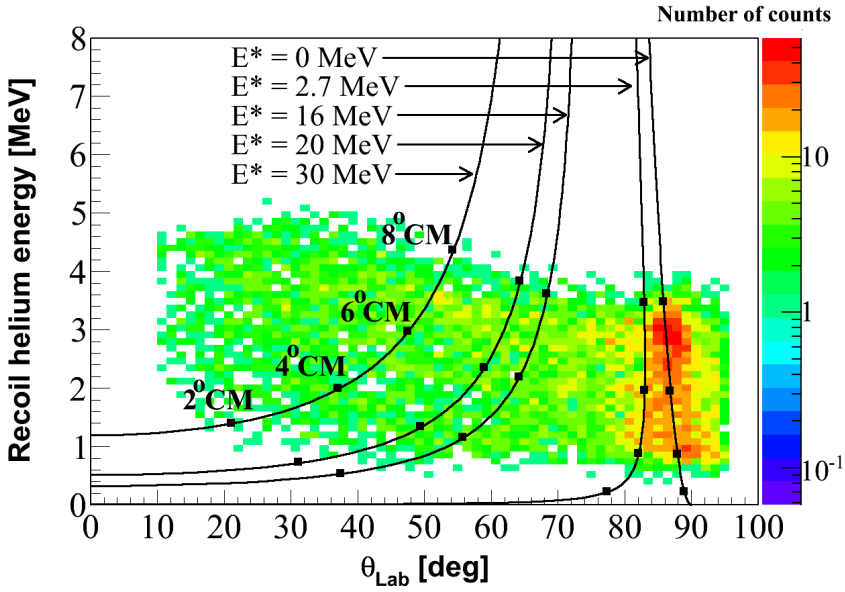

Figure 6.1: Two-dimensional plot of kinetic energies versus scattering angles reconstructed for the recoil α-particles. The solid lines represent the LISE++ kinematics calculations obtained for 0 MeV(elastic scattering), 2.7 MeV (first excited state), 16 MeV, 20 MeV and 30 MeV excitation energy of ^{56}Ni. Several CM angles are shown on the kinematics lines.

enough to separate these states. The events due to elastic scattering and having energies below 1 MeV have worse resolution as compared to events having energies greater than 1 MeV. These are due to events having short recoil tracks which are difficult to reconstruct as they are closer to the beam-passage region. The CM angles from 2° to 8°, which define the accessible region for certain excitation energies in the phase-space limited MAYA detector, are also shown. One can also see that, it is impossible to reconstruct events at 2° CM angle because the recoil α-particles have very low energies and/or they barely come out of the beam region. Events around 8° CM angle are also difficult to reconstruct as they punch through the MAYA volume due to their high energies.

6.1.1 Excitation energy spectrum of ^{56}Ni

Once the kinetic energies and the scattering angles of recoil α-particles are known in the laboratory frame, it is possible to calculate the excitation energy of ^{56}Ni for each event from the two-body kinematics. From the conservation of energy and momentum, the excitation

energy of ^{56}Ni ($E^*_{^{56}Ni}$) can be written as:

$$E^*_{^{56}Ni} = \sqrt{(E_{inc} + E_{target} - E_{recoil})^2 - (pc)^2} - m_{Ni} \tag{6.1}$$

where E_{inc} is the total energy of the incident ^{56}Ni beam particle, E_{target} is the rest-mass energy of the He target, E_{recoil} is the total energy of the recoil α-particle, p is the momentum of ^{56}Ni after scattering and m_{Ni} is the rest-mass energy of ^{56}Ni. In Fig. 6.2, the reconstructed excitation energy of ^{56}Ni is shown before (left panel) and after (right panel) efficiency correction.

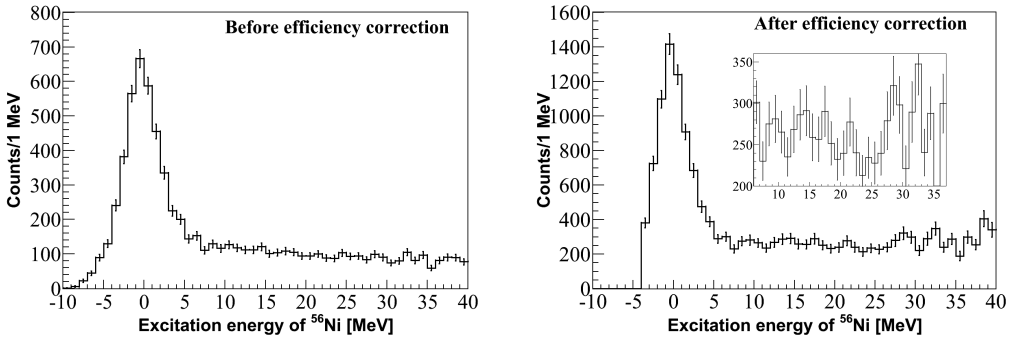

Figure 6.2: Excitation energy of ^{56}Ni. Left panel: before efficiency correction, right panel: after efficiency correction. The inset in the right panel shows the zoom of the efficiency-corrected spectrum from 8 MeV to 35 MeV.

The FWHM of the elastic-scattering peak is $\sim$4.5 MeV. It should be noted that the elastic-scattering peak is broadened by the presence of the low-lying excited states. The efficiency-corrected spectrum shows some structures in the region of the giant resonances (see the inset in the right panel of Fig. 6.2). However, for a clearer identification of these states, one has to observe the evolution of the excitation energy as a function of the scattering angle. This will also lead to the reconstruction of the angular distribution and a complete understanding of the giant resonances.

6.2 Angular distribution

6.2.1 Normalization

For a given excitation energy interval, the differential cross section for a given CM angle can be expressed as:

$$\frac{d\sigma}{d\Omega}(\theta_{CM}) = \frac{dN(\theta_{CM})}{2\pi\, sin(\theta_{CM}) d\theta_{CM}} \times \frac{1}{\epsilon\, N_{target}\, N_{beam}\, l} \tag{6.2}$$

where,

- $dN(\theta_{CM})$ is the number of events detected at θ_{CM} angle for a given energy interval dE.
- ϵ is the efficiency parameter and is calculated through the procedure described in the previous chapter.
- N_{target} is the number of target particles in unit volume, i.e., target-particle density. The target-particle density for 95% He and 5% CF_4 at 500 mbar pressure is $1.15\times10^{19}/\mathrm{cm}^3$.
- N_{beam} is the number of incoming beam particles. Since in our experiment, the diamond detector which acts as a beam stopper was not working, we could not extract any information from it. However, since wire#17 is parallel to the beam, the scaler, counting the frequency of events for wire#17, is used to count the number of incoming beam particles, taking into account the dead time. Furthermore, the incoming beam particles can be identified by looking into the time-of-flight of particles between the Micro-Channel-Plate-Analyzer (MCPA) and the plastic scintillator detector (see Fig. 3.3). It is clear from Fig. 4.26, that the peak in between channel number 4300 and 5800 corresponds to ^{56}Ni. By taking appropriate ratios of the ^{56}Ni peak and the whole spectrum, the number of incoming beam particles can further be corrected.
- l is the length of the active area in MAYA. This corresponds to the selection condition for vertex of interaction (see Fig. 4.28). Furthermore, the length of the active area varies depending on the extracted excitation energy of ^{56}Ni (see Fig. 5.15).

To obtain the efficiency correction, simulations have been performed and described in Chapter 5. The efficiency correction is performed bin-by-bin with a binning size in θ_{CM} of 1° and in excitation energy of 1 MeV. Although our main aim is to obtain the angular distributions of structures in the giant-resonance region in ^{56}Ni, efforts are also put to obtain the elastic-scattering cross section. Information on the elastic-scattering cross section can be useful to obtain a proper normalization which is necessary for the absolute cross sections of the giant-

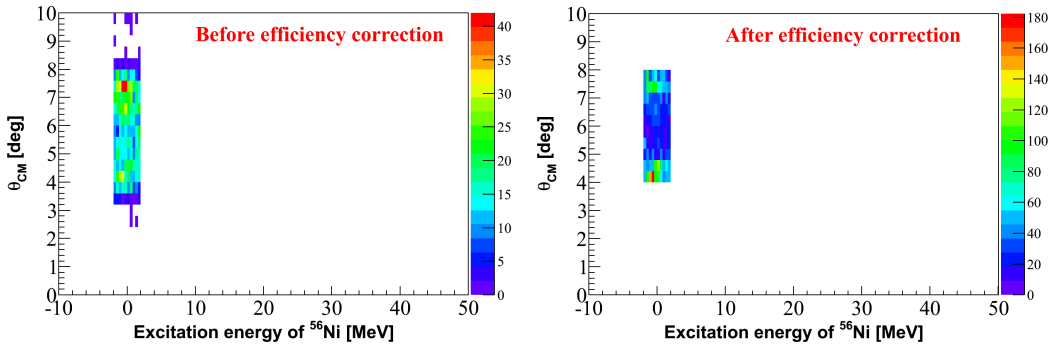

Figure 6.3: Efficiency plot for elastic scattering of ^{56}Ni. Left panel: before efficiency correction, right panel: after efficiency correction.

resonance states of ^{56}Ni. This chapter is further divided into two parts: elastic scattering of ^{56}Ni and inelastic scattering of ^{56}Ni.

6.3 Elastic scattering of ^{56}Ni

Elastic scattering is the most favorable process in most of the scattering experiments. Elastic scattering describes a process where the total kinetic energy of the system is conserved. Since the first-excited state of ^{56}Ni is at 2.7 MeV, for analysis of elastic scattering, a cut has been applied to the excitation-energy spectrum of ^{56}Ni which extends from -2 MeV to 2 MeV taking into account the experimental resolution. Due to favorable statistics, only for the elastic scattering analysis, the bin size for θ_{CM} has been decreased to 0.4° and the bin size for excitation energy to 0.4 MeV. In Fig. 6.3, the θ_{CM} angle versus the excitation energy is shown for elastic scattering before (left panel) and after (right panel) the efficiency correction. A threshold of efficiency correction greater than 10% has been considered in the present analysis. Therefore, although there are events below 4° and above 8° CM angle before efficiency correction (see the left panel of Fig. 6.3), after efficiency correction (see the right panel of Fig. 6.3) those events are not considered because of efficiency lower than 10%.

From the efficiency-corrected plot, data are projected onto the CM axis and Eqn. 6.2 was used to obtain the differential cross section. In Fig. 6.4, the angular distribution for elastic scattering of α-particles from ^{56}Ni is shown. The theoretical calculations have been performed using the CHUCK3 code [59] and the parameters used for optical potential are listed

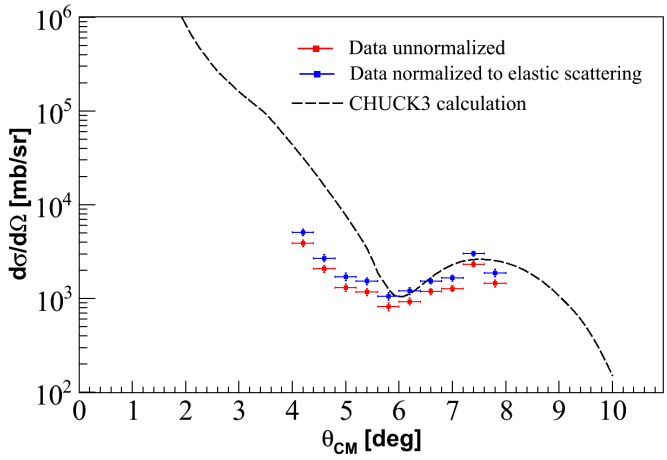

Figure 6.4: Cross section for elastic α-particle scattering off ^{56}Ni. The dashed line represents the optical-model calculations performed with the CHUCK3 code. The red points show the obtained elastic-scattering cross section using Eqn. 6.2. Data, multiplied by a normalization factor of 1.3, are shown as blue points (see text).

in Chapter 2.

In Fig. 6.4, the obtained elastic-scattering angular distribution using Eqn. 6.2 is shown by the red points. The black dashed curve represents the optical-model calculations performed with the CHUCK3 code. To obtain absolute cross sections for the giant resonances of ^{56}Ni, we have multiplied the elastic-scattering cross section data by a factor 1.3 to match with the theoretical prediction for the data points above 6° CM angle which correspond to events having long tracks. These data points, multiplied by the factor, are shown as blue points.

To obtain the data points (shown in red) in Fig. 6.4 , efficiency factors between 2 to 4 have been applied to account for track-reconstruction inefficiencies, in particular for short tracks as well as acceptance corrections for both track types. From Fig. 6.4, it is clear that below 5° CM angle, there is a discrepancy between the optical-model calculations and experimental data. It is due to the fact that for elastic scattering below 5° CM angle, the events correspond to the short recoil tracks whose reconstructions are more difficult as they are closer to the beam-passage region. Furthermore, as can be seen from Fig. 6.1 the events around 4° CM angle for the elastic scattering have energies below 1 MeV. The error bars are calculated taking into account only the statistical fluctuations in the data and errors in the efficiency correction. Above 6° CM angle, there is a good agreement with the optical-model calcula-

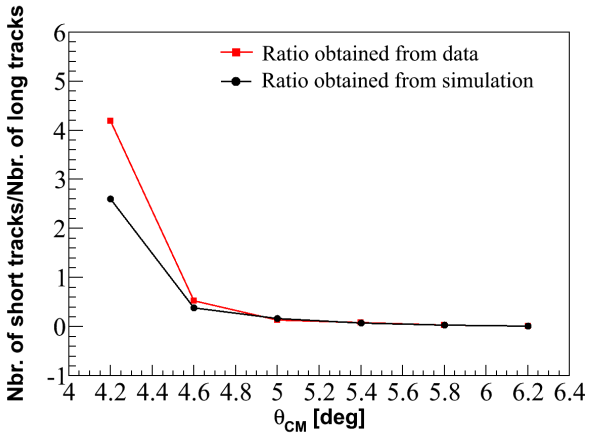

Figure 6.5: Ratio of number of short and long recoil α-particle tracks for elastic scattering.

tion as this angular region corresponds to the long recoil α-particle tracks. There are no data below 4° CM angle and above 8° CM angle due to the acceptance of the detector.

In Fig. 6.5, the ratio of the numbers of short and long tracks is shown versus the accessible CM angle for elastic scattering. Above 6.2° CM angle, there are only long recoil tracks. The ratio is shown for both the simulated events and the data. From this figure, it is clear that the ratio of the numbers of short and long tracks for simulation are comparable with the data. Therefore, the efficiency correction obtained from the simulation without distinguishing long and short tracks is reliable.

6.4 Inelastic scattering of ^{56}Ni: Giant resonances

After track and scattering-angle reconstruction and applying the same filter as mentioned in Chapter 4, the events are plotted as a function of reconstructed excitation energy of ^{56}Ni and CM angle. They are shown in Fig. 6.6 before (left panel) and after (right panel) the efficiency correction. One has to note here that in the analysis of inelastic scattering, the bin size for θ_{CM} axis has been changed to 1° and that of the excitation-energy axis to 1 MeV.

From the efficiency-corrected histogram (right panel in Fig. 6.6), it is possible to study the angular distributions for the giant resonances in two different ways:

- The Gaussian peak-fitting method, where the events are considered for a given CM an-

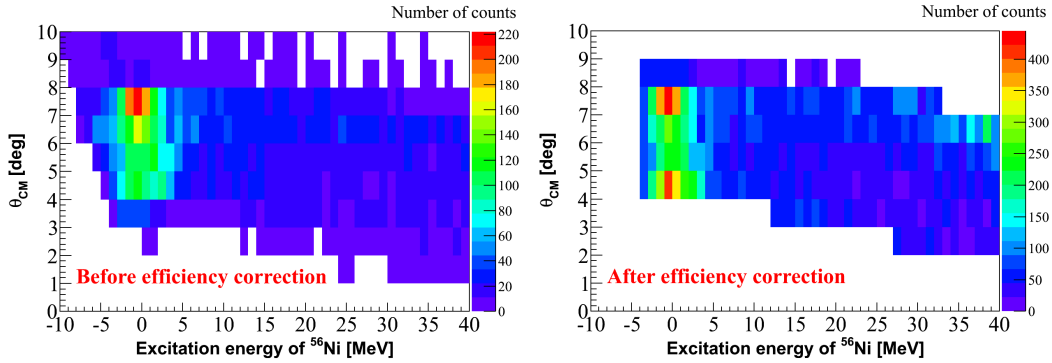

Figure 6.6: Efficiency plot for all events (elastic and inelastic scattering of ^{56}Ni). Left figure: before efficiency correction, right figure: after efficiency correction. The bin size in θ_{CM} axis is 1° and that in excitation energy axis is 1 MeV. Note that the binning sizes are larger than that are used for elastic scattering as shown in Fig. 6.3.

gle interval and data are projected on the excitation energy axis. The peaks in the excitation energy spectrum are then fitted with Gaussian functions. The areas of the peaks then lead to the cross sections.

- The multipole-decomposition analysis (MDA), where the events are considered for a given excitation-energy interval and data are projected on the axis of the CM angle. The angular distributions of events for each excitation-energy interval are fitted with linear combinations of theoretical angular distributions for the lowest four multipoles (L = 0, 1, 2 & 3). However, before MDA analysis is performed, a background is subtracted from the excitation-energy spectrum obtained from the Gaussian method.

6.4.1 Gaussian peak-fitting method for ^{56}Ni(α, α')^{56}Ni* reaction

The excitation-energy spectra have been obtained for several CM angles starting from 3.5° CM angle to 8.5° CM angle. Below 3° CM angle, it is impossible to reconstruct events as the recoil particles have very low energies and they barely come out of the beam-passage region. Above 9°, the recoil particles have high energies and they punch through the MAYA volume (see Fig. 6.6). The six excitation-energy spectra were fitted with Gaussian peaks and a continuous background. Fitting of the excitation-energy spectra for all CM angle intervals was limited to a region between 5 MeV and 35 MeV. Estimation of the background shape has been done in two different ways as described in the following.

Method 1: Fixing of the background shape manually

The shape of the background is fixed manually through the minima of the giant-resonance region. The shape of the background is chosen in a way such that it incorporates the extension of the elastic-scattering peak and few low-lying excited states into the inelastic-scattering region above 5 MeV. After fixing the shape of the background, it is then parameterized with a polynomial of order 4 (except for spectra obtained at 3.5° and 8.5° CM angles where a polynomial of order 2 has been taken into account). After parameterization with the polynomial, another scaling parameter has been added to the polynomial. While fitting the spectra with Gaussian functions along with the background, the shape of the "background" polynomial is kept fixed while the extra added parameter is kept free which can eventually determine the height of the background from the total fit (Gaussian peaks and background).

The width of a Gaussian peak is kept free for a CM angle where the corresponding peak is prominent. After obtaining the width parameter, it is kept fixed for other CM angles where the corresponding peak height is not pronounced. The centroid of a peak is also kept free within a window of 2 MeV. This procedure has been applied for all peaks under consideration. However, for the first peak around 8.7 MeV, the width has been fixed to the width obtained from the interpolation of the FWHM for the long tracks as can been seen from Fig. 5.14. In Fig. 6.7, the fitted excitation-energy spectra are shown for CM angles 3.5° to 8.5°. For all CM angles shown in Fig. 6.7, the green dashed line is the background which is fixed manually. The blue dashed line is the parameterized background which is practically the same as the green-dashed line. An extra parameter is added to this parameterized background and is kept free for the total fit. The green solid line shows the final background obtained from the total fit. See the legend in the figure to identify various peaks for different CM angles.

Method 2: Background shape obtained from fitting of excitation-energy spectra assuming no giant-resonance structures

In this method, the background shape is not fixed manually but with a polynomial fit of order 4 (expect for spectra obtained at 3.5° and 8.5° CM angles where a polynomial of order 2 has been taken into account) to the excitation-energy spectra assuming that there are no giant-resonance structures. After this fit, the background shape is kept fixed and then another parameter is added to this polynomial. This extra additive parameter is kept free during the total fit of the excitation energy spectra with Gaussian peaks. In the same way as

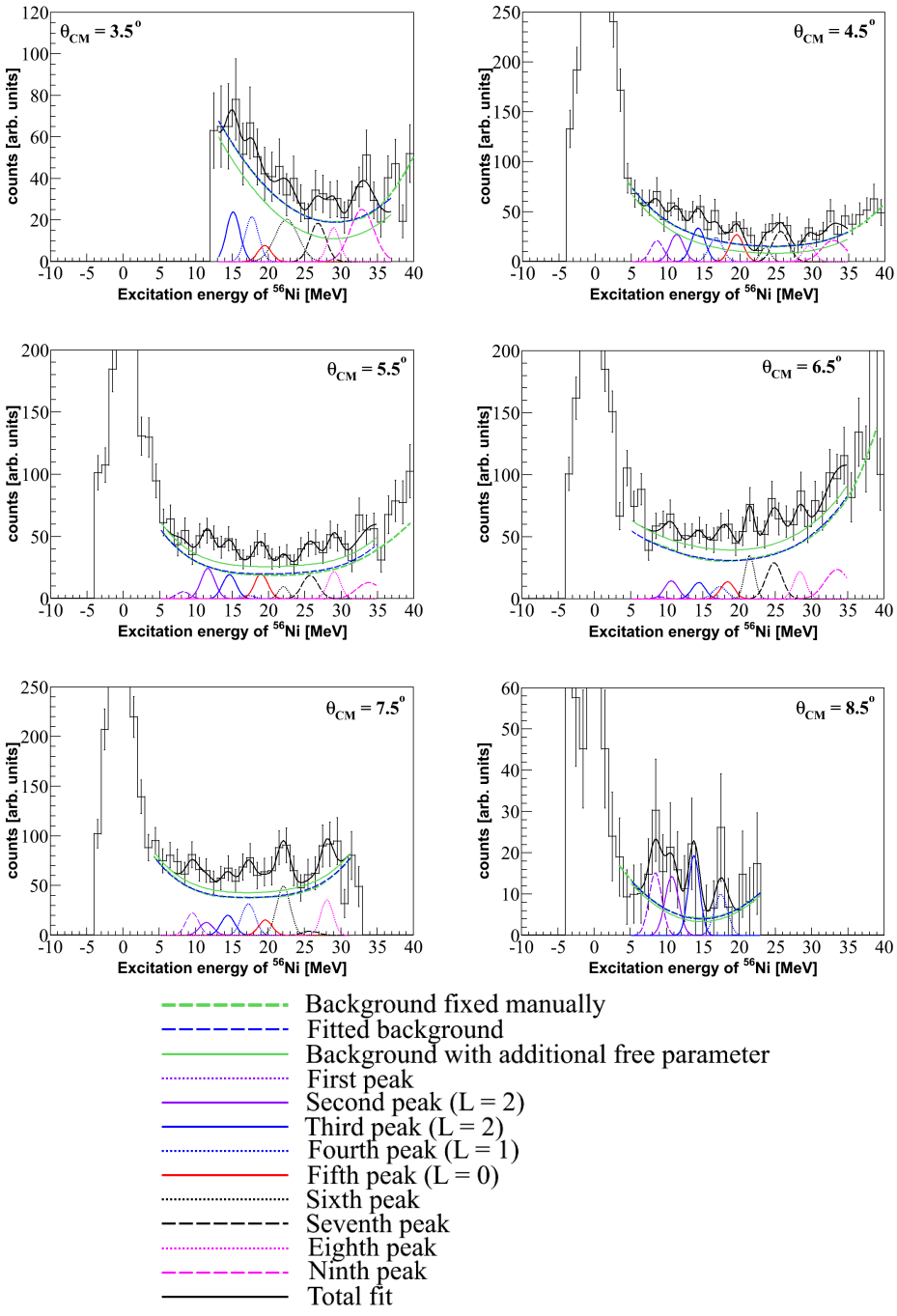

Figure 6.7: Excitation-energy spectra for different CM angles. The shapes of the backgrounds have been fixed manually (see text).

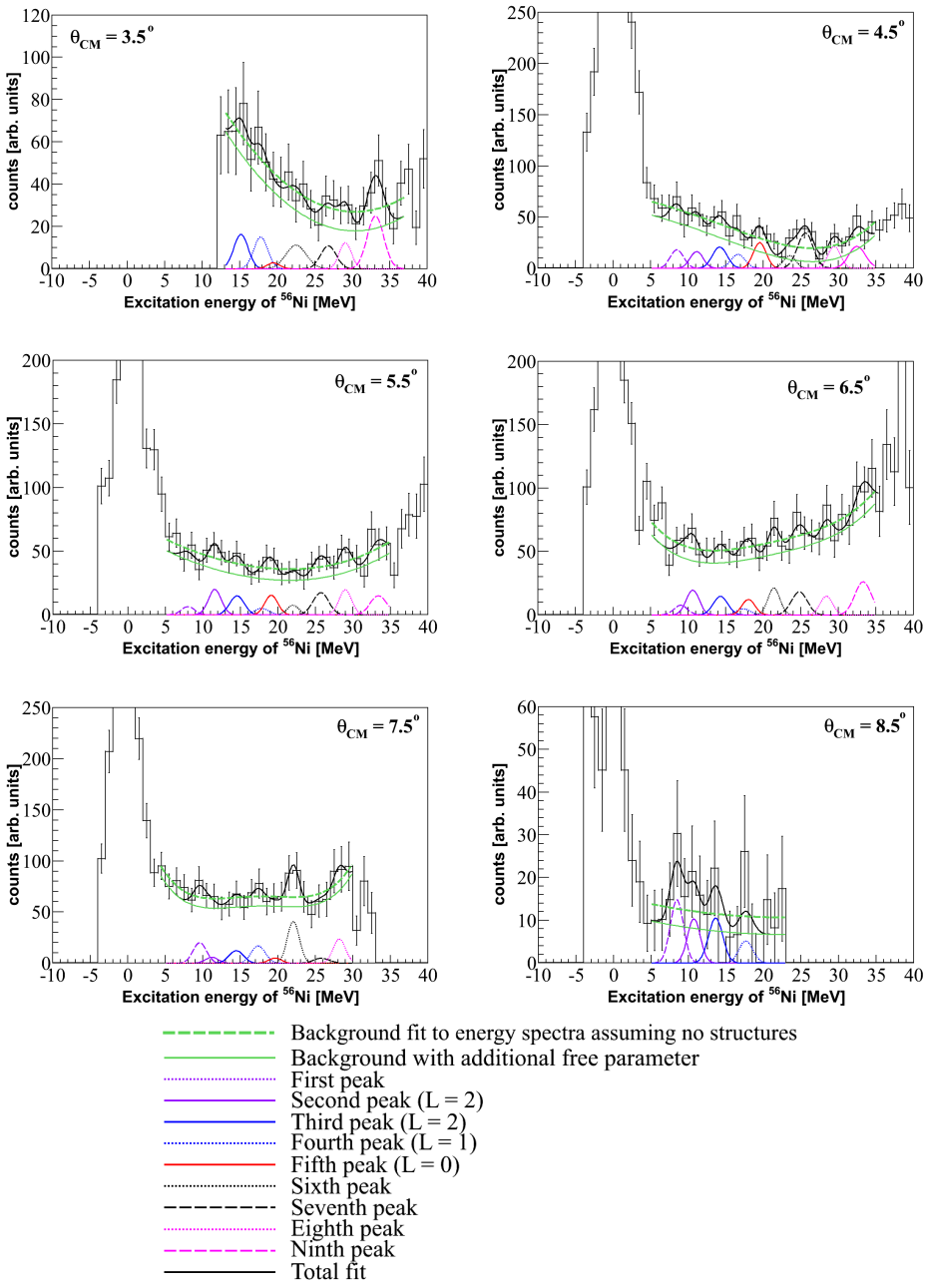

Figure 6.8: Excitation-energy spectra for different CM angles. The shapes of the backgrounds have been obtained from the fitting of the spectra assuming no structures of giant resonances (see text).

described above, the width of a Gaussian peak is kept free for a CM angle where a peak is prominent and is kept fixed at the obtained value for all other CM angles where the corresponding peak height is not pronounced and the centroid parameters of the peaks are kept free within a window of 2 MeV. In Fig. 6.8, the fitted excitation-energy spectra are shown for CM angles 3.5° to 8.5°. For all CM angles shown in Fig. 6.8, the green dashed line is the fitted background on the excitation energy spectra considering that there are no giant-resonance structures. The green solid line shows the final background obtained from the total fit. See the legend in the figure to identify the peaks for different CM angles.

From the fits, the centroid and FWHM of each Gaussian peak are obtained for each CM angle. In both methods of determining the background shape, the reduced χ^2 ranges from 0.5 to 1.5. The values of the centroid and FWHM for each peak are averaged over for all CM angles. These averaged values of the centroid and FWHM for each peak, obtained from the two different methods of fixing the shape of the background, are listed in Table 6.1.

	Centroid		**FWHM**	
	Method 1	Method 2	Method 1	Method 2
Peak 1	8.7±0.8 MeV	8.7±0.7 MeV	2.1 MeV	2.1 MeV
Peak 2 (L = 2)	11.1±0.4 MeV	11.0±0.5 MeV	2.2±0.8 MeV	2.0±0.3 MeV
Peak 3 (L = 2)	14.4±0.5 MeV	14.4±0.5 MeV	2.0±1.4 MeV	2.2±0.2 MeV
Peak 4 (L = 1)	17.3±0.7 MeV	17.4±0.7 MeV	2.2±0.6 MeV	2.2±0.6 MeV
Peak 5 (L = 0)	19.2±0.6 MeV	19.1±0.5 MeV	2.2±1.1 MeV	2.0±0.3 MeV
Peak 6	22.3±0.8 MeV	22.3±1.0 MeV	2.5±1.1 MeV	2.5±1.4 MeV
Peak 7	25.7±0.5 MeV	25.7±0.5 MeV	2.6±1.4 MeV	2.4±1.3 MeV
Peak 8	28.8±0.9 MeV	28.8±0.7 MeV	2.0±0.9 MeV	1.9±1.1 MeV
Peak 9	33.3±1.2 MeV	33.1±0.7 MeV	3.9±2.4 MeV	2.6±1.3 MeV

Table 6.1: Centroids and FWHM of the fitted peaks with two different methods of background-shape determination.

From Table 6.1, it is clear that there is not much difference (at least within the error bars) in the centroid positions and FWHM for the fitted peaks obtained from the two different methods of determining the shape of the background. For cross-section calculation, area of the Gaussian peak under consideration is calculated for each CM angle. After proper normalization as described in Eqn. 6.2 and also using the normalization factor of 1.3 obtained from the elastic scattering angular distribution, it is possible to reconstruct the angular distribution of the peaks under consideration. Figure 6.9 shows the angular distributions of

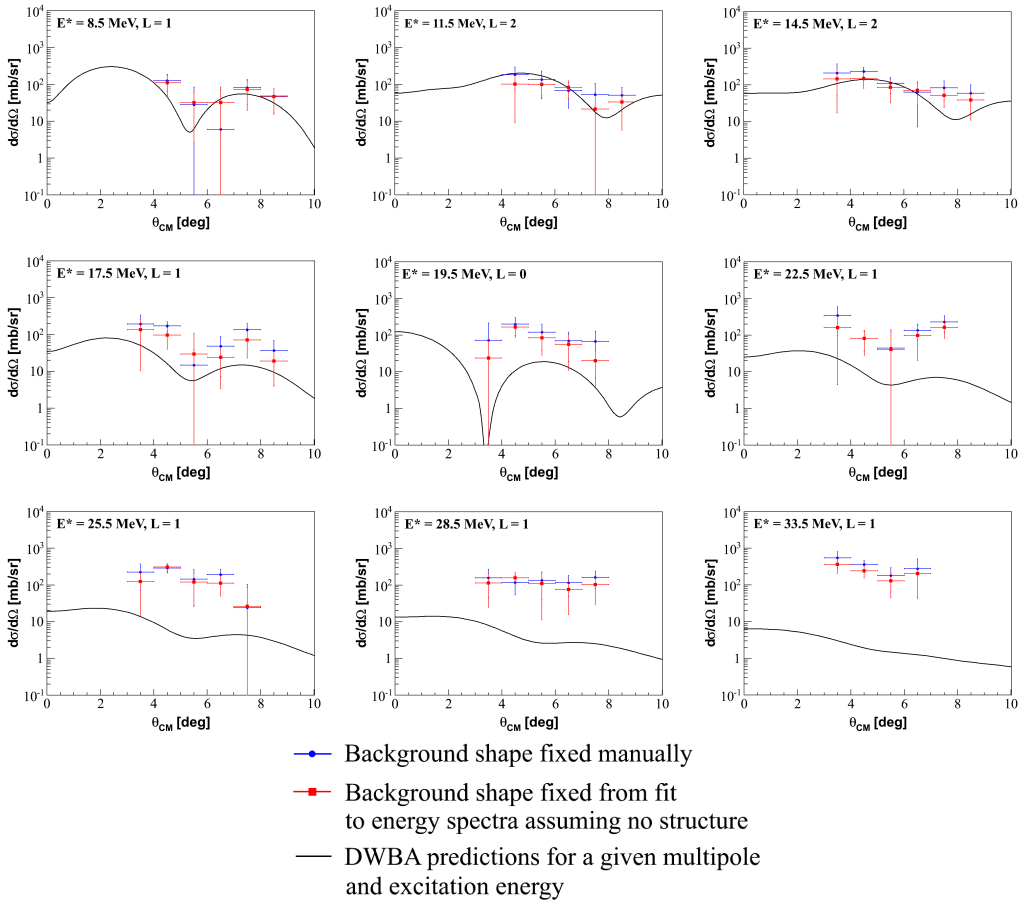

Figure 6.9: Angular distributions of different Gaussian peaks corresponding to different excitation energies. The dashed lines are DWBA predictions for the given excitation energy and multipole calculated with the CHUCK3 code. The parameters for the optical potential are given in Chapter2.

all fitted peaks in the Gaussian peak-fitting method. It is to be noted here again that for cross-section calculations, the proper lengths of the active area of MAYA have been considered for each peak according to the energy of the outgoing particle (see Section 5.4). For error calculations, the error of the free parameter of the background has also been taken into account for each CM angle. The theoretical differential cross sections were calculated within the DWBA framework using the CHUCK3 code. The parameters used for the optical potential are listed in Chapter 2. In theoretical calculations, it has been assumed that there is 100% exhaustion of the energy-weighted sum rule (EWSR). In Fig. 6.9, for a given excitation

energy a multipolarity is taken which is the best fit for the obtained angular distribution for that excitation energy. It is to be noted here that instead of an additive extra parameter in determining the height of the background, a multiplicative parameter has also been considered for the background. The results are consistent with the results mentioned here within the error bars. From Fig. 6.9, it can be seen that below 23 MeV, the angular distributions are similar to the corresponding theoretical calculations. However, for excitation energies higher than 23 MeV, multipoles other than the $L = 1$ mode start contributing. This will be clarified by MDA analysis in the following.

6.4.2 Multipole-decomposition analysis (MDA) for ^{56}Ni(α, α')^{56}Ni* reaction

From the Gaussian peak-fitting method, it is clear that the cross sections of different peaks obtained taking the shape of the background from the second method are systematically smaller (except for one data point for the $L = 1$ and $L = 2$ modes) than those from the first method (see Fig. 6.9). As seen from the figure, the data points are generally higher than the theoretical curves (which exhausts 100% of the EWSR) and therefore, for MDA analysis only the background shape, which is obtained from the fitting of the excitation-energy spectrum assuming no structures, is considered. Furthermore, due to low statistics, instead of 1 MeV bin, 2 MeV bin size in the excitation energy has been considered. After background subtraction, the angular distribution for each 2 MeV excitation-energy interval is obtained from the efficiency-corrected data using Eqn. 6.2. The obtained angular distributions for each energy interval are also normalized with a factor of 1.3 obtained from the elastic-scattering angular distribution. The obtained angular distribution for each energy interval, is then fitted with the following function:

$$\left.\frac{d^2\sigma}{d\Omega\, dE}(\theta_{CM}, E^*)\right|_{exp} = \sum_{L=0}^{L=3} a_L(E^*) \left.\frac{d^2\sigma_L}{d\Omega\, dE}(\theta_{CM}, E^*)\right|_{theory} \tag{6.3}$$

where $\left.\frac{d^2\sigma_L}{d\Omega\, dE}(\theta_{CM}, E^*)\right|_{theory}$ is the angular distribution obtained from a DWBA calculation for a given excitation energy (E^*) and for multipoles $L = 0$, 1, 2 and 3. In theoretical calculations, it has been assumed that there is 100% exhaustion of the EWSR for each multipole. Figure 6.10 shows the results of the MDA analysis. For each energy interval, the obtained cross section is fitted with a linear combination of multipoles relevant to the energy interval under consideration. For example, the monopole mode contributes mainly between 10 MeV

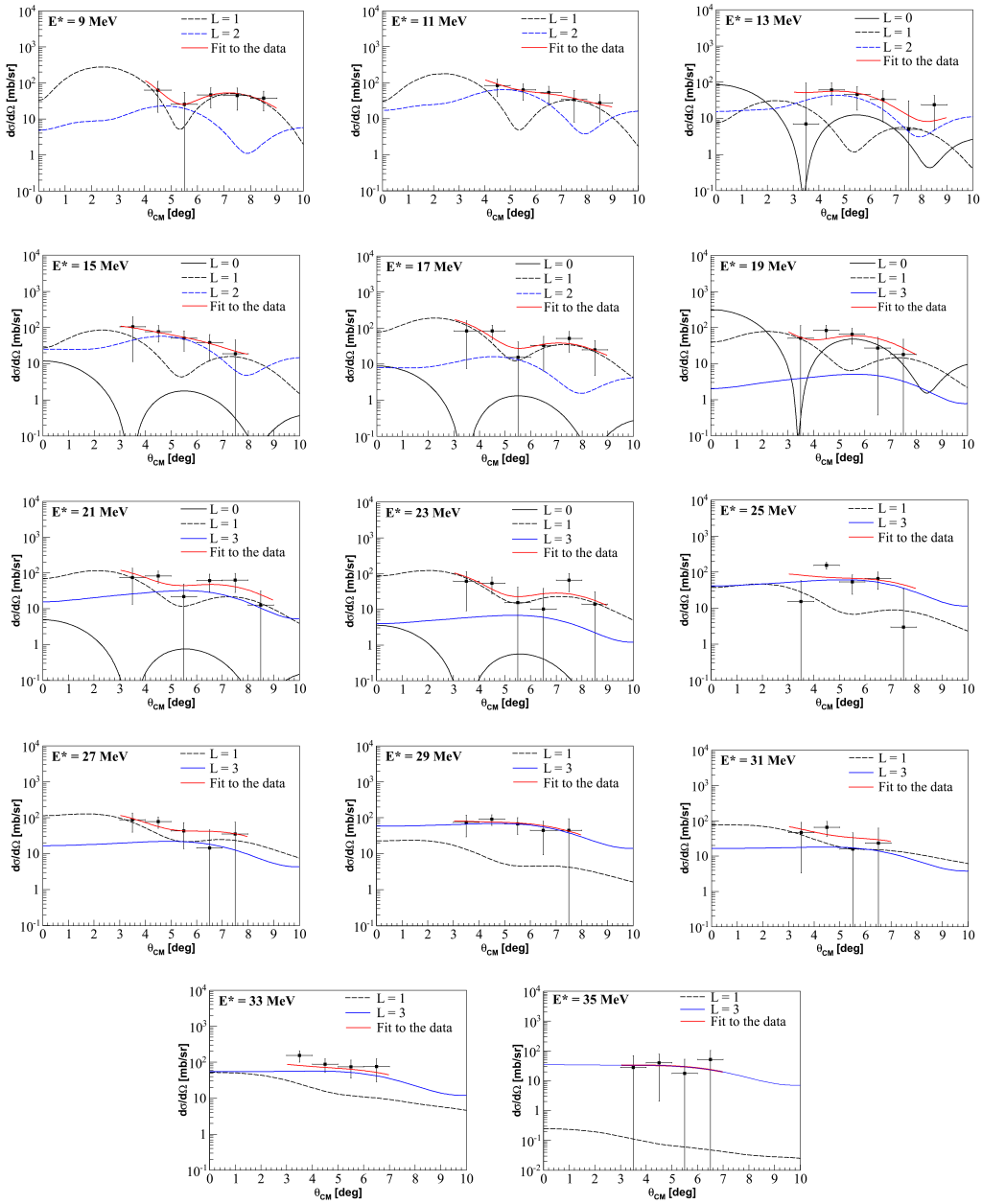

Figure 6.10: Fits to the angular distributions of the ^{56}Ni cross sections for excitation energy ranging from 9 MeV to 35 MeV with 2-MeV bin size. The theoretical angular distributions are obtained from DWBA calculations for the given excitation energy and multipole using the CHUCK3 code [59]. The parameters for the optical potential are given in Chapter2. For each figure, the contributions of the corresponding multipoles are also given.

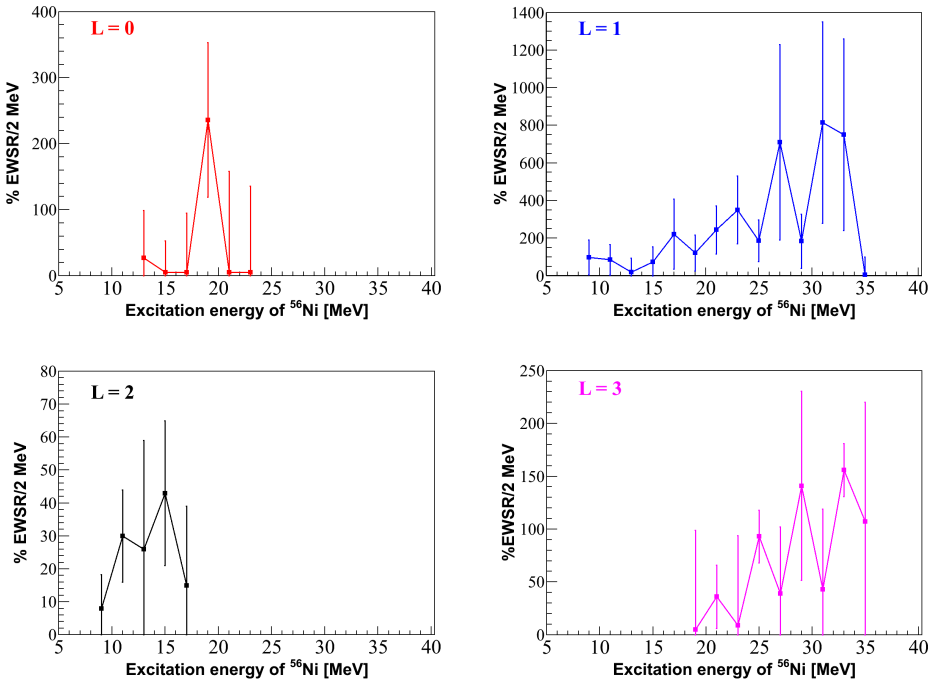

Figure 6.11: Percentage of EWSR exhausted for monopole (top left panel), dipole (top right panel), quadrupole (bottom left panel) and octupole (bottom right panel) obtained from MDA of spectra of inelastic α-particle scattering from ^{56}Ni.

to 25 MeV as can be seen from Refs. [50, 52] for ^{58}Ni. Similarly, the main contribution of the quadrupole mode ranges from 10 MeV to 18 MeV [50, 52, 53]. The dipole mode is more or less present throughout the whole excitation energy [50, 52]. The octupole mode starts contributing above 18 MeV. Since the angular domains in the phase-space limited MAYA detector are very narrow (from 3° upto 9° CM angle) the number of the data points in the obtained angular distributions is around 4 to 6. Therefore, the number of the parameters in the fits should be limited. Hence, in MDA, the multipoles which are relevant at a given excitation-energy interval are considered in the fitting instead of considering the contributions of all multipoles for all excitation-energy intervals. Furthermore, for MDA analysis, only the excitation energy upto 35 MeV has been considered because the data above 35 MeV suffer from the low acceptance of the MAYA detector.

The coefficient a_L is the fraction of EWSR for a multipolarity L at an excitation energy E^*. The coefficients for each multipole are plotted as a function of excitation energy of ^{56}Ni and

are shown in Fig. 6.11.

Error bars of the data are the square roots of the quadratic sums of errors due to statistical fluctuations, errors due to efficiency calculations and errors in the background heights. It can be noticed from Fig. 6.11 that the quadrupole modes contribute below 17 MeV and octupole modes contribute above 18 MeV. The dipole mode is more or less everywhere from 10 MeV to 35 MeV with an increase in percentage of EWSR at the higher excitation energies above 20 MeV. The monopole mode peaks around 19 MeV.

6.5 Discussion

For the first time, the giant resonances in ^{56}Ni have been studied through inelastic α-particle scattering using an active target. Since the α-particle has zero spin and isospin, predominantly the electric isoscalar modes are excited. For the following discussion, only the results from the Gaussian peak-fitting method and the MDA for the background shape obtained from fitting of the excitation-energy spectra assuming no structures are presented.

Monopole mode, L = 0

Both from the Gaussian peak-fitting method and MDA, the presence of the L = 0 mode has been established. In Table 6.2, the values of the peak positions and widths for the L = 0 mode obtained from this analysis along with the results obtained for the L = 0 mode from different reactions involving different isotopes of Ni are summarized.

From Table 6.2, it is clear that both the Gaussian peak-fitting method and MDA results are consistent in the centroid energy and the width of the L = 0 mode. The peak position of the monopole mode from this analysis (both Gaussian peak-fitting method and MDA) is consistent with that obtained from deuteron and α-particle scattering for ^{56}Ni and ^{58}Ni, respectively, and also with quasi-particle RPA calculations [49]. However, the width of the monopole mode obtained from this analysis is smaller than what has been observed by Monrozeau et al. [30]. A similar effect has also been observed by Vandebrouck et al. [54] from Lorentzian fits of excitation-energy spectra of ^{68}Ni obtained with inelastic α-particle scattering.

From the centroid value of the monopole mode, it is possible to calculate the nuclear incompressibility (K_A) for a finite nucleus using Eqn. 2.15. The rms radius ($\sqrt{< r^2 >}$) of the charge distribution for ^{56}Ni can be approximated by that for ^{58}Ni. From the Fermi charge-

	Gaussian fitting		MDA		Reaction
	E* [MeV]	FWHM [MeV]	m_1/m_0 [MeV]	rms [MeV]	
$L = 0$	19.1±0.5	2.0±0.3	18.4±1.8	2.0±1.2	^{56}**Ni(**α,α'**)**^{56}**Ni*** (this work)
$L = 0$	19.5±0.3	5.2	19.3±0.5	2.3	^{56}**Ni(**d, d'**)**^{56}**Ni*** [30, 53]
$L = 0$	18.43±0.15	7.41±0.13	$19.2^{+0.44}_{-0.19}$	$4.89^{+1.05}_{-0.31}$	^{58}**Ni(**α,α'**)**^{58}**Ni*** [50]
$L = 0$	-	-	$19.9^{+0.7}_{-0.8}$	-	^{58}**Ni(**α,α'**)**^{58}**Ni*** [52]
$L = 0$	17.62±0.15	7.55±0.13	$18.04^{+0.35}_{-0.23}$	$4.5^{+0.97}_{-0.22}$	^{60}**Ni(**α,α'**)**^{60}**Ni*** [50]
$L = 0$	21.1±1.9	1.3±1.0	23.4	6.5	^{68}**Ni(**α,α'**)**^{68}**Ni*** [54]

Table 6.2: Results obtained from the Gaussian peak-fitting method and MDA for the $L = 0$ mode from different reactions and for different isotopes of Ni. For the last entry of the table, the peaks in the excitation-energy spectrum were fitted with Lorentzian functions instead of Gaussian functions. The rms is the root-mean-square width of the multipole strength as obtained from MDA. In MDA, the excitation energy of a multipole is defined by the ratio m_1/m_0. See Chapter 2 for definitions of m_1 and m_0.

distribution model, the rms value of the radius of the charge distribution for ^{58}Ni is given as 3.764(10) fm [83]. The value of K_A thus obtained from the Gaussian peak-fitting method is 125.1(4.4) MeV whereas from MDA, the value of K_A has been calculated as 116.0(11.5) MeV.

Dipole mode, $L = 1$

From Fig. 6.11, it is evident that the dipole mode is present everywhere in the excitation-energy range from 10 MeV to 35 MeV. Due to the uncertainty in subtracting the background, possible contributions from the continuum due to knock-out reactions could also be there. However, the events at higher energies also suffer from low-efficiency.

The fingerprint of the low-lying $L = 1$ mode has been found both in the Gaussian peak-fitting method and MDA at an excitation energy of around 17 MeV. According to Refs. [50, 52], there is evidence of a low-lying dipole mode for ^{58}Ni around 16-17 MeV which is higher than the $1\hbar\omega$ component of ISGDR leading to the *bi-modal* nature of ISGDR with the cen-

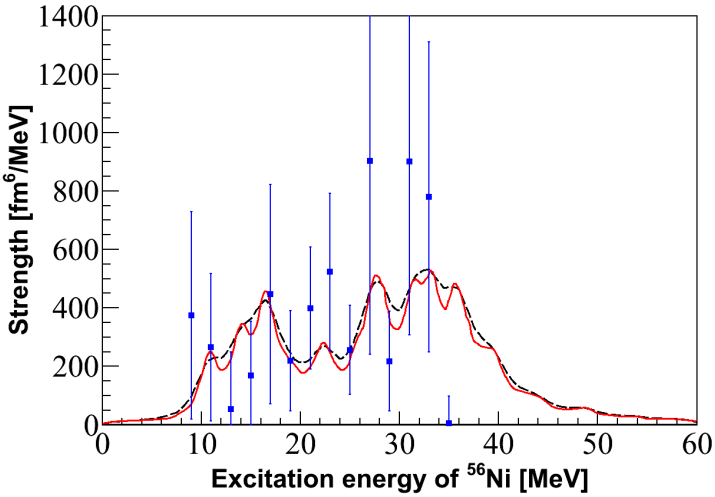

Figure 6.12: Comparison of the experimental ISGDR strength distribution (blue data points) in ^{56}Ni with the prediction of recent HF-RPA calculation (red solid line) [80]. The theoretical prediction has been convoluted with the experimental resolution (black dashed line).

troid of the high-energy component appearing around 30 MeV. From quasi-particle RPA calculations [49], a similar behavior of the ISGDR has been found with the low-lying component for $L = 1$ appearing around 16 MeV.

The MDA was carried out for excitation energies upto 35 MeV because in the present experimental setup the events at higher excitation energies suffer from low acceptance of the detector. Therefore, the drop of the percentage of EWSR for the dipole mode at 35 MeV is most probably due to the acceptance. To get a quantitative understanding of the ISGDR strength distribution, the experimental strength distribution has been compared with the predictions from Hartree-Fock- (HF-) based RPA calculations [80] as shown in Fig. 6.12.

In Fig. 6.12, the ISGDR strength distribution for ^{56}Ni is convoluted with the experimental energy resolution as shown in black dashed line. The evolution of the experimental data is more or less the same as the convoluted theoretical prediction but with large errors. Also the data points are scaled down by a factor 4 which leads to the fact that in the present analysis the observed EWSR exceeds 100% of the theoretical sum rule by a factor of 2 to 4 as can be seen also from Fig. 6.11. Since in the present analysis no events have been analyzed above 35 MeV, there are no data points above 35 MeV in Fig. 6.12.

	Gaussian fitting		MDA		Reaction
	E* [MeV]	FWHM [MeV]	m_1/m_0 [MeV]	rms [MeV]	
$L = 2$	11.0±0.5 14.4±0.5	2.0±0.3 2.2±0.2	13.4±0.9	2.3±0.7	^{56}**Ni(α,α')^{56}Ni*** (this work)
$L = 2$	16.5±0.3	5.2	16.2±0.5	1.7	^{56}**Ni**$(d, d')^{56}$**Ni*** [30,53]
$L = 2$	16.64±0.12	$5.81^{+0.16}_{-0.11}$	$16.31^{+0.17}_{-0.10}$	2.45±0.10	^{58}**Ni(α,α')^{58}Ni*** [50]
$L = 2$	-	-	$16.3^{+0.8}_{-0.9}$	-	^{58}**Ni(α,α')^{58}Ni*** [52]
$L = 2$	16.05±0.12	$6.61^{+0.16}_{-0.11}$	$15.84^{+0.18}_{-0.10}$	2.92±0.10	^{60}**Ni(α,α')^{60}Ni*** [50]
$L = 2$	15.9±1.3	2.3±1.0	16.2	1.0	^{68}**Ni(α,α')^{68}Ni*** [54,69]

Table 6.3: Results obtained from the Gaussian peak-fitting method and MDA for the $L = 2$ mode from different reactions and for different isotopes of Ni. For the last entry of the table, the peaks in the excitation-energy spectrum were fitted with Lorentzian functions instead of Gaussian functions.

Quadrupole mode, $L = 2$

The presence of the $L = 2$ mode has also been found from the Gaussian peak-fitting method and MDA. In the Gaussian peak-fitting method, the differential cross sections of peaks #2 and #3 (see Figs. 6.7, 6.8 and 6.9) are found to be best fit by a quadrupole angular distribution. In Table 6.3, the values of the peak positions and widths for the $L = 2$ mode, obtained from this analysis along with the results obtained for the $L = 2$ mode from different reactions involving different isotopes of Ni, are summarized.

From Table 6.3, it is clear that the peak position for the quadrupole mode is lower than that for ^{56}Ni with inelastic deuteron scattering and is also lower from the peak positions of the quadrupole mode for ^{58}Ni by almost 2-3 MeV. However, the results obtained from the Gaussian peak-fitting method and MDA are consistent with each other. The rms width of the $L = 2$ mode is consistent with the rms widths for the different isotopes of Ni except for the last one.

Octupole mode, $L = 3$

In MDA analysis, the $L = 3$ component has also been considered for excitation energies greater than 18 MeV. The percentage of EWSR for the $L = 3$ mode increases above 20 MeV. The same effect has also been observed by Lui et al. [50] for ^{58}Ni with inelastic α-particle scattering.

In the present analysis, the EWSR is not mentioned for any of the multipole giant resonances. As can be seen from Figs. 6.9 and 6.11, the percentages of EWSR, mainly for the $L = 0$ (which is in this case 236%) and the $L = 1$ (which is in this case 3862%), exceed 200%, which is hardly physical in spite of the large error bars. This could be due to the fact that the background shape is not estimated properly. Furthermore, from Fig. 6.2, it can be seen that the overall statistics is very poor. Due to the large errors, the percentage of EWSR cannot be measured reliably.

Chapter 7

Summary and outlook

Summary

With the advent of new types of accelerators, it is nowadays possible to access nuclei with exotic neutron-to-proton (N/Z) ratios in the nuclear chart. How the structure and properties of a nucleus, especially its collectivity, change with exotic (N/Z) ratios is still one of the fundamental questions in the field of nuclear physics. In fact, the study of collective modes in stable nuclei, the so-called Giant Resonances (GR), has been one of the physics motivations throughout the history of nuclear physics. Among these collective modes, the Isoscalar Giant Monopole Resonance (ISGMR) and the Isoscalar Giant Dipole Resonance (ISGDR) are of prime interests as their excitation energies are directly related to the nuclear incompressibility of a finite nucleus. The nuclear incompressibility of nuclear matter can be defined as the curvature of the binding energy per particle at the saturation density. It is an important key input to the equation of state of nuclear matter which, in turn, is useful in understanding some astrophysical phenomena such as masses of neutron stars and supernovae explosions.

Among the collective modes of a nucleus, an isoscalar mode refers to the oscillations of protons and neutrons in phase whereas an isovector mode refers to the oscillations of protons and neutrons out of phase. The ISGMR and ISGDR can be studied via inelastic α-particle scattering as the α-particle has its spin and isospin both equal to zero. The main motivation of this thesis is to study the ISGMR and ISGDR in ^{56}Ni with inelastic α-particle scattering although the ISGMR and Isoscalar Giant Quadrupole Resonance (ISGQR) in ^{56}Ni have been previously studied via inelastic deuteron scattering [53]. Since ^{56}Ni is an exotic (neutron-deficient) unstable nucleus, it cannot be used as a target. Therefore, we have performed

our experiment in inverse kinematics. Dealing with exotic beams is very challenging, as the intensity of such beams is very low, so to get a reasonable yield, a thick target is needed. However, the usage of a thick target can degrade the energy resolution and very low-energy recoil particles may not come out of the target. A storage-ring facility where the luminosity of the exotic beam can be increased by accumulation and circulation of the beam in the ring, for example the ESR at GSI, is a good alternative. Another approach is to use an active target: a gas detector where the target gas also acts as a detector. Such an example is the MAYA active-target detector.

We have performed our experiment at GANIL in Caen, France in May, 2011. The main aim is to study the ISGMR and ISGDR in ^{56}Ni with inelastic α-particle scattering using the active target MAYA with a beam energy of 50 MeV/u. MAYA is a time-charge projection chamber, which was filled, in our experiment, with 95% He and 5% CF_4 at a pressure of 500 mbar. Since the GR state of a nucleus is above the particle-emission threshold, ^{56}Ni will decay by emitting mainly protons and α-particles. These decay particles are very forward focused and will not stop inside the MAYA volume as they have almost the same energy per nucleon as the beam. To detect these particles, additional Si-CsI telescopes have been placed in the forward direction. Details of the ^{56}Ni beam-production method from the stable ^{58}Ni primary beam, the existing facility at GANIL and the experimental setup of the MAYA active-target detector are given in Chapter 3.

Data analysis has been performed using the ROOT framework. The ^{56}Ni-beam selection and the geometrical and event-reconstruction selection conditions for the recoil α-particles are detailed in Chapter 4. The data analysis has been performed on an event-by-event basis. In order to understand the detector efficiency and acceptance, extensive simulations have been performed using the inputs from the LISE++ [78] and SRIM [61] software packages. The details are given in Chapter 5.

For a complete understanding of the GR structures, the angular distributions have to be reconstructed. To obtain the absolute cross sections, elastic-scattering of α-particles from ^{56}Ni has been studied. The angular distributions of giant resonances have been obtained in two different ways. The first method is the Gaussian peak-fitting method, where the events are considered for a given center-of-mass (CM) angle to obtain the excitation-energy spectrum for that angle. The peaks in the obtained excitation-energy spectra are fitted with Gaussian functions and the areas of these Gaussian functions will then lead to the angular distributions. However, a background has to be subtracted beforehand.

The nature of the GR states can also be deduced from another independent analysis which is

called the Multipole-Decomposition Analysis (MDA). In this case, the events are considered for a given excitation-energy interval to obtain the angular distribution for that excitation energy. The obtained angular distributions for each energy interval are then fitted with a linear combination of theoretical cross sections of multipoles relevant to the energy interval under consideration. The theoretical differential cross sections were calculated within the distorted-wave Born approximation (DWBA) framework using the CHUCK3 code [59].

In both methods, the existence of the $L = 0$ mode (ISGMR) of ^{56}Ni was established. The peak position of the monopole mode obtained from the Gaussian peak-fitting method is found to be at 19.1$\pm$0.5 MeV whereas the value obtained from the MDA is found to be at 18.4$\pm$1.8 MeV. The FWHM values obtained from the Gaussian peak-fitting method and the MDA are 2.0$\pm$0.3 MeV and 2.0$\pm$1.2 MeV, respectively. Both the results (centroid position and FWHM of the monopole mode) are consistent with each other within the error bars.

The fingerprint of the low-lying dipole ($L = 1$) mode in ^{56}Ni has been found both in the Gaussian peak-fitting method and in the MDA at an excitation energy around 17 MeV. As expected, the dipole strength increases at high excitation energies, leading to the high-energy component of the *bi-modal* nature of the ISGDR strength. The *bi-modal* nature of the ISGDR has also been found in ^{58}Ni with the low-lying peak appearing around 16-17 MeV and the high-energy component around 30 MeV [50, 52]. In this analysis, the evolution of the ISGDR strength in the ^{56}Ni data has been found to be, more or less, similar to the predictions obtained from the quasi-particle random-phase-approximation (QRPA) calculations [80] although the percentage of energy-weighted sum rule (EWSR) exceeds 200% which is hardly physical. This could be due to the lack of knowledge in background subtraction.

The presence of the $L = 2$ mode (ISGQR) in ^{56}Ni has also been found although the centroid position appears at least 2 MeV lower than what has been found for ^{56}Ni with inelastic deuteron scattering [53]. However, the root-mean-square (rms) width of the strength distribution was found to be consistent with results for almost all other Ni isotopes found in different experiments [50].

For excitation energies higher than 20 MeV, the octupole mode ($L = 3$) also starts contributing as MDA suggests.

From the centroid value of the monopole mode, it is possible to calculate the nuclear incompressibility (K_A) for a finite nucleus using Eqn. 2.15. The rms radius ($\sqrt{< r^2 >}$) of the charge distribution for ^{56}Ni can be approximated by that for ^{58}Ni. From the Fermi charge-distribution model, the rms value of the radius of the charge distribution for ^{58}Ni is given as 3.764(10) fm [83]. The value of K_A for ^{56}Ni thus obtained from the Gaussian

peak-fitting method is 125.1(4.4) MeV whereas from MDA, the value of K_A has been calculated as 116.0(11.5) MeV.

Outlook

This thesis presents the analysis of an experiment which aimed to study the compression modes in ^{56}Ni with inelastic α-particle scattering. For this purpose, we have used the active-target detector MAYA. During the experiment and data-analysis, a number of challenges have been faced. In future, when performing experiments with such an experimental setup, these challenges have to be kept in mind and it is necessary to take actions accordingly. Few points for further improvements of such experimental setup and operating conditions are mentioned below.

Since MAYA is a time-charge projection chamber, the pressure of the gas inside MAYA has to be kept as low as possible for a two-body reaction where both the heavy and light particles have traces on the cathode pads. This will ensure that, most of the recoil particle will come out of the beam region and therefore, can easily be detected. It can be seen from the present analysis that, the long recoil-particle tracks have better resolution in the reconstructed range, energy and scattering angle as compared to the short recoil-particle tracks. Short recoil-particle tracks are difficult to reconstruct as they are closer to the beam region. If the pressure of the gas-mixture inside MAYA is low, most of the recoil-particle tracks will fall under the long-tracks category leading to better results. However, for lower gas pressure, the target will get thinner and therefore, the yields of the reaction of interest will go down. Therefore, the pressure of the gas mixture should be adjusted at the optimum value. Another alternative is to make the active target longer.

If the pressure is low, then the recoil particles having high energies will punch through the MAYA volume. This will lower the acceptance of the detector. Therefore, to solve this problem, MAYA should be surrounded with solid-state detectors to detect the particles that punch through and measure their energy loss and/or energy deposited in the ancillary solid-state detectors.

A proper beam monitor should be installed inside the MAYA chamber. This will ensure the proper counting of the number of incoming beam particles. Although in our experiment there was a diamond detector to monitor the incoming beam particles, it was unfortunately not working during the experiment. Therefore, no information could be extracted from it except using it as a beam dump.

The granularity of the cathode pads also determines the resolution of the extracted range of the recoil particle tracks. In MAYA, the cathode pads are hexagonal in shape with the length of the sides as 5 mm. However, in the future type of active targets, such as ACTAR [70], the cathode pads are smaller in size (2 mm and square in shape) and therefore, lead to better resolution of the reconstructed kinematics variables. This will improve the angular resolution which is important in the study of cross sections in the minima.

Chapter 8

Nederlandse samenvatting

Met de komst van nieuwe types versnellers, is het tegenwoordig mogelijk om kernen met exotische neutron-tot-proton *(N/Z)* verhoudingen in de nucleaire grafiek te bereiken. Hoe de structuur en eigenschappen van een kern, met name de collectiviteit, veranderen met exotische N/Z verhoudingen is nog steeds een van de fundamentele vragen op het gebied van kernfysica. In feite is de studie van collectieve modi van stabiele kernen, de zogenaamde Giant Resonanties (GR), altijd een van de belangrijkste motivaties voor het beoefenen van de kernfysica geweest. Onder deze collectieve modi zijn de Isoscalaire reuzenmonopool resonantie (ISGMR = Isoscalar Giant Monopole Resonance) en de Isoscalaire reuzendipool resonantie (ISGDR = Isoscalar Giant Dipole Resonance) van bijzonder belang, aangezien hun excitatie-energieën direct gerelateerd zijn aan de nucleaire onsamendrukbaarheid van een eindige kern. De nucleaire onsamendrukbaarheid van kernmaterie kan worden gedefinieerd als de kromming van de bindingsenergie per deeltje bij de verzadigingsdichtheid. Het is een belangrijke input voor de toestandsvergelijking van kernmaterie, dat op zijn beurt helpt om enkele astrofysische verschijnselen zoals de massa's van neutronensterren en supernovae explosies te begrijpen.

Onder de collectieve modi van een kern beschrijft een isoscalaire modus de trillingen van protonen en neutronen in fase, terwijl een isovector modus trillingen van protonen en neutronen uit fase beschrijft. De ISGMR en ISGDR kunnen onderzocht worden via inelastische α-deeltje-verstrooiing, aangezien de spin en isospin van α-deeltjes beide gelijk aan nul zijn. De belangrijkste motivatie van dit proefschrift is om de ISGMR en ISGDR in ^{56}Ni te bestuderen via inelastische α-deeltje-verstrooiing, hoewel de ISGMR en de isoscalaire reuzenquadrupool resonantie (ISGQR = Isoscalar Giant Quadrupole Resonance) in ^{56}Ni reeds via inelastische deuteronverstrooiing bestudeerd zijn [53]. Aangezien ^{56}Ni een ex-

otische (neutron-deficiënte), onstabiele kern is, kan deze niet worden gebruikt als een trefplaat. Daarom hebben we ons experiment uitgevoerd via omgekeerde kinematica. Omgaan met exotische stralen is zeer uitdagend, aangezien de intensiteit van dergelijke bundels zeer laag is, waardoor een dikke trefplaat nodig is om een redelijke opbrengst te krijgen. Echter kan het gebruik van een dikke trefplaat de energieresolutie degraderen, en zeer laag-energetiche terugstootdeeltjes kunnen mogelijk niet uit de trefplaat ontsnappen. Een opslagringfaciliteit, waar de intensiteit van de exotische bundel kan worden verhoogd door de ophoping en omloop van de bundel in de ring, bijvoorbeeld in de ESR bij GSI, is een goed alternatief. Een andere benadering is om een actieve trefplaat te gebruiken: een gasdetector waarin het doelgas ook als een detector fungeert. Een voorbeeld hiervan is de MAYA actieve-trefplaat-detector.

We hebben ons experiment uitgevoerd in GANIL in Caen, Frankrijk in mei 2011. Het belangrijkste doel was om de ISGMR en ISGDR in ^{56}Ni via inelastische α-deeltje-verstrooiing te onderzoeken met de actieve trefplaat MAYA, met een bundel-energie van 50 MeV/u. MAYA is een tijd-lading projectiekamer, die gevuld was met 95% He en 5% CF_4 bij een druk van 500 mbar. Omdat de reuzenresonantie toestand van een kerndeeltje boven de deeltjesemissie-drempel ligt, vervalt ^{56}Ni door het uitzenden van voornamelijk protonen en α-deeltjes. De uitzendrichting van deze vervaldeeltjes is zeer naar voren gericht, en zij zullen niet stoppen in het MAYA volume, omdat ze bijna dezelfde energie per kerndeeltje hebben als de bundel. Om deze deeltjes te detecteren zijn aanvullende Si-CsI telescopen geplaatst in voorwaartse richting. Details van de ^{56}Ni bundelproductiemethode uit de stabiele primaire ^{58}Ni-bundel, de bestaande faciliteit in GANIL en de experimentele opstelling van de MAYA actieve-trefplaat-detector worden gegeven in hoofdstuk 3.

De data-analyse werd uitgevoerd met het ROOT computerprogramma. De selectie van de ^{56}Ni-bundel en de geometrische en gebeurtenisreconstructie selectievoorwaarden voor de terugstoot α-deeltjes worden beschreven in hoofdstuk 4. De data-analyse werd op een gebeurtenis-per-gebeurtenis basis uitgevoerd. Om de doelmatigheid en acceptatie van de detector te begrijpen zijn uitgebreide simulaties uitgevoerd met behulp van de input van de LISE++ [78] en SRIM [61] softwarepaketten. De details hiervan worden gegeven in hoofdstuk 5.

Voor een volledig begrip van de GR structuren, moten de hoekverdelingen worden gereconstrueerd. Om de absolute werkzame doorsneden te verkrijgen is de elastische verstrooiing van α-deeltjes op ^{56}Ni onderzocht. De hoekverdelingen van de reuzenresonanties zijn verkregen op twee verschillende manieren. De eerste methode is de Gauss-piek passende methode, waarbij de gebeurtenissen voor een gegeven massamiddelpuntshoek worden bes-

chouwd het excitatie-energiespectrum te verlrijgen behorende bij die hoek. De pieken in de verkregen excitatie-energiespectra worden dan gepast met Gaussische functies en de oppervlakte onder deze functies voor de verschillende hoeken leidt tot de hoekverdelingen. Echter dient de achtergrond vooraf te worden afgetrokken.

De aard van de GR toestanden kan ook worden bepaald uit een andere, onafhankelijke analyse, genaamd de Multipool-Decompositie Analyse (MDA). In dit geval worden de gebeurtenissen beschouwd voor een gegeven excitatie-energie-interval om de hoekverdeling bij die excitatie-energie te verkrijgen. De verkregen hoekverdelingen per energie-interval worden dan gepast met een lineaire combinatie van theoretische werkzame doorsneden van multipolen die relevant zijn voor dit energie-interval. De theoretische differentiële werkzame doorsneden werden berekend binnen het vervormde-golf Born-benaderingkader (Distorded-Wave Born Approximation, DWBA) met behulp van de CHUCK3 code [59].

Bij beide werkwijzen werd het bestaan van de $L = 0$ modus (ISGMR) van ^{56}Ni vastgesteld. De piekpositie van de monopoolmodus, verkregen uit de Gauss-piek passende methode, werd vastgesteld op 19,1$\pm$0,5 MeV, terwijl die van de MDA methode op 18,4$\pm$1,8 MeV ligt. De FWHM waarde verkregen uit de Gauss-piek passende en MDA methodes zijn 2,0$\pm$0,3 MeV en 2,0$\pm$1,2 MeV, respectievelijk. Zowel de resultaten voor de zwaartepuntpositie en de FWHM van de monopoolmodus zijn consistent met elkaar binnen de foutmarges.

De vingerafdruk van de laaggelegen dipool ($L = 1$) modus in ^{56}Ni is zowel in de Gauss-piek passende methode en in de MDA methode gevonden bij een excitatie-energie van ongeveer 17 MeV. Zoals verwacht neemt de dipoolsterkte toe bij hoge excitatie-energieën; dit leidt tot de hoge-energiecomponent van de bimodale aard van de ISGDR-sterkte. Deze bimodale aard is ook gevonden in ^{58}Ni, waar de laaggelegen piek rond 16-17 MeV en de hoge-energiecomponent bij ongeveer 30 MeV zijn gevonden [50, 52]. In deze analyse blijkt de evolutie van de ISGDR-sterkte in de ^{56}Ni data min of meer overeen te komen met de voorspellingen van de quasi-deeltjes willekeurige-fase-benadering (Quasi-particle Random-Phase Approximation, QRPA) berekeningen [80], hoewel het percentage van de energie-gewogen somregel (Energy-weighted sum rule, EWSR) hoger uitkomt dan 200%, hetgeen niet echt fysisch kan zijn. Dit kan te wijten zijn aan het gebrek aan kennis in de achtergrondaftrekking.

De aanwezigheid van $L = 2$ modus (ISGQR) in ^{56}Ni is ook gevonden, hoewel de zwaartepuntpositie tenminste 2 MeV lager is dan wat gevonden werd voor ^{56}Ni via inelastische deuteronverstrooiing [53]. Echter komt de rms-breedte van de sterkteverdeling wel overeen met de resultaten die voor bijna alle andere Ni isotopen gevonden zijn in verschillende experi-

menten [50].

Bij excitatie-energieën hoger dan 20 MeV begint de octupoolmodus (L = 3) eveneens bij te dragen, zoals de MDA methode suggereert.

Uit de zwaartepuntpositie van de monopoolmodus is het mogelijk om de nucleaire onsamendrukbaarheid (K_A) te berekenen voor een eindige kern met behulp van Vergelijking 2.15. De rms-straal ($\sqrt{< r^2 >}$) van de ladingsverdeling voor ^{56}Ni kan worden benaderd met die van ^{58}Ni. Met het Fermi ladingsverdelingmodel, wordt de effectieve waarde van de straal van de ladingsverdeling voor ^{58}Ni bepaald op 3,764(10) fm [83]. Hiermee komt de waarde van K_A voor ^{56}Ni, verkregen met de Gauss-piek passende methode, op 125,1(4,4) MeV, terwijl met de MDA methode de waarde van K_A berekend is op 116,0(11,5) MeV.

Appendix A

Decay scheme of ^{226}Ra [72]. The α-lines with bold letters, are used to calibrate the ancillary detectors as mentioned in Chapter 4.

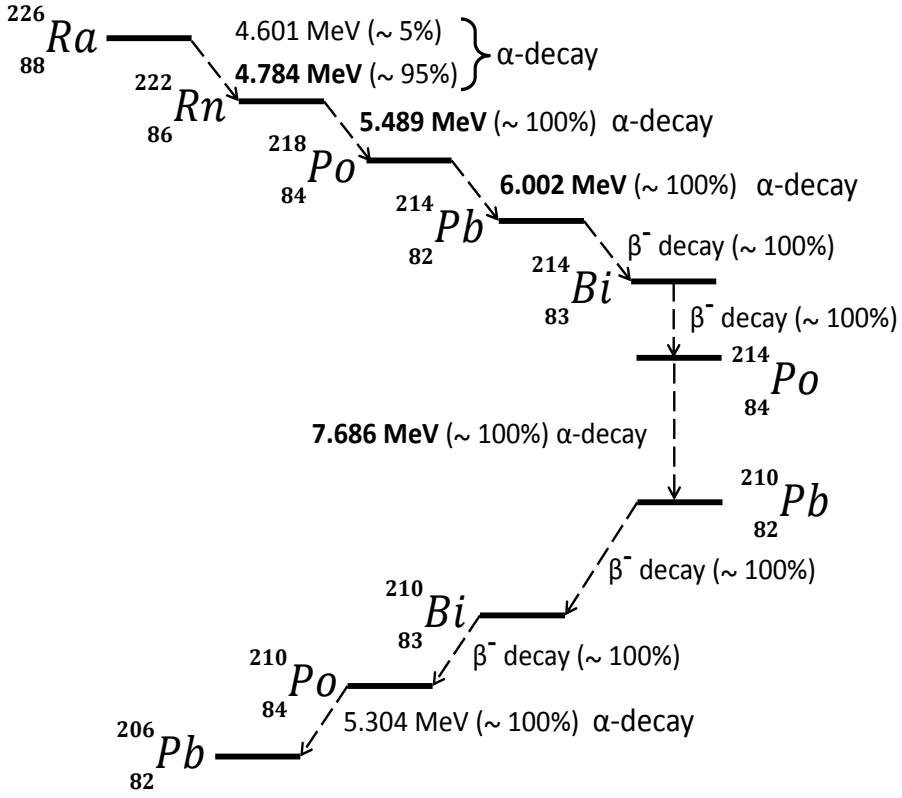

Appendix B

The formulas for strength distribution for isoscalar giant resonances for different multipolarities are given below [4, 52].

- Isoscalar Giant Monopole Resonance ($L = 0$, $T = 0$)

$$S_0(E_x) = \frac{\hbar^2}{2mE_x} A\langle r^2\rangle a_0(E_x) \tag{1}$$

- Isoscalar Giant Dipole Resonance ($L = 1$, $T = 0$)

$$S_1(E_x) = \frac{\hbar^2}{8\pi mE_x}\frac{3}{4}A\{11\langle r^4\rangle - \frac{25}{3}\langle r^2\rangle^2 - 10\epsilon\langle r^2\rangle\}a_1(E_x) \tag{2}$$

- Isoscalar Giant Multipole Resonance ($L \geqslant 2$, $T = 0$)

$$S_{\geqslant 2}(E_x) = \frac{\hbar^2}{8\pi mE_x} L(2L+1)^2 A\langle r^{2L-2}\rangle a_L(E_x) \tag{3}$$

where m, A and $\langle r^N\rangle$ are the nucleon mass, the mass number and the N-th moment of the ground-state density, respectively. The factor ϵ defined as $\epsilon = (\frac{4}{E_{ISGQR}} + \frac{5}{E_{ISGMR}})\frac{\hbar^2}{3mA}$, where E_{ISGMR} and E_{ISGQR}, given in Eqns. 2.1 & 2.3, are the excitation energies of the isoscalar giant monopole and quadrupole resonances, respectively. E_x is the excitation energy under consideration. $a_L(E_x)$ is the fraction of the EWSRs and defined in Eqn. 6.3 in Chapter 6.

Appendix C

Level scheme of ^{56}Ni [72].

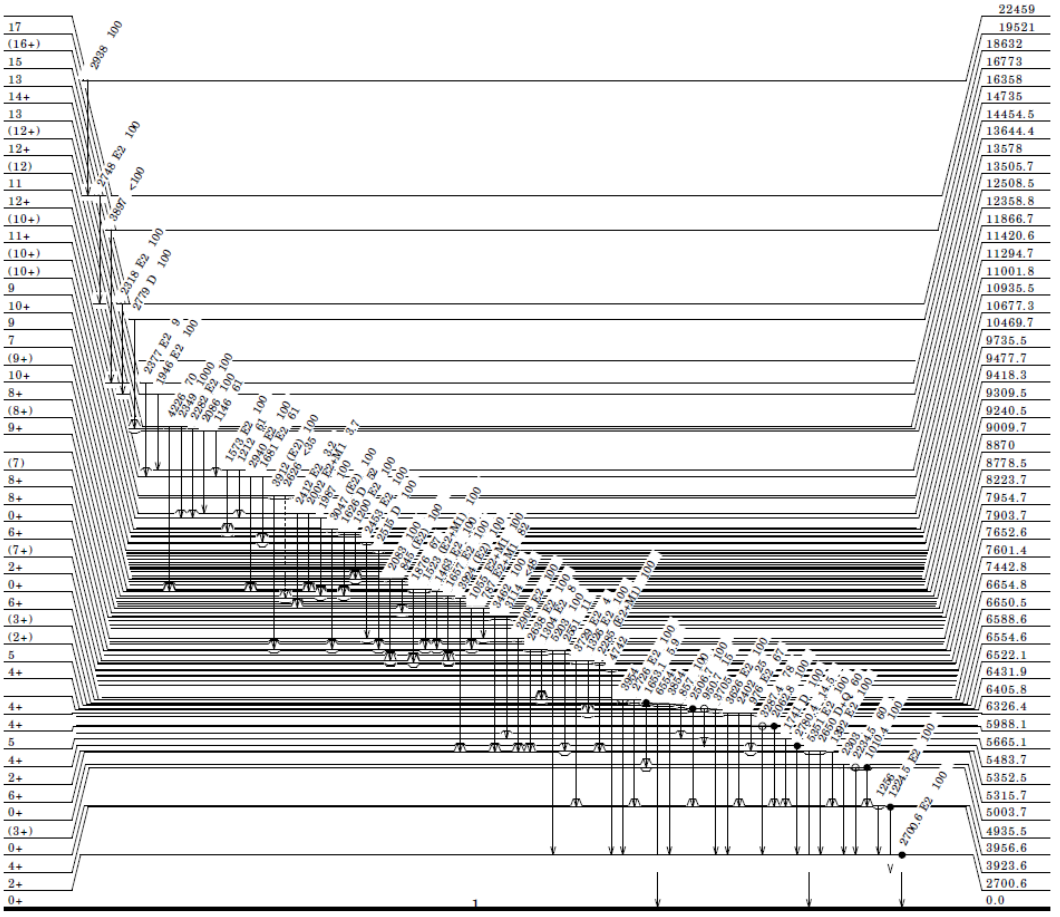

Bibliography

[1] I. Tanihata *et al.*, *Phys. Rev. Lett.* **55** (1985) 2676.

[2] M. Thoennessen, *Rep. Prog. Phys.* **76** (2013) 056301.

[3] T. Aumann and T. Nakamura, *Physica Scripta* **T152** (2013) 014012.

[4] M. N. Harakeh & A. van der Woude, Giant resonances, fundamental high-frequency modes of nuclear excitation, Oxford science publications (2001).

[5] W. Bothe and W. Genter, *Z. Phys.* **71** (1937) 236.

[6] A. Migdal, *J. Phys. (USSR)* **8** (1944) 331.

[7] G. C. Baldwin and G. S. Klaiber, *Phys. Rev.* **71** (1947) 3.

[8] G. C. Baldwin and G. S. Klaiber, *Phys. Rev.* **73** (1948) 1156.

[9] R. Pitthan and Th. Walcher, *Phys. Lett.* **36B** (1971) 563.

[10] M. N. Harakeh *et al.*, *Phys. Rev. Lett.* **38** (1977) 676.

[11] M. N. Harakeh *et al.*, *Nucl. Phys. A* **327** (1978) 373.

[12] H. P. Morsch *et al.*, *Phys. Rev. Lett.* **45** (1980) 337.

[13] C. Djalali *et al.*, *Nucl. Phys. A* **380** (1982) 42.

[14] H. P. Morsch *et al.*, *Phys. Rev. C* **28** (1983) 1947.

[15] B. Bonin *et al.*, *Nucl. Phys. A* **430** (1984) 349.

[16] G. S. Adams *et al.*, *Phys. Rev. C* **33** (1986) 2054.

[17] U. Garg, *Nucl. Phys. A* **649** (1999) 66c.

[18] B. F. Davis *et al.*, *Nucl. Phys. A* **569** (1994) 325c.

[19] B. F. Davis *et al.*, *Phys. Rev. Lett.* **79** (1997) 609.

[20] R. Pitthan, *Proc. Giant Multipole Resonance Tropical Conf. Oak Ridge 1979* (1980).

[21] Y. Torizuka *et al.*, *Phys. Rev. C* **11** (1975) 1174.

[22] D. A. Sims *et al.*, *Phys. Rev. C* **55** (1997) 1288.

[23] J. D. Bowman *et al.*, *Phys. Rev. Lett.* **50** (1983) 1195.

[24] T. Blaich *et al.*, *Nucl. Instr. Meth. Phys. Res. A* **314** (1992) 136.

[25] J. Gibelin, Ph.D. thesis, L'Université PARIS XI; *Search for low lying dipole strength in the neutron rich nucleus* ^{26}Ne, (2005).

[26] A. Leistenschneider *et al.*, *Phys. Rev. Lett.* **86** (2001) 5442.

[27] M. A. Najafi, Ph.D. thesis, Rijksuniversiteit Groningen; *Quasi-free proton and neutron knockout reaction in* ^{20}O, (2014).

[28] P. Egelhof *et al.*, *Physica Scripta* **T104** (2003) 151.

[29] H. Moeini, Ph.D. thesis, Rijksuniversiteit Groningen; *Feasibility experiment and simulations for EXL*, (2010).

[30] C. Monrozeau, Ph.D. thesis, Université Paris XI; *Nouvelle Méthode expérimentale dédiée à l'étude des modes collectifs dans les noyaux exotiques; Influence de la superfluidité sur le temps de refroidissement d'une étoile à neutrons* (2007).

[31] O. Bohigas *et al.*, *Phys. Reports* **51** (1979) 276.

[32] J. P. Blaizot *et al.*, *Nucl. Phys. A* **591** (1995) 435.

[33] F. Zwarts *et al.*, *Nucl. Phys. A* **439** (1985) 117.

[34] S. Brandenberg *et al.*, *Phys. Lett.* **130B** (1983) 1.

[35] G. O. Bolme *et al.*, *Phys. Rev. Lett.* **61** (1988) 9.

[36] M. Hunyadi *et al.*, *Phys. Rev. C* **80** (2009) 044317.

[37] G. Colò, *Physics of Particles and Nuclei*, **39** (2008) 286.

[38] J. P. Blaizot, *Phys. Rep.* **64** (1980) 171.

[39] J. Treiner *et al.*, *Nucl. Phys. A* **371** (1981) 253.

[40] J. M. Pearson, *Phys. Lett. B* **271** (1991) 12.

[41] B. K. Agrawal *et al.*, *Phys. Rev. C* **68** (2003) 031304(R).

[42] U. Garg, *Nucl. Phys. A* **731** (2004) 3.

[43] G. Colò *et al.*, *Phys. Rev. C* **70** (2004) 024307.

[44] B. G. Todd-Rutel and J. Piekarewicz, *Phys. Rev. Lett.* **95** (2005) 122501.

[45] J. Piekarewicz, *J. Phys. G* **37** (2010) 064038.

[46] J. Piekarewicz, *Phys. Rev. C* **76** (2007) 031301.

[47] U. Garg *et al.*, *Nucl. Phys. A* **788** (2007) 36c.

[48] D. Patel *et al.*, *Phys. Lett. B* **718** (2012) 447.

[49] J. Terasaki and J. Engel, *Phys. Rev. C* **74** (2006) 044301.

[50] Y. Lui *et al.*, *Phys. Rev. C* **73** (2006) 014314.

[51] Y. Lui *et al.*, *Phys. Rev. C* **61** (2000) 067307.

[52] B. K. Nayak *et al.*, *Phys. Lett. B* **637** (2006) 43.

[53] C. Monrozeau *et al.*, *Phys. Rev. Lett.* **100** (2008) 042501.

[54] M. Vandebrouck *et al.*, *Phys. Rev. Lett.* **113** (2014) 032504.

[55] A. Bohr and B. R. Mottelson, Nuclear structure vol. I, (1975).

[56] R. D. Woods and D. S. Saxon, *Phys. Rev.* **95** (1954) 577.

[57] H. L. Clark *et al.*, *Nucl. Phys. A* **589** (1995) 416.

[58] G.R. Satchler, Introduction to Nuclear Reactions, Oxford University Press (1990).

[59] J. R. Comfort, M. N. Harakeh, Program CHUCK3, (1979). Modified version of CHUCK by P. D. Kunz, University of Colorado, unpublished.

[60] W. R. Leo., Techniques for nuclear and particle physics experiments, Springer-Verlag (2010).

[61] J. F. Ziegler, http://www.srim.org .

[62] R. Anne *et al.*, *Nucl. Instr. Meth. Phys. Res. A* **257** (1987) 215.

[63] A. A. Vorobyov *et al.*, *Nucl. Instr. Meth. Phys. Res. A* **270** (1988) 419.

[64] Y. Mizoi *et al.*, *Nucl. Instr. Meth. Phys. Res. A* **431** (1999) 112.

[65] C.E. Demonchy *et al.*, *Nucl. Instr. Meth. Phys. Res. A* **583** (2007) 341.

[66] M. Caamaño *et al.*, *Phys. Rev. Lett.* **99** (2007) 062502.

[67] I. Tanihata *et al.*, *Phys. Rev. Lett.* **100** (2008) 192502.

[68] T. Roger *et al.*, *Phys. Rev. C* **79** (2009) 031603.

[69] M. Vandebrouck, Ph.D. thesis, De l'Université Paris Sud; *Première mesure des résonances géantes isoscalaires dans un noyau exotique riche en neutrons : le* ^{68}*Ni avec la cible active MAYA,* (2013).

[70] ACTAR TPC: Conceptual Design Report (GANIL) **D28** (2012).

[71] J. C. Santiard *et al.*, Gassiplex, a low noise analog signal processor for readout of gaseous detectors, CERN-ECP (1994).

[72] National Nuclear Data Center, http ://www.nndc.bnl.gov.

[73] M. Pârlog *et al.*, *Nucl. Instr. Meth. Phys. Res. A* **482** (2002) 674.

[74] J. Pancin *et al.*, *JINST* **7** (2012) 01006.

[75] T. Roger *et al.*, *Nucl. Instr. Meth. Phys. Res. A* **638** (2011) 134.

[76] R. Veenhof, CERN Programe, http://garfield.web.cern.ch/garfield.

[77] J. Pancin, private communication.

[78] LISE++, http://lise.nscl.msu.edu/lise.html.

[79] K. Lau *et al., Nucl. Instr. Meth. Phys. Res. A* **366** (1995) 298.

[80] N. Auerbach *et al., Phys. Rev. C* **89** (2014) 014335.

[81] M. Itoh *et al., Phys. Rev. C* **68** (2003) 064602.

[82] M. Uchida *et al., Phys. Rev. C* **69** (2004) 051301(R).

[83] H. de Vries *et al., Atomic Data and Nuclear Data Tables* **36** (1987) 495.

Acknowledgements

So this is the end of four and a half years. I want to thank all the people who have helped me to extract a Doctor out of myself.

First of all, I want to thank Prof. Nasser Kalantar-Nayestanaki, who has welcomed me in his group and supported me throughout the entire PhD. His valuable supervision and constructive criticism pushed me to work efficiently on my project. Dear Nasser, you are also very skilled in extra-curricular activities. It was really impossible to defeat you in the card game even if we took several strategies. Besides, I always enjoy your driving even though some people panic while you drive. Thank you for introducing me to the Persian cuisine, which I am definitely going to miss.

I also want to express my gratitude to Prof. Muhsin Harakeh. Your gravity of knowledge is always an inspiration to me. You always answer my physics questions even if the questions are very stupid and simple. Thank you for all your help, support and patience.

It is now the time to thank Dr. Julien Gibelin. I still remember when you had asked me after our experiment in GANIL, "*Who is going to supervise you daily?*". At that moment I did not have the answer because few days ago I came to know that Dr. Jarno van de Walle, who was my daily supervisor for a couple of months after I started my PhD, was going to leave KVI. And then, you started to supervise me gradually. Although you are almost 800 km far from KVI, you have supervised me very efficiently through Skype, in spite of bad connection sometimes on both sides. The Saturday morning Skype meetings which became a weekly occurrence for some months, were really helpful for me. You always have a number of insights to tackle technical difficulties, which I faced during data analysis. I was overwhelmed to see the beeper that you had designed, which beeped every time when there was no beam. That was the life savior during the long night shifts.

I would like to express my heartfelt thanks for Dr. Catherine Rigollet, who has supported me throughout my entire PhD. I really enjoyed our chit-chats on cricket, especially during the Indian Premiere League (IPL). Please remember that you are always welcome to India during the IPL season to watch live matches. I should also thanks here Dr. Jarno van de Walle, who helped me in the beginning of my PhD to deal with ROOT program and data analysis.

I owe my sincere gratitude to my PhD thesis assessment committee, Prof. Thomas Aumann, Prof.

Angela Bracco and Prof. Olaf Scholten. Thank you for your careful reading of my manuscript and for all your questions and suggestions. Thank you Marine and Thomas for fruitful discussions regarding my data analysis and thank you Sara for your immense help during my experiment.

I am deeply grateful to Prof. A. K. Jain, Dr. R. Chatterjee and Dr. P. Arumugam from IIT Roorkee, India for motivating me to pursue a PhD in nuclear physics, that is why I am here. Here I also want to thank my Roorkee friends, Soham, Moumita, Anita, Subhash, Rashmi, Sandeep and Vishvas for their help and motivation. Thanks to Soham, Vishvas and Rashmi for being my travel partners for visiting several places in Europe.

Dear Alex and Marcel, thank you for being my paranymphs. Marcel, thank you for translating my thesis summary to Dutch. Dear Daren, Hossein, Simona, Roxana, Santosh and finally Oksana, for being my nice officemates from time to time. I would also like to thank Jacco for debugging problems in the KVI cluster so that I can run my analysis smoothly. Dear Ali, Alex, Auke, Marcel, Stefano, Sreekanth, Gia, Zahra, Josbert, Roxana, Amita, Ayan, Bodha, Gita, Daren, Nivedya, Ganesh, Olga, Olena, Solmaz, Christiaan, Nafise, Faruk, Mohammad, Artem, Johan, Myroslav, Oksana, Manisha, Hossein, Simona, Victor, Santosh, Qader, thank you guys for making my time in KVI unforgettable. Thanks to the members of KVI Movie Club for the several wonderful evenings we spent together.

I would like to thank all of my Indian friends in Groningen. I always enjoyed our elaborate Indian dinners we had together during weekends. Thanks Pavan, for sharing your amazing collection of *gazals* and other songs with us. Thanks Dipayan for helping me in designing my thesis cover. Thanks Sandeep and Dipayan for helping me in my tough times.

Last but not the least, thanks to my parents and family for their continuous support and sacrifices throughout my entire PhD. Without their support it would have been impossible for me to reach this goal. I am very much indebted to Sudarshana, who has decided to walk with me for the rest of my life. Her immense patience, support and understanding helped me to accomplish my task. Finally, my dearest ma, may your soul rest in peace. I will miss you.